

CR-189374

FIRST YEAR PIDDP REPORT ON GAMMA-RAY  
AND X-RAY SPECTROSCOPY

X-Ray Remote Sensing and In Situ Spectroscopy  
for Planetary Exploration Missions  
and  
Gamma-Ray Remote Sensing and In Situ Spectroscopy  
for Planetary Exploration Missions

(NASA-CR-189374) FIRST YEAR PIDDP  
REPORT ON GAMMA-RAY AND X-RAY  
SPECTROSCOPY: X-RAY REMOTE SENSING  
AND IN SITU SPECTROSCOPY FOR  
PLANETARY EXPLORATION MISSIONS AND  
GAMMA-RAY REMOTE SENSING AND IN  
SITU SPECTROSCOPY FOR PLANETARY  
EXPLORATION MISSIONS  
(EMR-Photoelectric) 141 p

N95-15916

Unclass

G3/43 0027536

First Year PIDDP Report on Gamma-Ray  
and X-Ray Spectroscopy

**X-Ray Remote Sensing and In Situ Spectroscopy  
for Planetary Exploration Missions**

and

**Gamma-Ray Remote Sensing and In Situ Spectroscopy  
for Planetary Exploration Missions**

M. Mahdavi, K.L. Giboni, S. Vajda  
EMR Photoelectric

J.S. Schweitzer, J.A. Truax  
Schlumberger-Doll Research

25 August, 1994

**Abstract:**

Detectors that will be used for planetary missions must have their responses calibrated in a reproducible manner. In addition, it is important to characterize a detector system at uneven portions of its life cycle, for example after exposure to different amounts of radiation. A calibration and response characterization facility has been constructed at Schlumberger-Doll Research for all types of gamma- and x-ray detectors that may be used for planetary measurement. This facility is currently being tested. Initial use is expected for the MARS 94 detectors. The facility will then also be available for calibrating other detectors as well as arrays of detectors such as the NEAR detector with its central NaI(Tl) crystal surrounded with a large BGO crystal.

Cadmium telluride detector are investigated for applications in space explorations. These detectors show an energy resolution of 5 keV for the 122 keV  $^{57}\text{Co}$  line. Earlier reported polarization effects are not observed. The detectors can be used at temperatures up to 100° C, although with reduced energy resolution. The thickness of standard detectors is limited to 2 mm. These detectors become fully efficient at bias voltages above 200 V. Initial results for a 1 cm thick detector show that the quality of the material is inferior to the thinner standard detectors and hole trapping affects the pulse height. A detailed characterization of the detector is in progress.

Prototypes of photomultipliers based on a Channel Electron Multiplier (CEM) are being built to study their performance. Such photomultipliers promise better timing characteristics and a higher dynamic range while being more compact and of lower in weight.

## Table of Content

1. Introduction	3
2. Detector Calibration and Response Characterization Facility	3
3. The Scintillation Mechanisms in Cerium-Doped Rare-Earth Oxyorthosilicates	4
4. Elemental Concentrations Determined With a Neutron Generator and a Gamma-Ray Detector	5
5. Fourier Transform Analysis of Germanium Spectra	5
6. CdTe Detectors for Space Applications	7
7. Large Volume CdTe Detectors	8
8. Development of a Channel-Electron-Multiplier PMT	11
9. Characterization of a Standard CEM	11
10. Development of Prototype CEM-PMTs	12
References	17
Presentations and Publications	18

### Appendices

1. First Semi-Annual Report for the PIDDP Program
2. The Role of Gadolinium in the Scintillation Processes of Cerium Doped Gadolinium Oxyorthosilicate
3. Application of Continuum Analysis to Borehole Gamma-Ray Spectra Obtained from the German Continental Deep Drilling Project
4. Evaluation of CdTe Detectors for X and  $\gamma$  Ray Detection

## Introduction

During the first year of this program, a number of different studies have been initiated. In all cases, they are focused on the fundamentals of detector properties, physics of planetary spectroscopic measurements, and the improvements that can be obtained with the use of a neutron generator on a planetary surface, all for improving the determination of elemental concentrations that can be related to the lithological constituents of the body under study. While a number of small efforts have also been made, e.g. study of detector properties at 150 K for a possible comet penetrator with W. Boynton - U. of Arizona, the primary studies in this time period have been on obtaining a better understanding of the scintillation mechanisms in the cerium-doped rare-earth oxyorthosilicates to better be able to predict their performance for different planetary missions, a better determination of the spectroscopic potential for measurements made with a neutron generator, a detector calibration and response characterization facility, and a study of a Fourier transform technique for including the Compton background in the analysis of an elemental response with a germanium detector, such as was planned for Mars Observer. In addition, a survey of all known scintillators has been initiated with a goal of determining optimum combinations of scintillator and photon converters to obtain the best possible detector system for particular planetary measurement requirements. Samples of some scintillators are available to identify and evaluate the best scintillator - photoconverter combination. A new photoconverter, a much more compact photomultiplier tube, has already been developed and implemented for the NEAR detector. Another novel photoconverter concept, a photomultiplier based on a Channel Electron Multiplier, is under investigation. First prototypes are now available for evaluation. A study is being undertaken to combine the best features of a Schlumberger and a GSFC high voltage system to obtain a new design that satisfies the requirements for high voltage generation for both neutron and X-ray generators. A study has been initiated to better understand the potential capability and use for a smaller, more compact, lower power version of the neutron generator for compatibility with a rover system for planetary measurements and the potential use of a larger volume CdTe detector than has been previously used has been studied.

The portion of this work that was completed for the six month report is incorporated in this report in Appendix 1. We will not repeat the relevant portions of that report here and will refer to the previously reported work by reference to that appendix.

## Detector Calibration and Response Characterization Facility

Detectors that will be used for planetary missions must have their responses calibrated in a reproducible manner, so that the information obtained during the mission can be better analyzed. In addition, it is important to characterize a detector system at uneven portions of its life cycle, for example after exposure to different amounts of radiation. The change in a detectors response can be well-determined in the laboratory, if an invariant reproducible facility exists that is unaltered over time. In addition, it is important that the facility is sufficiently flexible to permit the detector system to have its response to different stimuli, i.e. gamma rays of widely differing energies from different elemental sources, well characterized. This permits a critical experimental determination of spectral response to an elemental source and is a necessary component for the analysis of the data obtained on the mission. Such

measurements can also be used to benchmark Monte Carlo calculations that may be necessary to obtain final detector responses, either from an unplanned alteration in the detector response after launch or because of an inability to exactly simulate the planetary measurement environment in the laboratory.

The basic design for the calibration facility was presented earlier (Appendix 1). Initial tests were performed to validate the capability of the facility to obtain low noise spectra and to evaluate the time that would be needed to obtain sufficiently good spectra to determine a detector response to sufficiently good statistical precision. The basic operational nature of the calibration facility is filled with a quartz sand. This configuration provides capture gamma rays from silicon and hydrogen. A capture gamma-ray spectrum obtained in the calibration facility using the pulsed neutron generator and a 96% germanium detector is shown in Figure 1. The sand had a few kilograms of iron added to provide additional peaks in the spectrum. The clear peaks from hydrogen (2.2 MeV), silicon (3.5 and 4.9 MeV), and the iron peaks at 7.6 MeV. Inelastic gamma rays from oxygen are also provided to obtain peak gamma ray energies that span the energy range of interest. To provide additional responses, containers with specific elements (e.g., chromium) are buried in the sand at an appropriate location to add the desired gamma ray peaks to the spectrum. In this way, essentially arbitrary gamma-ray energies can be provided. Initial use of the facility will be to calibrate the radiation damaged MARS 94 germanium detector. The facility will then also be available for calibrating other detectors as well as arrays of detectors such as the NEAR detector with its central NaI(Tl) crystal surrounded with a large BGO crystal.

## **The Scintillation Mechanisms in Cerium-Doped Rare-Earth Oxyorthosilicates**

The cerium-doped rare-earth oxyorthosilicates are an interesting, recently discovered family of single crystal scintillators that have many useful properties as gamma-ray detectors. There are currently three established members of this family, a relatively light one based on yttrium, YSO,<sup>1</sup> and heavy ones based on gadolinium, GSO,<sup>2</sup> and lutetium, LSO.<sup>3</sup> All of these materials have relatively fast scintillation decays allowing high count rate capabilities without dead time and pile up corrections and appear to be at least reasonably resistant to radiation damage. However, the scintillation properties of these materials are not known. A further complication is that these materials have two different crystal structures. To make optimum use of such materials as possible detectors for planetary measurements, it is important to understand the scintillation mechanism of these materials to reliably predict their performance during the actual measurements.

The first of the cerium-doped rare-earth oxyorthosilicates to be used as a gamma-ray detector, GSO, has been extensively studied at Hitachi Chemical Company, the inventors of the material, and by us at Schlumberger-Doll Research, and at the National Synchrotron Light Source at Brookhaven National Laboratory, in collaboration with a group at California Institute of Technology. Through this effort, we have established a model that describes the scintillation properties of GSO. When gamma rays are incident on a GSO crystal, most of the energy is absorbed by the gadolinium. The energy then migrates through the gadolinium sub-lattice until it can be transferred to a cerium ion. The excited cerium atom then decays by emitting light

from the 5d to 4f transition. It is the resonant energy transfer between the gadolinium and the cerium that provides the two decay components seen in the light emission, and the dependence of the decay components as a function of cerium concentration is due to the migration of the energy through the gadolinium sub-lattice that results in the variation of the two decay components with cerium concentration (see Appendix 2). Work is continuing to better understand LSO, the heaviest of this type of detector, and potentially the best for measurements at temperatures below 300 K. A sample of GSO was irradiated and the detector characteristics were essentially unchanged. We expect to begin radiation studies on LSO in the next few months. A sample of LSO is being flown on the current Shuttle launch (August 1994) to experimentally confirm its worthiness for planetary measurements in space. Results of this test will be reported in the coming year.

### **Elemental Concentrations Determined With a Neutron Generator and a Gamma-Ray Detector**

The previous report (Appendix 1) presented studies of the use of a current technology neutron generator system for elemental concentration determination on a planetary surface (Venus). The potential use of this system with a Venera spacecraft was deemed to be completely satisfactory. Recent emphasis has focused on the desire for lighter payload missions, where even the relatively small weight and power requirements of the neutron generator may be too large. This is especially true for the case of a rover-based measurement. Thus, a concept has been proposed in which the size, weight, and power requirements of the current neutron generator system would be substantially reduced. This miniature system would, of course, have a much reduced neutron output. However, it is believed that one to two orders of magnitude more neutrons can be produced than are produced by the ambient cosmic-ray flux. Thus, such a miniature system could still significantly enhance elemental concentration measurement capability on planetary surfaces.

### **Fourier Transform Analysis of Germanium Spectra**

A study was completed (with J. Arnold and A. Thakur - UC San Diego) to test the spectral analysis approach that was to be taken with the germanium detector spectra from Mars Observer,<sup>4</sup>) a peak fitting program (GANYMED) and a Fourier transform analysis of the continuum. The study used data obtained with a Ge detector<sup>5</sup> in the German Continental Deep Drilling Project (KTB). The results have been accepted for publication (Appendix 3). We hope to compare these results with those obtained from a spline approach that has also been used to include the information in the Compton scattering response from a gamma-ray peak in the future.

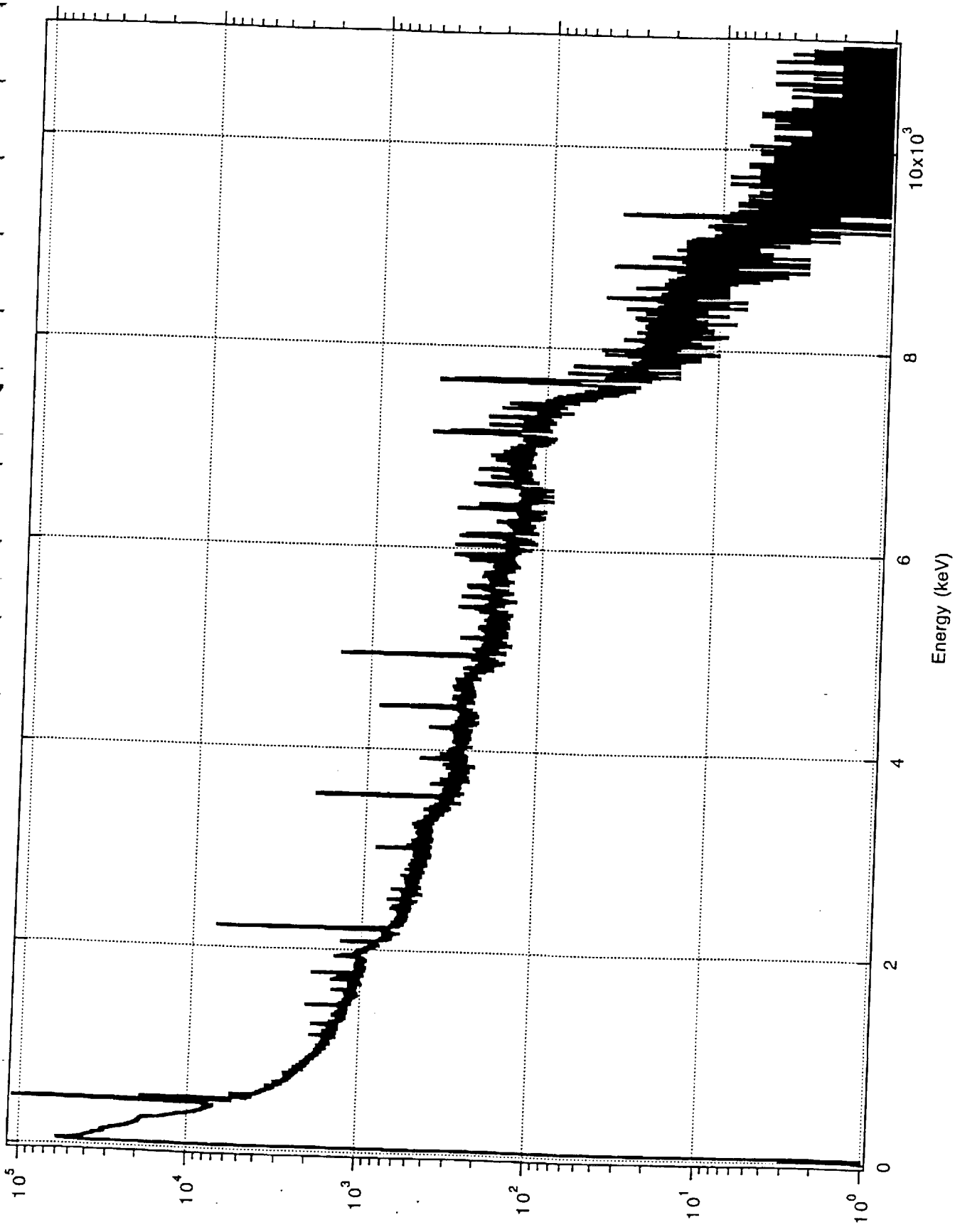


Fig. 1

## CdTe Detectors for Space Applications

The potential of cadmium telluride (CdTe) as nuclear detectors was recognized more than 25 years ago. The high atomic number and the large density promised to revolutionize the development of X- and  $\gamma$ -ray detectors. The fabrication of good spectroscopic detectors, however, turned out to be more difficult than expected. Usable detectors became available, but initially detectors were plagued by defects in their performance. One such defect was a polarization effect resulting in a decrease of pulse height and count rate over time.

The CdTe technology developed only slowly. The polarization effects were eliminated, the carrier lifetime was increased, and good detectors became commercially available. CdTe is now used in a growing number of applications. Many of these applications involve small handheld radiation monitors, taking direct advantage of the volume and weight of CdTe detector systems.

Together with  $\text{HgI}_2$  and the more recent  $\text{Cd}_{(1-x)}\text{Zn}_x\text{Te}$ , or CZT, cadmium telluride remains the only material sufficiently advanced in its development to be considered for practical detector applications. Surveys of the list of all possible materials revealed that no other material promised to be significantly better suited to justify the enormous research effort required for its development as nuclear detectors.  $\text{HgI}_2$  shows several severe drawbacks for many applications, especially the irreversible phase change at  $127^\circ\text{C}$  which reduces its usefulness when high temperature may be encountered during operation or storage.

CZT was strongly affected by hole trapping. The recent availability of high purity starting materials, especially zinc, provided better detectors, but reliable measurements of the hole trapping time are not yet available. A fast trapping of the holes renders CZT detectors inefficient in spectroscopic applications, since the holes can not travel the full thickness of a standard 2 mm detector. The pulse height becomes position dependent. Several institutions are presently testing the new CZT detectors.

CdTe detectors of good quality are commercially available.<sup>6</sup> The volume of the available crystals of spectrometer grade is limited to a fraction of a cubic centimeter, but the properties of the material, including high Z, high density, and 'room temperature' operation, make the available standard detectors a valuable alternative for many systems. The best energy resolution of these detector is about 4 - 5 keV for the 122 keV  $^{57}\text{Co}$  line. Although not at the level of germanium detectors, the resolution is better than scintillators. For interplanetary space missions the resolution of Ge detectors is frequently reduced due to radiation damage and temperature cycling, especially during launch of the vehicle.

For space applications CdTe offers the following advantages:

- High average Z of 50 and high density ( $6.06\text{ g/cm}^3$ ).
- Room temperature operation. Higher temperatures up to  $100^\circ\text{C}$  were repeatedly tested. The leakage current at elevated temperatures is increased, and the energy resolution is reduced. No damage to the detectors, however, was observed.
- Temperatures well above  $100^\circ\text{C}$  can be supported when the detector is not

operated, e.g. during launch.

- Good energy resolution of 4 - 5 keV for the 122 keV  $^{57}\text{Co}$  line. The energy resolution is reduced to 35 keV at 100° C. A better resolution is expected for lower temperatures, but were not tested yet during this study.
- Fully efficient spectroscopic detectors are readily available up to a thickness of 2 mm when operated with bias voltages above 200 V and amplifier shaping times above 2  $\mu\text{sec}$ .
- Small dead volume around contacts. Thickness of contacts about 1000 Å.
- Small volume and weight for the complete assembly. No cryogenics, low voltages (200 V), no optical coupling to photomultipliers.
- Simple arrangement of many detectors in arrays.

The properties of standard  $5 \times 5 \times 2 \text{ mm}^3$  CdTe detectors were evaluated in a study presented in appendix 4. In addition to the above mentioned properties, also the stability and the rate capability were measured. Of special interest for space applications are the characteristics at low temperatures down to -120° C. These tests have not yet been performed since the required equipment was not readily available. The investigations in the temperature range from -100° C to room temperature are planned to start soon.

The results of the present study indicate that CdTe is well suited for space applications. This conclusion is confirmed by the planned use of CdTe detectors in space missions. An European group is working on a array of 15,000 triangular detectors.<sup>7</sup>

### Large Volume CdTe Detectors

During the evaluation of standard 2 mm thick detectors, the pulse shapes were recorded. The pulse shapes for various depths of interaction within the detector volume are reproduced in the fig. 2. These pulse shapes were acquired at a bias voltage of 200 V, corresponding to a field strength of 1 kV/cm. The first pulse shape stems from an event which occurred very close to the cathode. The slow holes have only a short distance to travel. The electrons drift the full 2 mm and determine the rise time. For the remaining plots the events take place progressively farther away from the cathode. A clear break in the leading edge of the pulse can be observed once all the electrons reached the anode and only holes are still drifting with their reduced velocity. In the last plot the  $\gamma$ -ray interacts near the anode, and the rise time of the observed pulse is equal to the transit time of the holes. It is interesting that the charge pulse generated by the holes is rising linearly even for the longest drift time in the last pulse. The amount of hole trapping must be minimal. This result suggests that the use of much thicker detectors might be possible. A  $10 \times 10 \times 10 \text{ mm}^3$  detector was acquired to verify its performance. This detector is not a

standard item, and it was specially prepared for this study by Eurorad.<sup>8</sup>

The 10 mm thick detector shows an energy resolution of 11.75 keV FWHM for the 122 keV <sup>57</sup>Co line and 9.01 keV FWHM for the 60 keV <sup>241</sup>Am line. These values were determined with a bias voltage of 400 V. The loss in efficiency due to the small drift field is difficult to observe with this low energy radiation. Therefore, single pulse shapes were studied, similar to the evaluation of the standard detectors.

The bias voltage on the detector was increased to 1000 V in order to match the 1 kV/cm field strength of the earlier measurements. The initial fast rise is observed as expected with a maximum rise time of 1 μsec. This corresponds to the five times greater thickness. Special interest has been paid to the events with long hole drift. From the earlier results a maximum rise of 10 - 12 μsec is expected. Long hole signals are observed, but they do not rise linearly as expected. The signal is rounded and smoothly continues into the decay caused by the integrating constant (about 100 μsec) of the preamplifier. This observation is consistent with hole trapping which is much stronger than expected from the 2 mm detectors.

There are two explanation for the discrepancies:

- Recent measurements of the field distribution inside a CdTe detector show that the field is not equally distributed.<sup>9,10</sup> Close to the contacts the field strength is lower than expected. These results were recently published.
- The standard detectors are cut from long ingots. After application of the contacts they are tested for their qualities as a spectroscopic detector. The probability to find a spectroscopic 5 x 5 x 2 mm<sup>3</sup> detector were judged to be above 50 %. These detectors are further categorized according to the observed energy resolution. The detectors used in the study of standard devices all belonged to the best class with 4 - 6 keV resolution. The large detector has 20-times this volume, and the probability that the full volume is flawless is correspondingly small.

Further systematic measurements are planned with the large detector. The detailed study of the field distribution in this detector, and the pulse shapes from different regions of the detector could provide necessary information to understand the effects causing the hole trapping. The feedback of this information will help to produce better large detectors and to determine the largest size economically feasible.

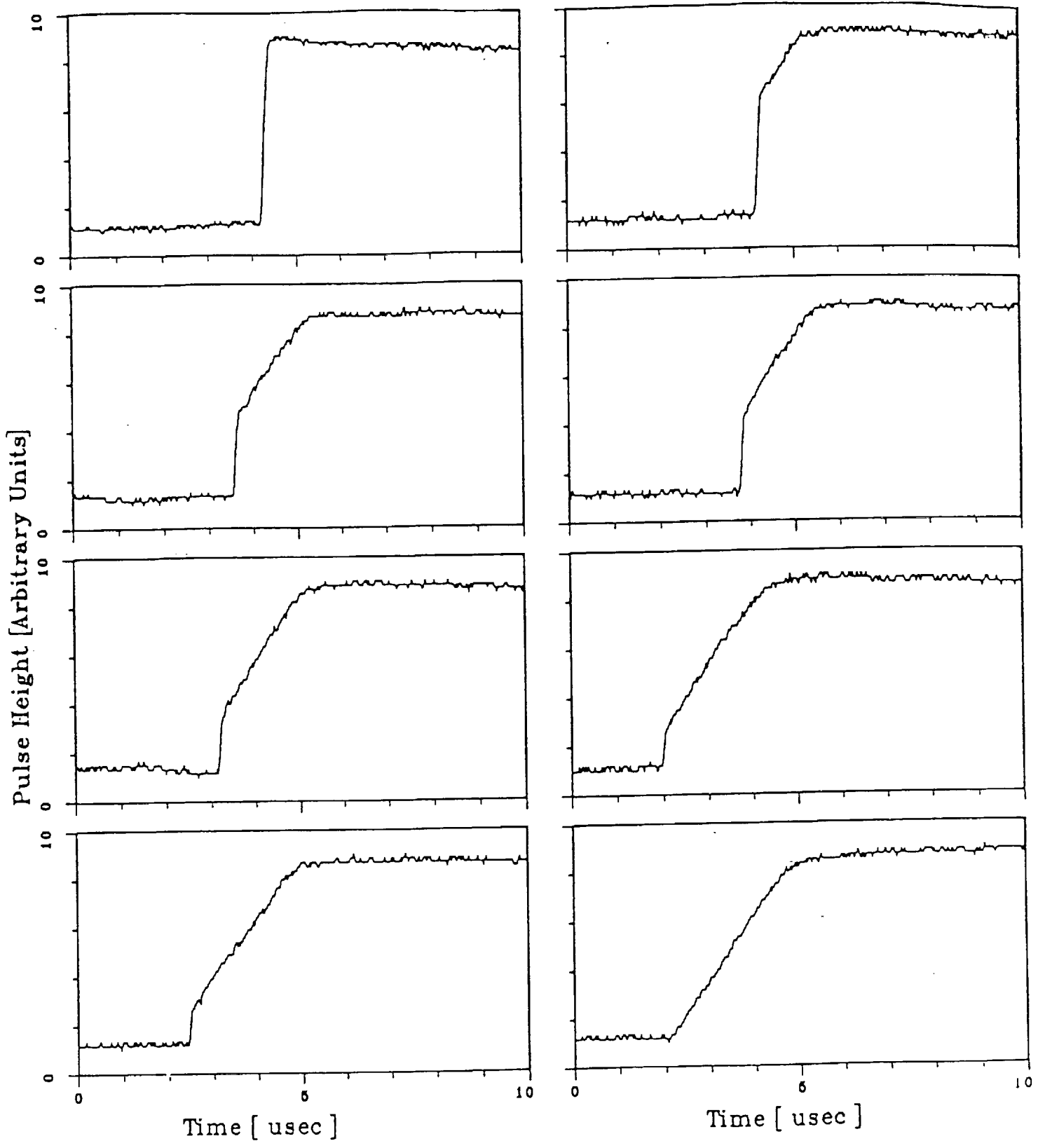


Fig. 2

## Development of a Channel-Electron-Multiplier PMT

Single channel electron multipliers (CEM) are continuous dynode electron multipliers. These devices are used in analytical instrumentation, e.g. mass spectrometers. In the early 70's, Bendix manufactured photomultipliers based on such CEMs for special applications with superior performance in magnetic fields and with good sensitivity and high speed. The performance level of CEMs at that time, however, was not sufficient to meet the demands of most photomultiplier applications, and production was finally discontinued due to the high costs and limited demand. The quality of CEMs was steadily advanced since then, and present day devices show enhanced gain, reduced noise, and increased maximum count rates.

The intrinsic qualities of CEM devices are expected to provide superior photomultipliers for space applications when coupled to a photocathode. Their small overall size and low weight would be particularly beneficial. The evaluation of such photodetectors has been started with a characterization of the available devices. These initial measurements on standard CEMs confirm the expectations, and prototypes of a CEM-PMT are under construction. After a study of these prototypes the final device can be designed.

## Characterization of a Standard CEM

The typical application of CEMs is in mass spectroscopy. Standard devices are neither optimized nor characterized for use in a PMT. Therefore, EMR initiated a study of the operational parameters of a standard CEM. The CEM chosen belongs to the 4800 series from Galileo, Sturbridge, MA.

### **Gain and High Count Rate Capability**

A gain of  $10^6 - 10^8$  is typical for standard CEMs and maximum count rates can be of the order of  $10^5 - 10^6$ . Higher count rates can be achieved by reducing the channel resistance, which shortens the time required to replenish the charges depleted by the signal current. Experience shows that the bias current should be several times the maximum signal current. The gain of the test CEM was measured using standard pulse counting electronics including a charge sensitive preamplifier and a multichannel analyzer (MCA). A gain of  $1.4 \times 10^8$  was measured at 2500 V bias.

The maximum count rate was determined by splitting the detector output to both an MCA and a fast counter. The input source strength was gradually increased while the output pulse height was monitored. The relation between gain and count rate is displayed in fig. 3. The maximum linear count rate is  $3 \times 10^6$ .

### **Dark Pulses**

The dark noise was measured with the same equipment used for the gain measurement.

In the absence of any input signal, at full operating voltage, the output pulses were monitored. The average level of dark counts was 0.03 counts per second. This dark noise is the intrinsic noise of the multiplying channel. Additional dark noise has to be expected when the channel is coupled to a photocathode in a PMT.

### **Single Electron Resolution**

The pulse height resolution was measured with standard pulse counting electronics. When stimulated with photoelectrons the pulse height distribution is a Gaussian with a Full Width Half Maximum of 69 % at the operating voltage.

### **Dynamic Range**

The dynamic range of the multiplier is defined as the range between the smallest and largest detectable signal. This range was determined to be approximately  $1.1 \times 10^6$ .

### **Time Resolution**

The time resolution of a CEM is characterized by the rise time and the pulse width of the output pulses. For these measurements the anode was connected to a Tektronix 7104 analog oscilloscope. The pulse rise time was measured to be 7 nsec, and the width to be 15 nsec.

### **Plateau Characteristic**

A distinct plateau characteristic is important for the performance of an electron multiplier in pulse counting applications. A stable input count rate was established, and then the bias voltage was raised while recording the resulting output count rate. The result is shown in fig. 4. A plateau is identified between 2000 V and 2500 V.

## **Development of Prototype CEM-PMTs**

Several characteristics of a CEM-PMT can only be evaluated in a complete prototype, i.e. a CEM coupled to a photocathode in a vacuum envelope.

### **Dark Noise**

The dark noise of the channel multiplier is extremely low with 0.03 counts per second. In a PMT, however, the dark count rate will be governed by noise from the photocathode.

### **Life Time**

Typical life times for CEMs in mass spectrometers are about 1 year, mostly limited by the reaction with the organic gas ions introduced during this operation. For application where a very good vacuum is guaranteed, as in the case of a PMT, the average life is expected to exceed 5 years.

### **Linearity for High Instantaneous Rates**

A special case is the exposure of the CEM to high instantaneous count rates such as in  $\gamma$ -ray spectroscopy. A  $\gamma$ -ray can produce sufficient light in a scintillator to generate more than 10,000 photoelectrons in a photocathode. These photoelectrons reach the channel within a few nsec. The instantaneous current can be large, without the average exceeding the maximum signal current of the CEM. In this case, the behavior of the CEM is not determined by the resistance of the channel, but its capacitance.

### **Recovery After High Light Exposure**

For a PMT it is important to quickly return to its normal operational characteristics after exposure to very high light levels.

To ensure a rapid progress of the investigations, the prototypes of CEM-PMTs are under construction, where the CEM is enclosed in a glass envelope and a photocathode is deposited on an entrance window. For a final design it appears imperative to use the CEM body itself as a hermetically sealed envelope. The size and the weight of the assembly can thus be reduced to a minimum. This will require that the entrance window is hermetically sealed to the cone of the CEM, and the anode connection must be vacuum tight. For glass CEMs the body itself is normally hermetic. For ceramic CEMs additional treatment of the ceramic body might be necessary. This is technically feasible, but requires development work. It was therefore decided to first evaluate the operational characteristics of CEM-PMTs in a separate envelope. A schematic view of the prototypes is shown in fig. 5. If the results from the evaluation confirm the expectations, the development of the final design can be started.

# Gain vs. Counts/sec 4816B Channeltron

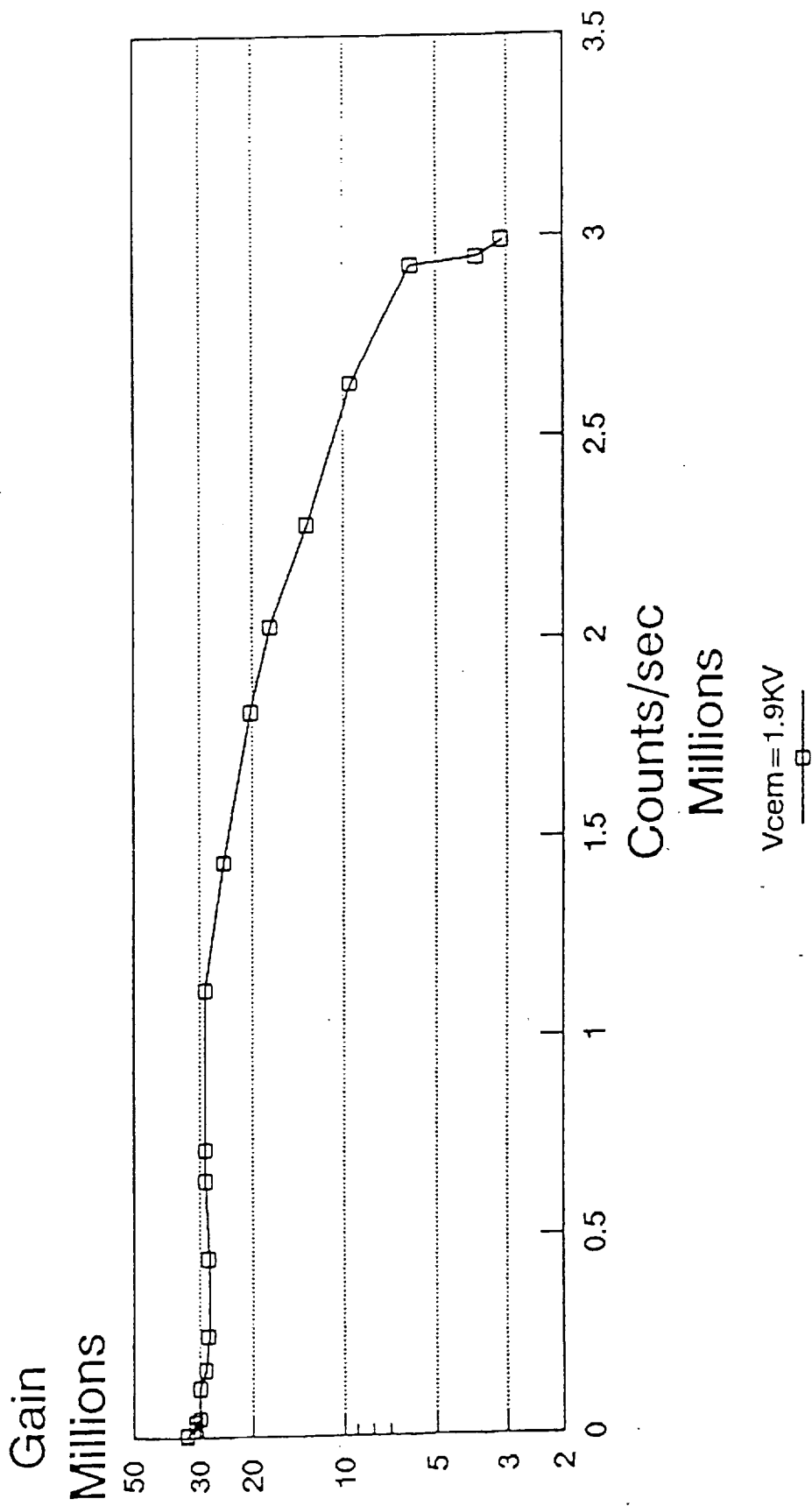


Fig. 3

# Counts/sec vs. Voltage 4816B Channeltron

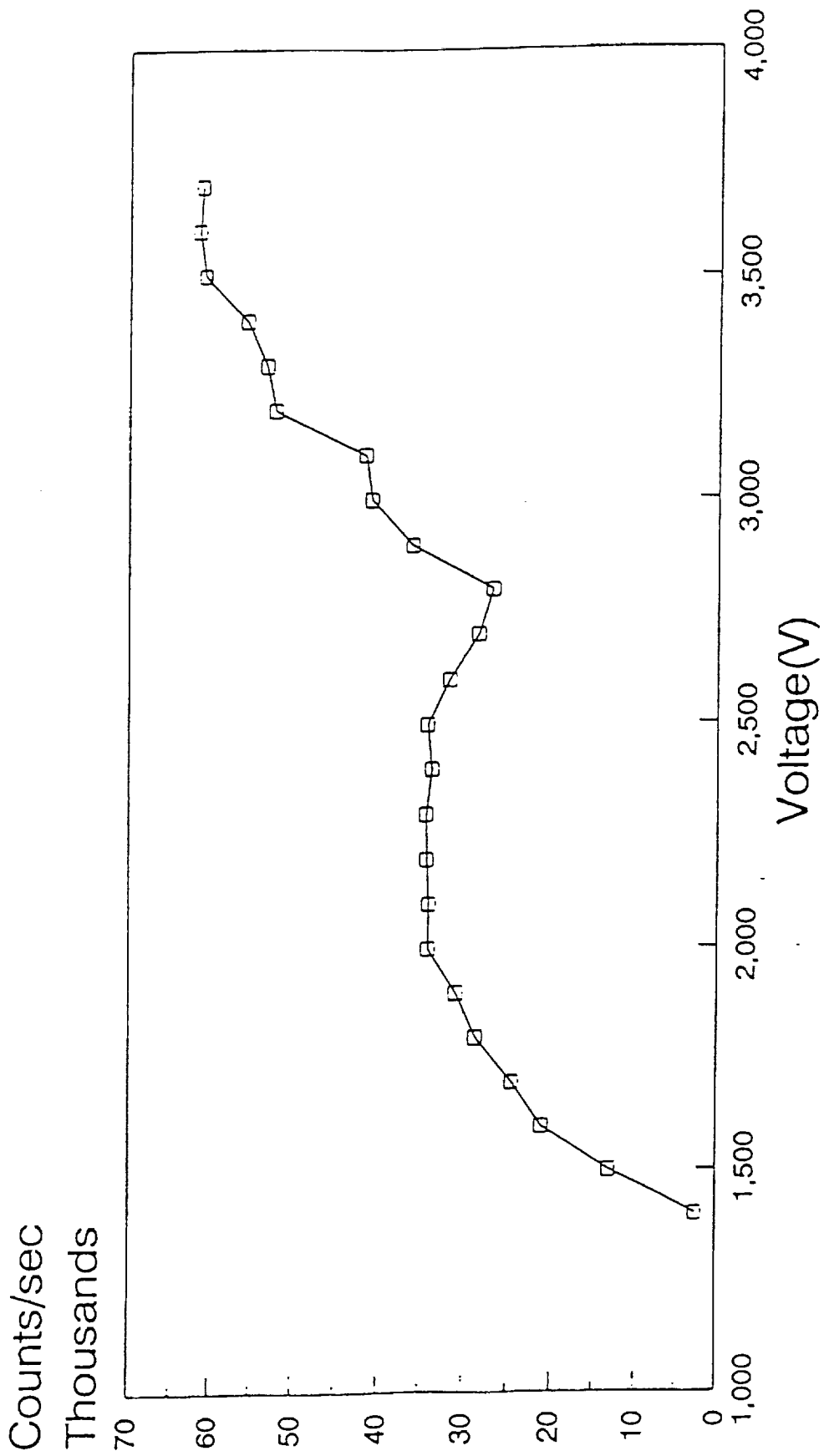
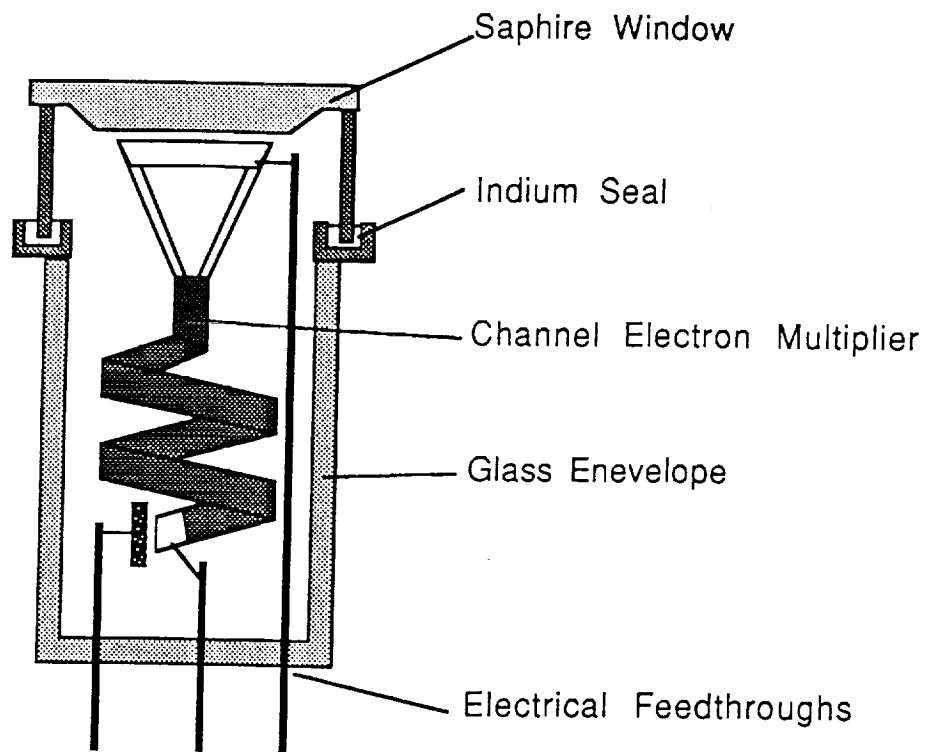


Fig. 4



Assembly of Channel Electron Multiplier in a Glass Envelope for Testing

Fig. 5

P10

Table 1: Inorganic Scintillators

Crystal	Z	Density (g/cm <sup>3</sup> )	Refractive Index	Hygroscopic	Radiation Length (cm)	$\lambda$ Fast Component (nm)	$\lambda$ Slow Component (nm)	Decay Fast Comp (ns)	Decay Slow Comp (ns)	Yield % NaI <sup>a</sup>	Light Yield (phot/MeV)
BGO	75	7.13	2.19	no	1.11	480	-	300	-	13	8200
BaCl <sub>2</sub>	50	3.90	-	-	-	-	-	1.2, 3.5	-	-	25000
BaF <sub>2</sub>	53	4.88	1.49	no	2.06	220	310	0.60	620	5 <sup>b</sup>	2200 <sup>b</sup>
BaI <sub>2</sub>	54	5.15	-	no <sup>c</sup>	-	190-340	-	6	-	-	-
BaLiF <sub>3</sub>	51	5.24	-	-	2.13	240-440	-	<25	-	5	2200
BaYb <sub>2</sub> F <sub>8</sub>	63	6.99	-	-	1.3	>310	-	-	-	-	-
CaF <sub>2</sub>	17	3.19	1.44	no	-	435	-	940	-	40	24000
CaWO <sub>4</sub>	67	6.12	1.92	no	-	430	-	500	20 $\mu$ s	50	18000
CdI <sub>2</sub>	52	5.67	-	-	1.5	540	-	3	-	-	-
CdWO <sub>4</sub>	65	7.90	2.2 - 2.3	no	1.06	540	-	5 $\mu$ s	-	40	15300
CeCl <sub>3</sub>	51	3.90	-	-	-	-	-	4.4, 23	-	-	28500
CeF <sub>3</sub>	53	6.16	1.68	no	1.7	310	340	5	30	4	4000
CeF <sub>3</sub> (Ca)	53	6.10	-	slightly	1	340	-	30	-	-	-
CsBr	50	4.40	-	no	-	250	390	.07	>500	5	900
CsCaCl <sub>3</sub>	47	2.90	-	-	-	205-305	-	<1	-	10	5000
CsCl	52	4.00	-	no	-	240-270	390	.88	>500	5	900
CsF	53	4.11	1.48	very	2.0	390	-	2.80	4.40	5	2500
CsI	54	4.53	1.80	slightly	1.86	320	> 400	10	> 1 $\mu$ s	4	2000
CsI(Na)	54	4.53	1.84	yes	1.86	420	-	630	-	75	39000
CsI(Tl)	54	4.53	1.80	slightly	1.86	565	-	1 $\mu$ s	-	45	52000
Gd <sub>2</sub> SiO <sub>5</sub>	59	6.71	1.85	no	1.38	440	-	56	600	25	10000
KCaF <sub>3</sub>	17	3.00	-	-	-	140-190	-	<2	-	5	2200
KLuF <sub>4</sub>	63	4.80	-	-	2	165-200	-	1.5	-	-	170-400
KMgF <sub>3</sub>	15	3.16	-	-	7.72	140-190	180	1.5	-	2	3500

<sup>a</sup> Relative Pulse Height with a Bialkali Photocathode

<sup>b</sup> Fast Component only

<sup>c</sup> Unstable in Air

Crystal	Z	Density (g/cm <sup>3</sup> )	Refractive Index	Hygroscopic	Radiation Length	$\lambda$ Fast Component	$\lambda$ Slow Component	Decay Fast Comp	Decay Slow Comp	Yield	Light Yield
---------	---	------------------------------	------------------	-------------	------------------	--------------------------	--------------------------	-----------------	-----------------	-------	-------------

Crystal	Z	Density (g/cm <sup>3</sup> )	Refractive Index	Hygro- scopic	Radiation Length (cm)	$\lambda$ Fast Component (nm)	$\lambda$ Slow Component (nm)	Decay Fast Comp (ns)	Decay SlowComp (ns)	Yield % NaI <sup>a</sup>	Light Yield (phot/MeV)
KYF4(Rb)	33	3.60	-	-	-	140-190	-	1.9	-	5	2200
LsO	66	7.40	1.82	no	1.14	420	-	12	42	75	-
LXe	54	3.06	1.5	-	2.77	170	-	3-25	-	-	26000
LaF3(Ce)	53	>5.9	1.70	-	-	290, 305	-	3-27	-	-	2200
LaF3(Nd)	53	5.94	1.70	no	-	173, 245	-	6.3	-	5	200
LiBaF3	51	4.90	-	-	2.3	200-230	-	1.9	-	5	2200
LiI(Eu)	52	4.08	1.96	yes	-	470	-	600	1.4 $\mu$ s	35	11000
LiYbF4	64	6.09	-	-	1.56	400-500	-	<25	-	5	2200
NaI(Tl)	51	3.67	1.85	yes	2.6	415	-	230	1.5 ms	100	38000
PbCO3	76	6.6	1.80	no	-	475	-	5.6	27, 155	<1	-
RbCaF3	31	2.83	-	-	-	-	-	1	-	5	2200
RbF	35	3.60	-	yes	-	200, 380	-	1.3	-	5	2200
ThF4	85	6.32	-	-	1.18	330, 450	-	<25	-	-	-
Y3Al5O12	33	4.56	-	-	3.5	550	-	65	-	-	14000
YAlO3(Ce)	33	5.55	1.94	no	2.63	350-390	-	17-35	-	12	18500
YSO	35	4.54	-	-	-	400	500	37	82	25	-
ZnO	29	5.61	2.02	no	-	385	-	-	-	40	-
ZnS(Ag)	28	4.09	2.35	no	-	450	-	200	-	150	-
ZnWO4	64	7.84	2.20	no	1.12	475	-	5 $\mu$ s	20 $\mu$ s	26	9500

<sup>a</sup> Relative Pulse Height Measured with BiAlkali Photocathode.

ORIGINAL PAGE IS  
OF POOR QUALITY

P.12

Table 2a: Promising High Density Scintillators

Crystal	Z	Density (g/cm <sup>3</sup> )	Refractive Index	Hygro- scopic	Radiation Length (cm)	$\lambda$ Fast Component (nm)	$\lambda$ Slow Component (nm)	Decay Fast Comp (ns)	Decay SlowComp (ns)	Yield % NaI <sup>a</sup>	Light Yield (phot/MeV)
BGO	75	7.13	2.19	no	1.11	480	-	300	-	13	8200
CaWO <sub>4</sub>	67	6.12	1.92	no	-	430	-	500	20 $\mu$ s	50	18000
CdWO <sub>4</sub>	65	7.90	2.2 - 2.3	no	1.06	540	-	5 $\mu$ s	-	40	15300
Gd <sub>2</sub> SiO <sub>5</sub>	59	6.71	1.85	no	1.38	440	-	56	600	25	10000
LSO	66	7.40	1.5	no	1.14	420	-	12	42	75	-
ZnWO <sub>4</sub>	64	7.84	2.20	no	1.12	475	-	5 $\mu$ s	20 $\mu$ s	26	9500

<sup>a</sup> Relative Pulse Height with a Bialkali Photocathode

Table 2b: Promising Medium Density Scintillators

Crystal	Z	Density (g/cm <sup>3</sup> )	Refractive Index	Hygro- scopic	Radiation Length (cm)	$\lambda$ Fast Component (nm)	$\lambda$ Slow Component (nm)	Decay Fast Comp (ns)	Decay SlowComp (ns)	Yield % NaI <sup>a</sup>	Light Yield (phot/MeV)
LSO	66	7.40	1.82	no	1.14	420	-	12	42	75	-
NaI(Tl)	51	3.67	1.85	yes	2.6	415	-	230	1.5 ms	100	38000
YSO	35	4.54	-	-	-	400	500	37	82	25	-
CsI(Na)	54	4.53	1.84	yes	1.86	420	-	630	-	75	39000
CsI(Tl)	54	4.53	1.80	slightly	1.86	565	-	1 $\mu$ s	-	45	52000

<sup>a</sup> Relative Pulse Height Measured with Bialkali Photocathode.ORIGINAL PAGE IS  
OF POOR QUALITY

## Compact PMTs

Schlumberger-EMR has a line of photomultipliers well suited to well logging applications in extremely harsh conditions. The expertise was developed and successfully applied Measurement-While-Drilling (MWD) operations, which subject the tool and detector to shock levels in excess of 500 g in a continuous fashion, and high levels of random vibrations. Problems arising from size limitations led to the development of compact PMTs with similar characteristics but a drastically reduced size. Tests conducted in 1993 for the qualification of this novel detector showed no performance degradation while allowing a smaller detector package. An added advantage was the development of extremely compact power supplies that use the volume around the electron multiplier structure. This development allowed operation of the detector to higher count rates than before, with higher reliability and linearity, while still reducing the original detector size.

The original size of a 1.25" diameter photomultiplier was 4.2" long. The compact PMT of the same diameter is 2.5" long when fully packaged with its biasing resistor network and the shock resistant potting. The integrated power supply brings the package to 3.1" length with no change in diameter. The power supply delivers up to 2400 V and operates up to 150°C, with a higher temperature version being finalized in the first half of 1994.

A similar approach is being applied to larger diameter ( 2" - 3" ) photomultipliers. A 3" photomultiplier can be packaged to a length of 3.5". This technology is being employed in the  $\gamma$ -ray detector for the NEAR project.

It is worth mentioning that these photomultipliers were developed for a large range of temperatures up to 200°C. The photocathodes are being matched to the various emission characteristics of the scintillating crystals, including, but not limited to, NaI(Tl), BGO, and GSO ( gadolinium oxyorthosilicate). Detectors including these scintillators are being successfully used in various applications.

## Short Term Plans

- Microchannel Plate (MCP) PMTs

Replacing the multiplying structure in a PMT by a set of Multi Channel Plates could result in a significant length and weight reduction. MCP-PMTs provide an imaging capability which might considerably enhance the performance of present X-ray detection systems. Prototypes of such MCP-PMTs exist. The performance characteristics of these devices will be investigated.

- Channel Electron Multiplier (CEM) PMTs

The main topic of this investigation is to determine if Channel Electron Multipliers can replace the classical PMT with an advantage in size, weight, or performance.

- Other solid state electron multiplication devices

There are several possibilities to employ Avalanche Photo Diodes (APDs) to replace some parts of the multiplying structure in a classical PMT.

- Miniature Detectors

Certain combinations of scintillating crystals, compact PMTs, and integrated power supplies offer unique characteristics of compactness, reliability, and performance for specific applications. The most promising combinations will be evaluated.

- Space Qualification of Integrated Power Supplies

The miniaturized power supplies mentioned above have excellent characteristics of stability, ruggedness, and operating temperature range. When used with the small size PMTs they use the available space very efficiently and improve the high count rate linearity. They contain both passive and active surface mount components. The space worthiness of these power supplies will be evaluated.

**ORIGINAL PAGE IS  
OF POOR QUALITY**

Appendix 1

A NEUTRON ACTIVATION GAMMA RAY SPECTROMETER  
FOR PLANETARY SURFACE ANALYSIS

J.G. Bradley  
Jet Propulsion Laboratory, 306-336  
California Institute of Technology  
4800 Oak Grove Drive  
Pasadena, California 91109

J.S. Schweitzer, J.A. Truax  
Schlumberger-Doll Research  
Old Quarry Road  
Ridgefield, Connecticut 06877

A. Rice, T.A. Tombrello  
California Institute of Technology, 200-36  
Pasadena, California 91125

ABSTRACT

A pulsed DT neutron generator system, similar to that used in commercial well logging, offers the possibility of performing accurate elemental analyses to depths of tens of centimeters in a few seconds with the probe on the body's surface. Through time-phased measurements of the gamma-ray spectrum synchronized with the neutron pulses, concentrations of hydrogen, carbon and key mineral forming elements can be determined even with a low-resolution spectrometer. If a high resolution spectrometer is used, the number of elements measured and the sensitivity for measurement is increased. An implanted probe system, such as in a comet or ice cap penetrator, would offer the highest possible sensitivity.

An inexpensive neutron probe system based on modifications of the Schlumberger well-logging system has been proposed for the Discovery/Venera/SAGE Mission to Venus and the Mars Polar Pathfinder. Preliminary experiments on a simulated Venusian surface indicate that high quality results can be obtained.

INTRODUCTION

There are a number of planned and contemplated NASA, ESA, and Russian solar system lander missions that will characterize planets and small bodies over the next ten years. These include missions to the Moon, Mars, Venus, asteroids and comets. Except for gamma-ray spectrometers, the existing suite of "demonstrated" instruments can only characterize the first fraction of a millimeter of the surface for elemental composition unless drilling or excavating techniques are used. Cosmic-ray induced activation analysis by gamma-ray counting can determine the composition of significant volumes, but only with tens of hours counting time for high quality measurements.

**ORIGINAL PAGE IS  
OF POOR QUALITY**

## References

1. C.D. Brandle, A.J. Valentino, and G.W. Berkstresser. Jour. of Crystal Growth **79** 308 (1986).
2. K. Takagi and T. Fukazawa. Appl. Phys. Letters **42** 43 (1983).
3. C.L. Melcher and J.S. Schweitzer. Nucl. Inst. & Meth. **A314** 212 (1992).
4. A.N. Thakur and J.R. Arnold. Nucl. Inst. & Meth. **A325** 529 (1992).
5. J.S. Schweitzer, C.A. Peterson, and J.K. Draxler. IEEE Trans. Nucl. Sci. **35**(1) 847 (1993).
6. P. Siffert; Cadmium Telluride and Related Materials as X- and Gamma- Ray Detectors: A Review, talk presented at SPIE conference on Gamma Ray Detector Physics and Applications, San Diego, 29 July, 1994
7. P. Siffert, CNRS Strasbourg, France; private communication
8. Eurorad, 14 Rue Lenôtre, Mittelhausbergen, 67200 Strasbourg, France
9. C. Manfredotti, F. Fizzotti, E. Vitone; Monte Carlo Simulation of a CdTe Spectrometer: Best Time and Energy Resolution Performances, talk presented at SPIE conference on Gamma Ray Detector Physics and Applications, San Diego, 29 July, 1994
10. M.C. Busch, M. Hage-Ali, J.M. Koebel, P. Siffert; Internal Field Distributions in Semi-Insulating Cadmium Telluride Detectors, talk presented at SPIE conference on Gamma Ray Detector Physics and Applications, San Diego, 29 July, 1994

## Presentations and Publications

J. S. Schweitzer and J. A. Truax, Elemental measurements on the surface of Venus. Vernadsky-Brown Microsymposium 18, Moscow, 1993.

J. A. Bradley, J. S. Schweitzer, J. A. Truax, A. Rice, and T. A. Tombrello, A neutron activation gamma ray spectrometer for planetary surface analysis. IAA meeting, The Johns Hopkins University Applied Physics Laboratory, Columbia, Md., April, 1994.

J. S. Schweitzer, J. A. Bradley, J. L. Callas, J. A. Truax, J. I. Trombka, W. V. Boynton, J. R. Arnold, M. Mahdavi, K. L. Giboni, A. P. Rice, and T. A. Tombrello, A pulsed neutron activation gamma-ray spectrometer for planetary surface analysis. Mars Surveyor Workshop, Jet Propulsion Laboratory, Pasadena, Ca., May 1994.

H. Suzuki, T. A. Tombrello, C. L. Melcher, C. A. Peterson, and J. S. Schweitzer, The role of gadolinium in the scintillation processes of cerium-doped gadolinium oxyorthosilicate. Nucl. Instrum. & Meth. A346, 510-521, 1994.

A. N. Thakur, J. R. Arnold, and J. S. Schweitzer, Continuum gamma-ray spectral analysis in the German Continental Deep Drilling Project, accepted for publication in Nuclear Geophysics. 1994.

**Appendix 1**

**First Semi-Annual Report for the PIDDP Program**

First Semi Annual Report  
for PIDDP Program  
Contract NAS5-32486

X-Ray Remote Sensing and In-Situ Spectroscopy  
for Planetary Exploration Missions

and

Gamma-Ray Remote Sensing and In-Situ Spectroscopy  
for Planetary Exploration Missions

M. Mahdavi, K.L. Giboni, and S. Vajda  
EMR-Photoelectric

J. Schweitzer  
Schlumberger-Doll Research

9 May, 1994

Abstract:

Detectors that will be used for planetary missions must have their responses calibrated in a reproducible manner. A calibration facility is being constructed at Schlumberger-Doll Research for Gamma- and X-Ray detectors. With this facility the detector response can be determined in an invariant and reproducible fashion. Initial use of the facility is expected for the MARS94 detectors.

Work is continuing to better understand the rare earth oxyorthosilicates and to define their characteristics. This will allow a better use of these scintillators for planetary missions. In a survey of scintillating materials two scintillators were identified as promising candidates besides GSO, LSO, and YSO. These are CdWO<sub>4</sub> and CsI(Tl). It will be investigated, if a detector with a better overall performance can be assembled with various photon converters.

Considerable progress was achieved in photomultiplier design. The length of an 1" diameter PMT could be reduced from 4.2" to 2.5" without performance degradation. This technology is being employed in the gamma-ray detector for the NEAR project. A further weight and size reduction of the detector package can be achieved with miniaturized integrated power supplies.

## Six Month PIDDP Report on Gamma-Ray and X-Ray Spectroscopy

### Introduction

During the initial six months of this program, a number of different studies have been initiated. In all cases, they are focused on the fundamentals of detector properties, physics of planetary spectroscopic measurements, and the improvements that can be obtained with the use of a neutron generator on a planetary surface, all for improving the determination of elemental concentrations that can be related to the lithological constituents of the body under study. While a number of small efforts have also been made, e.g. study of detector properties at 150 K for a possible comet penetrator with W. Boynton - U. of Arizona, the primary studies in this time period have been on obtaining a better understanding of the scintillation mechanisms in the cerium-doped rare-earth oxyorthosilicates to better be able to predict their performance for different planetary missions, a better determination of the spectroscopic potential for measurements made with a neutron generator, a detector calibration and response characterization facility, and a study of a Fourier transform technique for including the Compton background in the analysis of an elemental response with a germanium detector, such as was planned for Mars Observer. In addition, a survey of all known scintillators has been initiated with a goal of determining optimum combinations of scintillator and photon converters to obtain the best possible detector system for particular planetary measurement requirements. During the past decade Schlumberger developed a line of rugged, high temperature photomultipliers for well logging applications. This technology together with highly efficient photocathodes was applied for a new photoconverter, a much more compact photomultiplier tube, which has already been implemented for the NEAR detector. Finally, a study is being undertaken to combine the best features of a Schlumberger and a GSFC high voltage system to obtain a new design that satisfies the requirements for high voltage generation for both neutron and X-ray generators in a space environment.

### Detector Calibration and Response Characterization Facility

Detectors that will be used for planetary missions must have their responses calibrated in a reproducible manner, so that the information obtained during the mission can be better analyzed. In addition, it is important to characterize a detector system at uneven portions of its life cycle, for example after exposure to different amounts of radiation. The change in a detectors response can be well-determined in the laboratory, if an invariant reproducible facility exists that is unaltered over time. In addition, it is important that the facility is sufficiently flexible to permit the detector system to have its response to different stimuli, i.e. gamma rays of widely differing energies from different elemental sources, well characterized. This permits

a critical experimental determination of spectral response to an elemental source and is a necessary component for the analysis of the data obtained on the mission. Such measurements can also be used to benchmark Monte Carlo calculations that may be necessary to obtain final detector responses, either from an unplanned alteration in the detector response after launch or because of an inability to exactly simulate the planetary measurement environment in the laboratory.

A design has been completed for such a calibration and response characterization facility at Schlumberger-Doll Research for all types of gamma-ray (and x-ray) detectors that may be used for planetary measurement, whether orbital or on the planetary body. Neutron sources, either small D,T accelerators or isotopic sources, can be accurately positioned in a number of locations to obtain the desired response. The design also allows for the use of a compact x-ray generator. There is a 96% efficient germanium detector (Resolution ~ 2.1 keV) that is continuously available to insure stability of the electronics and geometry. The main calibration facility will be constructed of plywood and about 1500 lbs. of JSC-1 lunar simulant (obtained with the assistance of Texas A&M and JPL). There is a side-mounted arrangement to position the center of the front face of all detectors in a reproducible geometry. This design is shown in Figure 1. There will also be a facility filled with calcite that will allow response characterization to be obtained for arbitrary elements by "salting" the container with sealed samples of any elemental composition desired. There will also be other similar samples for obtaining detector responses in different mixes of elemental concentrations. The facility should be available for use in about 1-2 months.

Initial use of the facility is expected to be the MARS 94 detectors. The facility will then also be available for calibrating other detectors as well as arrays of detectors such as the NEAR detector with its central NaI(Tl) crystal surrounded with a large BGO crystal.

## The Scintillation Mechanisms in Cerium-Doped Rare-Earth Oxyorthosilicates

The cerium-doped rare-earth oxyorthosilicates are an interesting recently discovered family of single crystal scintillators that have many useful properties when using them as gamma-ray detectors. There are currently three established members of this family, a relatively light one based on yttrium, YSO,<sup>1)</sup> and heavy ones based on gadolinium, GSO,<sup>2)</sup> and lutetium, LSO.<sup>3)</sup> All of these materials have relatively fast scintillation decays allowing high count rate capabilities without dead time and pile up corrections and appear to be at least reasonably resistant to radiation damage. However, the scintillation properties of these materials are not known. A further complication is that these materials have two different crystal structures. To make optimum use of such materials as possible detectors for planetary measurements, it is important to understand the scintillation mechanism of these materials to reliably predict their performance during the actual measurements.

The first of the cerium-doped rare-earth oxyorthosilicates to be used as a gamma-ray detector, GSO, has been extensively studied at Hitachi Chemical Company, the inventors of the material, and by us at Schlumberger-Doll Research, and at the National Synchrotron Light Source at Brookhaven National Laboratory, in collaboration with a group at California Institute of Technology. Through this effort,

we have established a model that describes the scintillation properties of GSO. This allows a better use of GSO for planetary measurements as the response can be predicted under any measurement condition. Work is continuing to better understand LSO, the heaviest of this type of detector, and potentially the best for measurements at temperatures below 300 K. A sample of GSO was irradiated and the detector characteristics were essentially unchanged. We expect to begin radiation studies on LSO in the next six months.

## Elemental Concentrations Determined With a Neutron Generator and a Gamma-Ray Detector

To better understand the potential for the use of pulsed neutron generators with landers, rovers, and penetrators, a laboratory model was constructed to simulate the surface of Venus. The elemental composition of the laboratory model was intended to simulate the analysis obtained by the Venera 14 lander. This comparison is shown in Table 1.

Element	Venera 14 measurements	Venusian simulant
Magnesium	4.9	4.3
Aluminum	9.5	7.9
Silicon	22.7	19.5
Potassium	0.17	0.65
Calcium	7.4	7.2
Titanium	0.75	0.75
Manganese	0.16	0.12
Iron	6.8	6.8
Sulfur	0.35	0.27
Chlorine	0.4	0.42
Oxygen	43.6	47.5
Carbon	-	4.3
Sodium	-	0.28
unknown	3.3	-

Table 1. Comparison between elemental content determined by Venera 14 and the laboratory Venusian simulant.

Gamma-ray spectra were obtained with a GSO detector, from reactions involving high energy neutrons (during the burst), thermal neutrons (shortly after the end of the burst), and delayed activation (after the accelerator was turned off). Studies were also performed to investigate the effect of the possible uncertain amount of the Venusian atmosphere that would contribute to the measurement. Other than for the expected additional contribution of carbon and oxygen gamma rays, no alteration in the spectra were observed. A presentation of the initial efforts on this work was given at the Vernadsky-Brown Microsymposium in Moscow in the Fall of 1993. A poster on this work was presented at the IAA meeting at the Johns Hopkins University Applied Physics Laboratory in April, 1994. A copy of the preprint for the IAA meeting is attached as Appendix 1.

## Fourier Transform Analysis of Germanium Spectra

A study has been initiated (with J. Arnold and A. Thakur - UC San Diego) to test the spectral analysis approach that was to be taken with the germanium detector spectra from Mars Observer.<sup>4)</sup> As the satellite was between the Earth and Mars, it was desirable to test the adequacy of the code on realistic data. We realized that a realistic approximation of the spectra that were expected to be obtained by Mars Observer existed from data obtained with a Ge detector<sup>5)</sup> in the German Continental Deep Drilling Project (KTB). The data consisted of gamma-ray spectra from prompt thermal capture and gamma-ray spectra from the decay of delayed radioactivities. Previous work had shown that the peak analysis results were in excellent agreement with data obtained in the laboratory from cuttings and core samples. In the current work, these spectra have been analyzed with a combination of a peak fitting program (GANYMED) and a Fourier transform analysis of the continuum. The results are very encouraging and we hope to compare these results with those obtained from a spline approach that has also been used to include the information in the Compton scattering response from a gamma-ray peak.

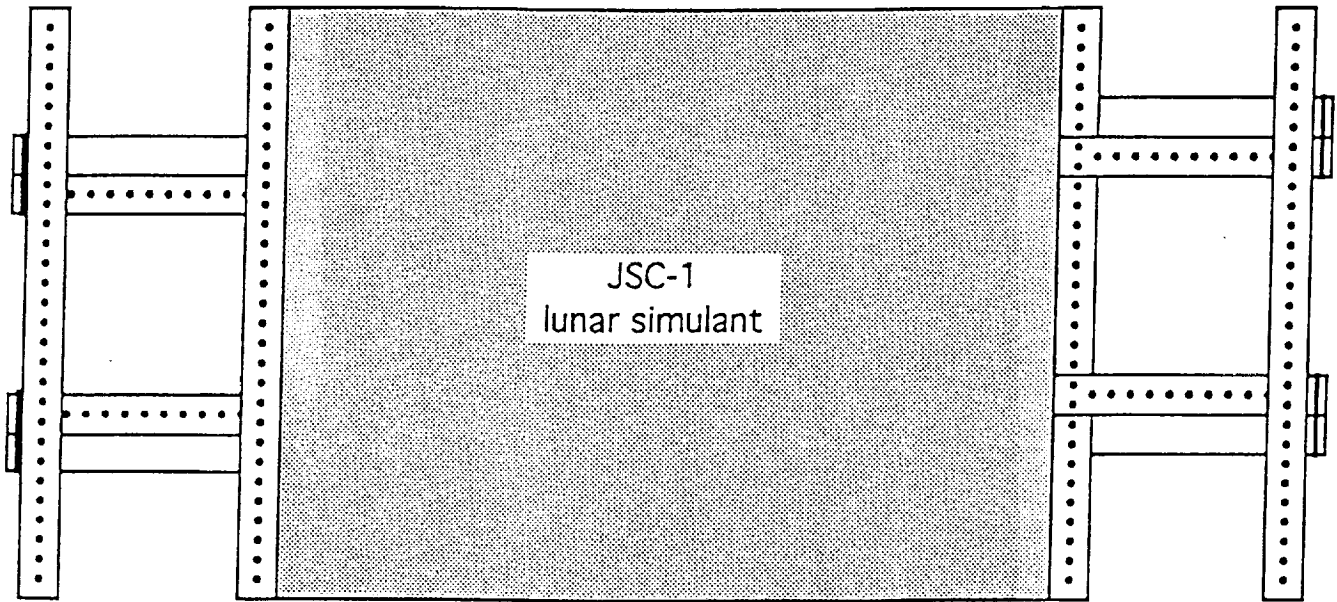
## References

- 1) C.D. Brandle, A.J. Valentino, and G.W. Berkstresser. *Jour. of Crystal Growth* 79 308 (1986).
- 2) K. Takagi and T. Fukazawa. *Appl. Phys. Letters* 42 43 (1983).
- 3) C.L. Melcher and J.S. Schweitzer. *Nucl. Inst. & Meth.* A314 212 (1992).
- 4) A.N. Thakur and J.R. Arnold. *Nucl. Inst. & Meth.* A325 529 (1992).
- 5) J.S. Schweitzer, C.A. Peterson, and J.K. Draxler. *IEEE Trans. Nucl. Sci.* 35(1) 847 (1993).

## Figure Caption

Figure 1. Schematic of planetary detector calibration facility.

top view



side view

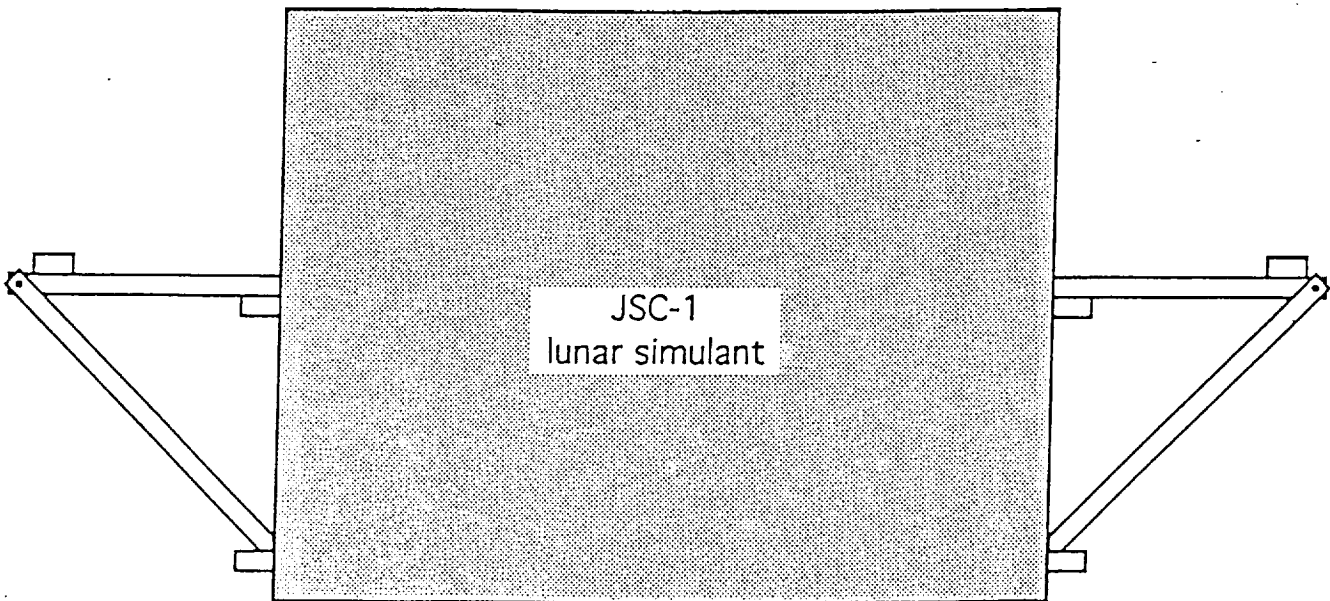


Figure 1

## Survey of Inorganic Scintillators

Although there are many substances known to scintillate under X- or  $\gamma$ -ray irradiation, the ideal scintillator for all applications does not exist, or at least has not yet been found. This ideal material would be:

- fast, similar to the fast component of  $\text{BaF}_2$
- dense for a high  $\gamma$ -ray detection efficiency, as BGO
- high average Z, comparable to BGO
- high light output, such as  $\text{NaI(Tl)}$  or  $\text{CsI(Tl)}$
- good spectral match of emission with a photocathode material, as  $\text{NaI(Tl)}$
- no temperature dependence of the photon yield, as the fast component of  $\text{BaF}_2$
- not hygroscopic
- rugged material
- inexpensive

In the absence of such a material the choice of a scintillator depends on the application and on the choice of the photon converter, i.e. the device which transforms the light of the scintillator into an electronic signal.

The present survey has been initiated to identify an optimized  $\gamma$ -ray detector to detect the  $\gamma$ -ray lines from elements. Thus, the interest is in a spectroscopic detector with as good an energy resolution as possible. The event rate is most often low and speed of the detector may only be sometimes an issue, but detection efficiency is. A high density and a large Z result in a smaller detector. Since the detector is often packaged in an anti-coincidence shield, a smaller detector's the savings in size and weight are amplified by the reduction of this shield.

## List of Inorganic Scintillators

Inorganic scintillators found in the literature are listed in table 1. Although this list is not complete, and there are many more scintillating crystals, most of them might be only interesting for special applications and do not promise to be better in the present search. Besides some well known crystals, there are many exotic materials in the list which are rarely used. From scanning the list, most materials can be easily rejected for this application, since the photon yield is rather low. Although the photon yield is not the only factor, a scintillator with a low light yield cannot provide the desired number of photons required for a good energy resolution. Other scintillators have too low a density or Z to be of interest here. Their efficiency is substantially lower than, for example,  $\text{NaI(Tl)}$  or BGO, a clear disadvantage for space applications.

The most common detectors presently used are  $\text{NaI(Tl)}$  and BGO.  $\text{NaI(Tl)}$  is currently the standard spectroscopy scintillator, but its density and Z are not very high. Therefore, BGO is often chosen where detection efficiency is more important than energy resolution, as for example in anti-coincidence shields. A reduction of candidates in the list is achieved by comparing the characteristics with  $\text{NaI}$  and BGO. A scintillator which does not have the potential to be better suited than either of the two is not worth considering in this context. In particular this means requiring that

either the photon yield is either comparable to or larger than NaI(Tl), or the density and Z are comparable to BGO and the photon yield is larger than the value for BGO. Preserving this artificial classification for the moment, table 2a lists the candidates which may show a better performance than NaI, and table 2b is the equivalent for BGO.

The number of candidates in table 2 is small. One group of interest are the rare earth oxyorthosilicates. Especially, LSO is interesting since the high density and Z provide a scintillator nearly as efficient as BGO, at least above 500 keV. Additionally, the light output is comparable to NaI(Tl), and the decay time is a factor of ten shorter. LSO could be a good spectroscopic detector which is more efficient than NaI(Tl), as well as a superior material for an anticoincidence shield, because of its better energy resolution and timing performance than BGO. These qualities are of special value for high energy gamma rays in order to recover the first and second escape peak.

The second group of interest are scintillators with emission in the red, namely CsI(Tl) and CdWO<sub>4</sub>. Coupled either to red sensitive photocathodes or semiconductor photon converters like Si-diodes, an improved performance can be expected.

The new era of lower cost solar system exploration missions introduces constraints on the options for the science instrument systems. The selected science payload must always meet the resource constraints of the spacecraft and launch vehicle. The size and capabilities of the spacecraft and launch vehicle will most often be selected for their cost. It is also necessary to select the set of instruments that provides the optimum science return within the overall cost and resource constraints. This can mean only a few instruments are flown if expensive innovation is needed in the essential payload, or quality of science return may be sacrificed if existing instrument designs are used. However in some cases there are options for innovative instruments, use of existing designs for some instruments and space craft, and low cost implementation modes that can produce an exceptionally high value science return. This is the case with the proposed Discovery Venera Surface Atmospheric Geochemistry Experiment (SAGE) Mission.

The SAGE mission proposes that a select set of U.S. and Russian built instruments be flown on a Russian built Venus lander of the Vega design with a Russian provided launch vehicle. The proposed instrument set includes a new atmospheric chemical analyzer for descent operation, a surface imaging spectrometer for mineralogical identification, an Alpha Proton X-ray analyzer for elemental analysis of a retrieved sample, and the new Neutron Activation Gamma-Ray Spectrometer (NAGS) for analysis of the Venusian surface in-situ.<sup>1</sup> The APX and NAGS elemental analyzer systems are complementary. The APX system provides elemental analysis of a surface sample obtained by an external drilling system identical to that used on the Venera 13, 14 and Vega 1, 2 landers.<sup>2</sup> The drilling system can retrieve a sample of 1 to 6 cm<sup>3</sup> from the top few centimeters of the surface. The NAGS system on the other hand can provide an analysis of hundreds of cm<sup>3</sup> of the surface without the necessity for retrieving it. Thus a comparison of results can provide an indication of changes in chemistry in the first few centimeters depth due to atmospheric interaction. The APX experiment will determine the abundance of elements from C through Ni with concentrations greater than 1 to 5% by weight. The NAGS system will measure the abundances of H, C, O, Na, Al, Si, S, Ca, Ti, Fe, Gd+Sm, plus Cl and Mg (if present in appreciable quantities) by means of neutron inelastic scattering, capture, and delayed radioactivity. The sensitivity will be better than 0.1% in most cases, with Gd+Sm measured at ppm levels. In addition the natural radioactivities of K, Th and U will be measured at the site. The thick Venusian atmosphere prevents significant cosmic ray induced gamma-ray activation.

## INSTRUMENT SYSTEM

The NAGS instrument is based on the hardware and analytical principles developed by Schlumberger, Inc. for petroleum well logging. The instrumentation consists of a small deuterium-tritium neutron generator (DT minitron), its 80 kV high voltage power supply, a scintillator with a miniature, rugged ceramic photomultiplier tube and amplifier, and control electronics. Schlumberger has developed a number of configurations, but the most suitable one houses all components in lengths of 5.7 cm diameter cylinders that are interconnected and stacked for lowering into a bore hole. The commercial systems are engineered for continuous operation in very harsh down-hole conditions, up to 200° C, hundreds of Gs transient accelerations, and 20,000 lb/in<sup>2</sup> pressures (with steel housing). These basic components can readily be adapted to a number of planetary applications.

For the Venera/SAGE mission, the commercial system, with minor modifications, would be reconfigured and additionally packaged for the Venus surface environment so that it can be deployed from the lander. The instrument will be deployed to a distance of one to two meters by means of an arm that folds out from the side of the lander. The control and data acquisition electronics are divided between the deployed system and the lander. Measurements could be made with the NAGS system fixed at the bottom of the lander, however that position makes it particularly vulnerable to damage on landing, and it maximizes the neutron interaction with the lander, and thus decreases the sensitivity for the geochemical measurements. Deployment to one or two meters will decrease the gamma-ray signal from the spacecraft itself by one or two orders of magnitude.

The harsh Venusian environment, approximately 500 C and 100 atmospheres pressure at the surface, requires extraordinary thermal and mechanical designs for the lander and externally deployed instruments. Despite the inclusion of extensive thermal insulation and heat absorbers, the Venera and Vega landers are limited to, at most, two hours of surface operations. Preliminary analyses indicate that the NAGS system can be made to last two hours using the packaging system illustrated in Figure 1. The primary insulation is a metal vacuum dewar that completely

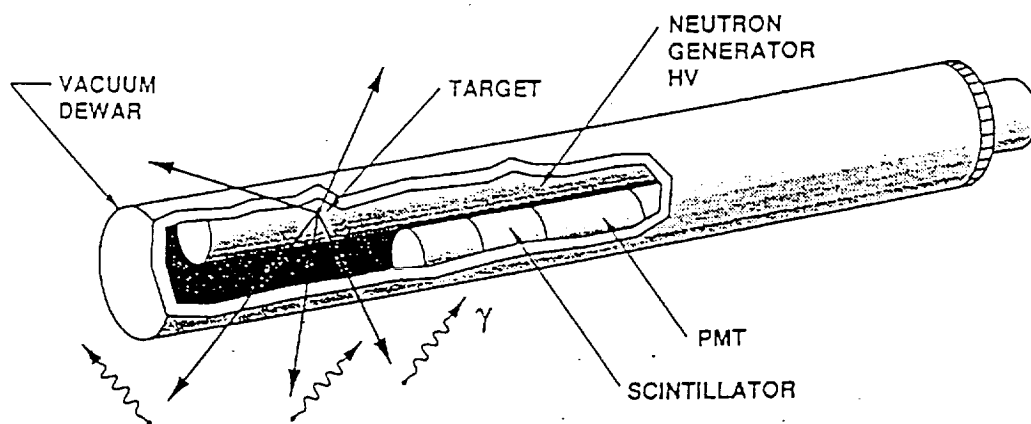


Figure 1. Schematic of packaging system for the NAGS in Venus environment

contains the neutron generator, spectrometer and electronics. Overall the dewar is about 1 meter long and 15 cm in outside diameter, 11 cm inside diameter. The vacuum wall contains high temperature multilayer insulation. The power and signal lines are carried through insulated connectors at one end. In order to limit the temperature rise rate, the voids within the inner dewar wall are filled with a heat absorbing phase-change material. Because the logging systems are mechanically and electrically designed for harsh deep-well conditions, no significant re-engineering of the generator and spectrometer systems is anticipated. The complete system would have a mass of about 27 kg including the thermal packaging. Approximately 30 W would be consumed to maximize neutron output for the operating period. This mass and power is well within the capability of a Vega lander to deliver and operate. For a less severe planetary environment, such as Mars, the neutron probe system mass and power requirement would be less by, perhaps, an order of magnitude.

In well logging applications the neutron generator and gamma spectrometer systems are in one linear string with neutron scattering material between them to minimize line-of-sight neutron interaction. However a completely in-line system would be too long to be accommodated on a Venera/Vega lander. Thus the neutron generator with its power supply are placed beside the spectrometer system with the scattering material close to the scintillator. This is still excellent geometry.

Clearly there are important similarities and differences between using the NAGS system in a petroleum well and on the surface of a planet, Venus in particular. In both cases, the system must be mechanically and electrically rugged. In both cases the system must produce high quality spectral data under extreme mechanical stress and rapid temperature changes. The ability to perform well under these conditions is fundamental to the existing commercial logging systems.

The two most important differences between well logging and the planetary system are the geometry and the amounts of neutron moderator present. In a well logging application, the neutrons are interacting with rock that is nominally in  $4\pi$  geometry around the source and detector, whereas in the case of the surface location, the material to be analyzed is only in one hemisphere. This has the effect of decreasing the overall sensitivity of measurements because approximately half the neutrons will never interact with the solid surface, and additional neutrons will be scattered out of the solid before they are captured.

The second major difference from well logging is the relative amounts of neutron moderator present. In well-logging applications the generator is always surrounded by significant concentrations of hydrogen-containing fluids such as water and hydrocarbons. These act to very efficiently slow down the neutrons so that they are captured within a few tens of centimeters from the generator. Thus the gamma ray signal from neutron capture is strong in a scintillator close to the generator. On the other hand, on Venus or other "dry" planets there is little or no hydrogen present so that the neutrons may travel several times farther before they are captured. Thus the optimum capture signal may be obtained farther from the generator.

### Data Acquisition

The data acquisition strategy as been well developed for the well logging applications, and an essentially similar strategy is used for a planetary application.<sup>3</sup> The gamma-ray signal at the spectrometer detector contains components from neutron inelastic scattering, neutron capture, and delayed radioactive decay. The separation of these components can enhance the sensitivity for some elements. Although the gamma ray spectrum from each element is unique, when the spectrum is derived from a relatively low resolution detector, such as the scintillator system, the lines are not uniquely resolved and separation of components is a considerable advantage. Thus the strategy is to measure the gamma rays as a function of time following a microsecond burst of neutrons. The inelastic scattering of the primary 14 MeV neutrons,  $(n,n')$  reactions, results in immediate emission of gammas from the excited nuclei. The capture of the neutrons by target nuclei,  $(n,\gamma)$  reactions, results in prompt emission of gamma rays, but there is a delay of some microseconds between emission of the primary neutrons and the capture because capture is more

likely for slow neutrons. The emission of gammas by decay of activated nuclei is statistically delayed by the half life of the nucleus.

A typical data acquisition scenario is as follows. The neutron generator is pulsed on for about 10 microseconds every millisecond. A "pulse gate" gamma spectrum is accumulated during the pulse. This spectrum is dominated by (n,n') reactions. Then a "capture" spectrum is accumulated for a few hundred microseconds. This spectrum is dominated by the (n, $\gamma$ ) reactions. Then, perhaps with some hundreds of microsecond delay, the "delay activation" spectrum is accumulated for a few hundred microseconds. This spectrum is dominated by decay of radioactive nuclei. The intercomparison of these spectra, and subtraction of various components allows analysis for H, C, O, Na, Al, Si, S, Ca, Ti, Fe, Gd+Sm, plus Cl and Mg (if present in appreciable quantities) with sensitivities of better than 0.1% for most components and Gd+Sm with ppm sensitivities. The quantitation process has been described elsewhere.<sup>4,5</sup>

### EXPERIMENTAL TESTS

A number of laboratory experiments were performed to investigate the quality of the spectra that could be obtained on the Venusian surface by a neutron generator (output  $> 10^8$  n/sec) with a 3.5 cm diameter x 7.5 cm cerium-doped gadolinium oxyorthosilicate (GSO) gamma-ray detector. Simulations of the Venusian surface were made in a 68 cm x 99 cm x 75 cm polyethylene container. Initial measurements were made with a CaCO<sub>3</sub>-filled or SiO<sub>2</sub>-filled container. These measurements were intended to evaluate the effects of the CO<sub>2</sub> atmosphere on the shape of the spectra and to "salt" the formation with individual elemental compounds to evaluate the spectral shapes for each individual element. Subsequently, a simulation of the Venusian surface was constructed to provide a close approximation of the elemental content from the results obtained by Venera 14.<sup>6</sup> The elemental content of the resultant simulation is compared with the Venera 14 results in Table 1.

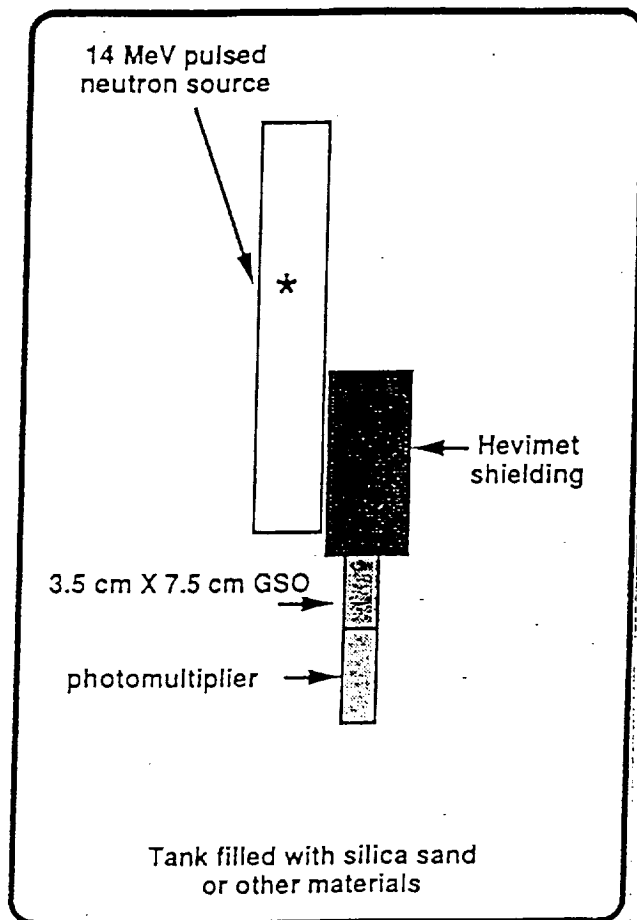


Figure 2. Schematic drawing of the top view of the laboratory experimental setup.

All measurements were performed with the neutron generator, shielding, and the detector-photomultiplier combination lying on the surface of the formation, as shown schematically in Figure 2. Since the Venusian environment is characterized by being essentially hydrogen free, the

slowing down and diffusion properties of neutrons are controlled by the other light elements present, rather than hydrogen as is usually the case on Earth. As there is uncertainty on how much of the CO<sub>2</sub> atmosphere may permeate the Venusian soil and on whether there will be a portion of the atmosphere between the neutron generator and the detector and the soil being measured, we attempted to evaluate the effect of the variation of neutron moderation properties on detected gamma-ray spectral shapes by comparing simple spectra obtained with and without substantial CO<sub>2</sub> present. Spectra were obtained by placing the neutron generator and detector directly on the SiO<sub>2</sub> soil surface and by repeating the measurement with a 5 cm layer of solid CO<sub>2</sub> between the neutron generator and detector and the soil surface.

To provide an estimate of the spectral shape for individual elements, packages, containing typically 1 kg of individual element oxides or carbonates, were placed about 10 cm beneath the CaCO<sub>3</sub> soil surface between the neutron generator and the GSO detector. The resulting spectra will provide individual spectral response functions after subtracting the contribution from the common CaCO<sub>3</sub> content.

Table 1. Comparison between elemental content determined by Venera 14 and the laboratory Venusian simulant.

Element	Venera 14 Measurements (wt percent)	Venusian Simulant (wt percent)
Magnesium	4.9	4.3
Aluminum	9.5	7.9
Silicon	22.7	19.5
Potassium	0.17	0.65
Calcium	7.4	7.2
Titanium	0.75	0.75
Manganese	0.16	0.12
Iron	6.8	6.8
Sulfur	0.35	0.27
Chlorine	0.4	0.42
Oxygen	43.6	47.5
Carbon	-	4.3
Sodium	-	0.28
Unknown	3.3	-

All electronics for processing the detector outputs used standard laboratory electronics. Spectra to reflect the fast neutron-induced gamma rays, those due to thermal neutron capture reactions, as well as the spectrum of gamma rays from the decay of delayed radioactivity were obtained by gating the detector electronics with signals from the pulse from the neutron generator.

## RESULTS

The test of the effect of the CO<sub>2</sub> atmosphere can be seen in the capture spectra shown in Figure 3. If there were significant changes introduced by the CO<sub>2</sub> atmosphere, then a change in

the peak height to scattered background would be expected. The figure shows the gross thermal neutron capture gamma-ray spectrum without any CO<sub>2</sub> present (dashed curve) with the corresponding spectrum obtained with the 5 cm of CO<sub>2</sub> between the equipment and the formation surface (solid curve). The only significant change in the spectral shape is from the additional oxygen activation photopeaks (the triplet at roughly 6, 5.5 and 5 MeV) and the Compton background to lower energies from these peaks. In the region of the silicon thermal neutron capture gamma-rays, there is no significant change in the peak or background portion of the spectrum when the solid CO<sub>2</sub> is introduced. Thus the shape of the gamma-ray standards are expected to be minimally perturbed by the exact amount of CO<sub>2</sub> atmosphere present during the measurement, indicating that this factor would probably not be an important limit on the accuracy of derived elemental concentrations.

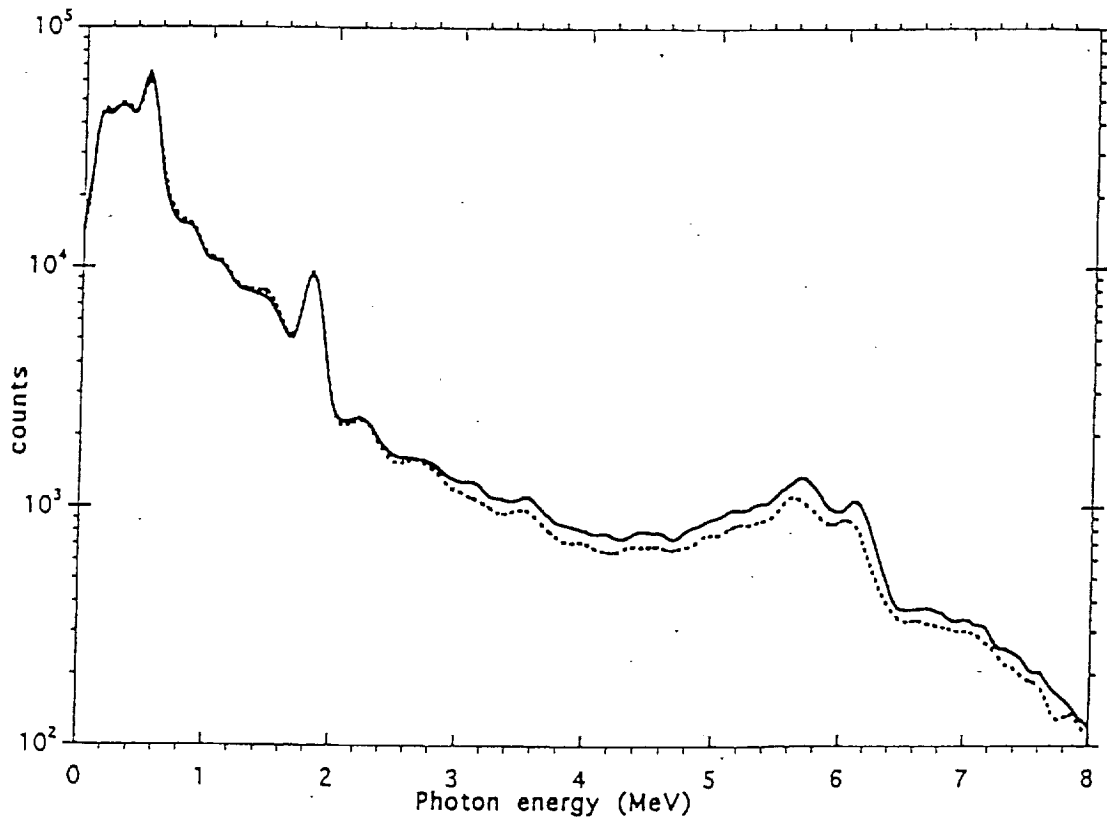


Figure 3. Comparison between thermal neutron capture gamma-ray spectra obtained on a quartz formation with (solid curve) and without (dashed curve) CO<sub>2</sub> between the surface and the instrument.

Two typical neutron capture gamma-ray spectra are shown in Figures 4 and 5 where TiO<sub>2</sub> and Fe<sub>2</sub>O<sub>3</sub> are salted in the CaCO<sub>3</sub> matrix. In both cases the contributions from the added elements can be clearly identified. These spectra confirm that elemental standards could be derived for the response of the spectrometer to individual elements contained in the measurement volume.

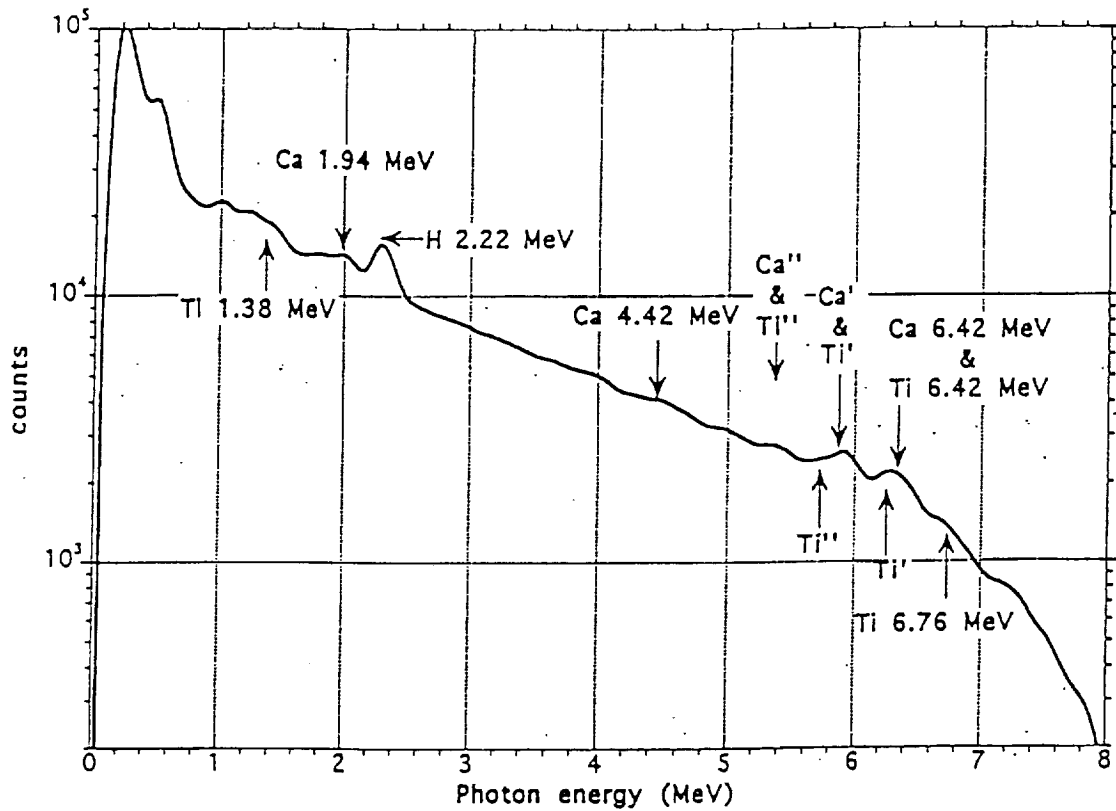


Figure 4. Thermal neutron capture gamma-ray spectrum when the calcite simulation is "salted" with  $\text{TiO}_2$ .

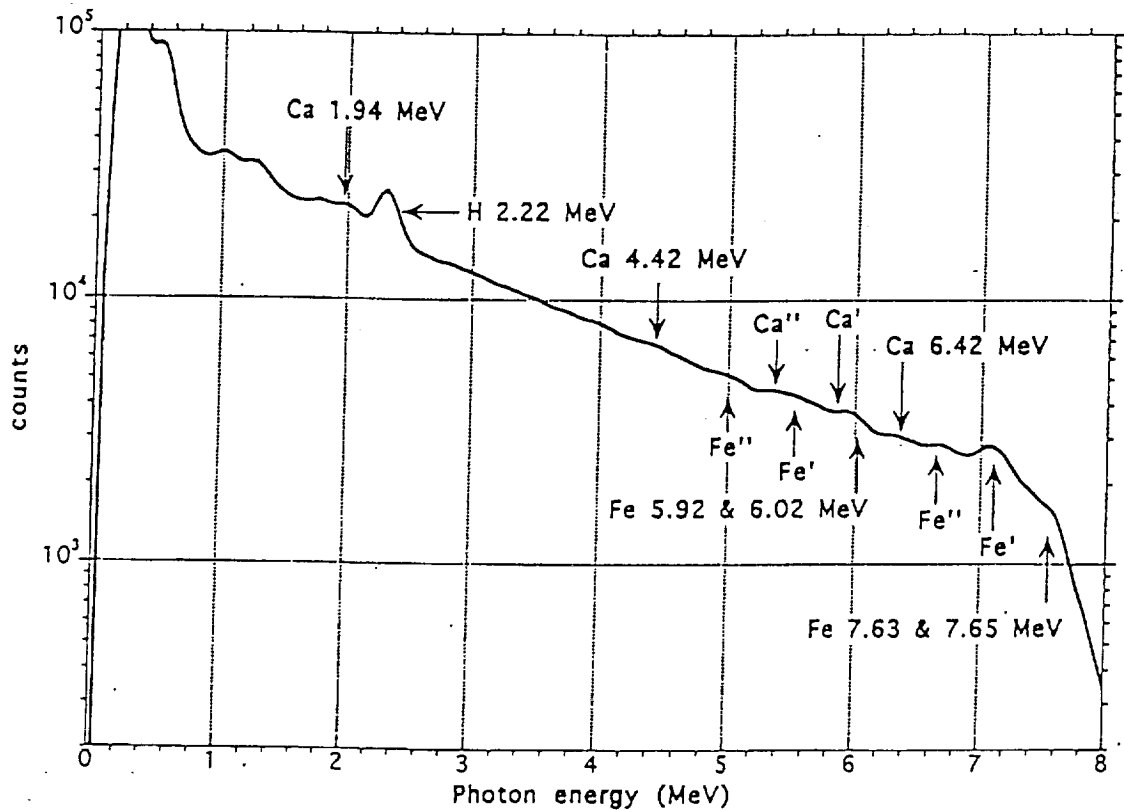


Figure 5. Thermal neutron capture gamma-ray spectrum when the calcite simulation is "salted" with  $\text{Fe}_2\text{O}_3$ .

Figure 6 shows a thermal neutron gamma-ray capture spectrum obtained with boron surrounding the detector to minimize the spectral contribution from the detector package. This spectrum was obtained in the complete simulation, whose elemental content is shown in Table 1. Numerous peaks can be identified from the elements in the simulation, indicating that these elements, as well as perhaps some of the others whose peaks are not visually obvious, can be quantitatively determined. It should be noted, of course, that some of the elements would be determined from prompt neutron-induced reactions, such as carbon, oxygen, and magnesium, and from delayed radioactivity, such as aluminum, manganese, and sodium.

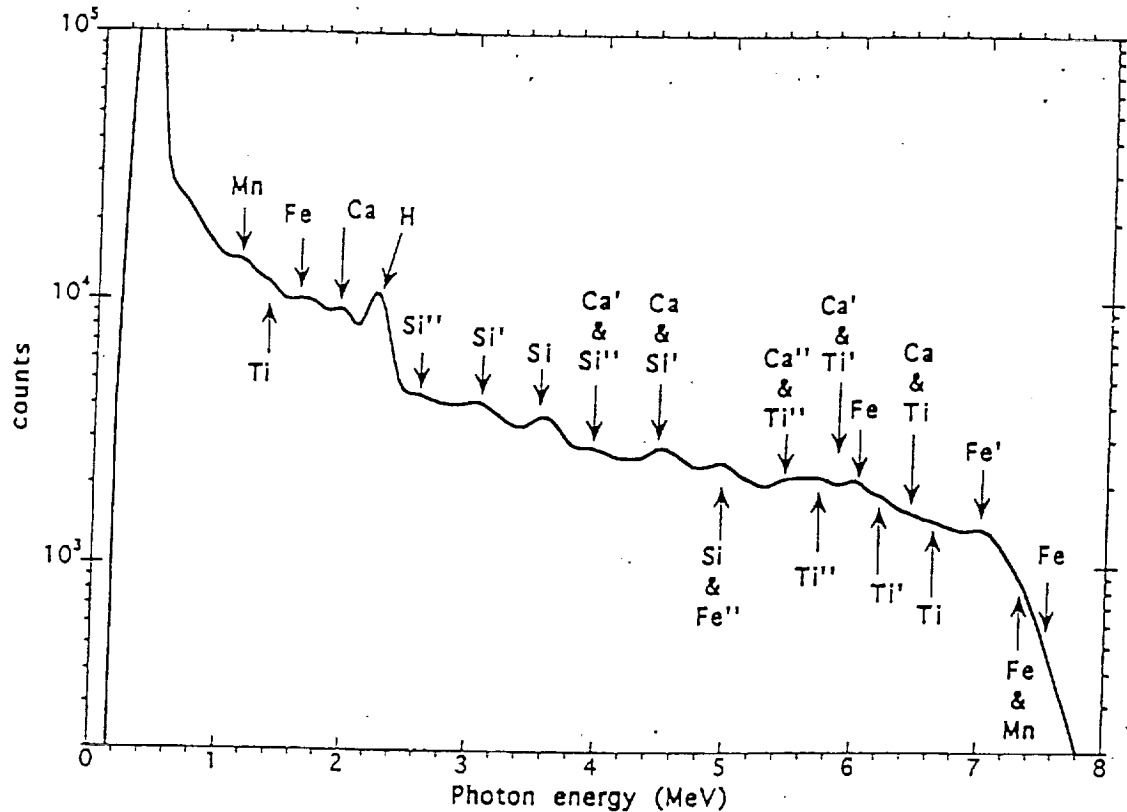


Figure 6. Thermal neutron capture gamma-ray spectrum in the complete simulant model whose composition is given in Table 1. The hydrogen peak is from the environment surrounding the simulant.

## DISCUSSION

The technique of using a gamma-ray detector together with a pulsed neutron generator to determine accurate elemental abundances has been well developed for remote sensing applications on Earth in rugged environments. Such systems can be applied to non-orbital planetary environments to provide elemental concentrations of the surface constituents averaged over the first tens of centimeters in depth. In an impact scenario a volume of tens of centimeters in radius around the probe location can be analyzed. The particular choice of system components for planetary missions is governed by the particular mission environment. The selection of GSO for the Venusian measurement is based on its properties at elevated temperatures<sup>7</sup> where it can maintain a good light output with an acceptably fast scintillation light decay constant over the

entire range of anticipated measurement temperatures. In addition, it provides a good volumetric detection efficiency, minimizing the size of the dewar while maintaining a good gamma-ray spectral response. For a colder environment, a better choice might be cerium-doped lutetium oxyorthosilicate<sup>8</sup> which has a faster decay time, essentially the same volumetric detection efficiency as BGO and has essentially constant output and time characteristics between 11 K and room temperature, providing better spectral stability and easier electronics design. Of course, in situations where no neutron generator is provided (i.e., using cosmic rays to induce the reaction gamma rays) other detectors such as BGO may be more than adequate. When extensive multielement analysis is required, a neutron generator can be coupled with a germanium detector for optimum energy resolution and detection sensitivity.

The data presented here are not sufficient for making accurate predictions of anticipated statistical uncertainties or minimum detection limits for the Venera measurement. However, experience has indicated that when even a hint of spectral peaks can be seen in the measured spectrum acceptable precision can be obtained for the elements that make a reasonable spectral contribution to the measurement. In fact, it is possible to quantify elemental concentrations at reasonable levels of precision even when there is no visual indication of specific peaks. Laboratory measurements can be used to predict quantitatively the performance of such a system under a particular planetary measurement environment<sup>9</sup>, but resources were not available to perform the complete study here.

These measurements do confirm, however, that the use of a gamma-ray detector with pulsed neutron generator in the Venusian environment can perform a significant elemental analysis to provide greater insight into the nature of the surface rocks on the planet. The application of this technique to planetary environments with significantly different surface constituents, such as comets, is currently being evaluated.

#### ACKNOWLEDGMENTS

This work was sponsored, in part, by the Director's Discretionary Fund of the Jet Propulsion Laboratory, California Institute of Technology. Significant in-kind support was provided by Schlumberger-Doll Research for the work performed in their facilities. The work described was performed, in part, at the California Institute of Technology, at the Jet Propulsion Laboratory, California Institute of Technology and at Schlumberger-Doll Research.

#### REFERENCES

1. J.W. Head, III, Discovery Venera Surface Atmosphere Geochemistry Experiments, Proposal to the Discovery Missions Workshop, San Juan Capistrano, Calif., 9 Sept. 1992.
2. I.V. Barman and A.A. Shevchenko, Soil Scooping Mechanism for the Venera 13 and Venera 14 Unmanned Interplanetary Spacecraft, *Cosmic Research*, Vol. 21, No. 2, 118-122, 1983.
3. J.S. Schweitzer, Nuclear Techniques in the Oil Industry, *Nucl. Geophys.*, Vol. 5, No. 1/2, 65-90, 1991.

4. R.C. Hertzog, Laboratory and Field Evaluation of an Inelastic Neutron Scattering and Capture Gamma Ray Spectroscopy Tool, Soc. Petr. Eng. Jour., Vol. 20, 327-340, 1980.
5. R.C. Hertzog, et al, Geochemical Logging with Spectrometry Tools, Tech. Symp. Soc. Petr. Eng., Dallas, Paper SPE16792, 1987.
6. Y.A. Surkov, L.P. Moskaleva, O.P. Shcheglov, V.P. Kharyukova, and O.S. Manvelyan, Elemental Composition of Rocks on Venus, Cosmic Research, Vol. 21, No. 2, 241-251, 1983.
7. C.L. Melcher, J.S. Schweitzer, R.A. Manente and C.A. Peterson, Applicability of GSO Scintillators for Well Logging, IEEE Trans. Nucl. Sci., Vol. 38, No. 2, 506-509, 1991.
8. C.L. Melcher and J.S. Schweitzer, A Promising New Scintillator: Cerium-Doped Lutetium Oxyorthosilicate, Nucl. Instr. & Meth. in Phys. Research, Vol. A314, 212-214, 1992.
9. J.A. Grau, J.S. Schweitzer and R.C. Hertzog, Statistical Uncertainties of Elemental Concentrations Extracted from Neutron-Induced Gamma-Ray Measurements, IEEE Trans. Nucl. Sci., Vol. 37, No. 6, 2175-2178, 1990.

## **Appendix 2**

### **The Role of Gadolinium in the Scintillation Processes of Cerium Doped Gadolinium Oxyorthosilicate**

PRECEDING PAGE BLANK NOT FILMED

# The role of gadolinium in the scintillation processes of cerium-doped gadolinium oxyorthosilicate

H. Suzuki<sup>a,1,\*</sup>, T.A. Tombrello<sup>a</sup>, C.L. Melcher<sup>b</sup>, C.A. Peterson<sup>b</sup>, J.S. Schweitzer<sup>b</sup>

<sup>a</sup> Division of Physics, Mathematics, and Astronomy, California Institute of Technology, Pasadena, CA 91125, USA

<sup>b</sup> Schlumberger-Doll Research, Ridgefield, CT 06877-4108, USA

(Received 24 January 1994)

The origins of two decay constants in the scintillation decay of cerium-doped gadolinium oxyorthosilicate ( $Gd_2(SiO_4)O:Ce$ ) are investigated using UV light. We find that build-ups and long decay components observed with gamma-ray excitation are due to non-radiative energy transfer from Gd to Ce. The transfer rate from Gd to Ce increases as the Ce concentration increases. The gamma-ray excited decay curves of GSO are composed of prompt Ce emission and delayed Ce emission (transfer of energy through Gd), as observed by UV excitation.

## 1. Introduction

The scintillation properties of Ce-doped gadolinium oxyorthosilicate  $Gd_2(SiO_4)O:Ce$  (GSO) are characterized by a relatively high emission intensity (25% of NaI(Tl)), two decay constants ( $\sim 56$  and  $\sim 600$  ns for 0.5 mol% Ce-doped GSO), an emission peak at 430 nm and emission intensities and decay times that depend on the Ce concentration [1,2]. The blue emission of GSO entirely originates from the  $Ce^{3+}$  activator, which has parity allowed electric-dipole transitions between the excited 5d states and the spin-orbit split 4f ground state.

When GSO is excited with high energy particles such as gamma rays or X-rays, the scintillation processes of GSO can be separated into two parts [3]: primary and secondary processes. The primary process is the transfer of energy from ionizing radiation to the luminescent centers ( $Ce^{3+}$ ). The secondary process is that by which excited luminescent centers lose their energy. The secondary process of GSO has been studied [4] independently as a function of temperature (11–300 K) by direct excitation of the luminescent centers, with ultraviolet excitation instead of with ionizing radiation. The existence of two activation centers (Ce1 and Ce2) has been proposed [4] because  $Gd_2(SiO_4)O$  has two crystallographically independent  $Gd^{3+}$  sites [5,6].

In our previous work [4] we studied the excitation and emission bands, the decay constants, and the temperature dependence of the two Ce centers. That work showed that

the Ce1 center has its two lowest energy absorption bands at 284 and 345 nm, and an emission band at 425 nm. The decay constant of  $Ce^{3+}$ , which is obtained by a direct excitation into the  $Ce1^{3+}$  absorption bands, is 27 ns at 77 K, and it becomes faster (22 ns) at room temperature due to an increase in the non-radiative transition rate (as a result of thermal quenching). It was also shown that the two lowest absorption bands of  $Ce2^{3+}$  are located at 300 and 378 nm and the emission band is at 480 nm. The  $Ce2^{3+}$  has a decay constant of 43 ns at 77 K; this decay constant becomes much faster ( $< 6$  ns) at room temperature because of strong thermal quenching. Thus the emission of GSO following gamma-ray excitation at room temperature is dominated by the emission from the  $Ce1^{3+}$  luminescent center.

The emission peak of GSO with room temperature gamma-ray excitation agrees well with the emission peak of Ce1 and it supports the assumption that most emission comes from the Ce1 center. However, the two decay constants,  $\sim 56$  and  $\sim 600$  ns [2], obtained with gamma-ray excitation are much slower than the decay constant of the Ce1 center itself (22 ns) [4]. This difference in the decay time between UV excitation and gamma-ray excitation suggests that the primary scintillation process of GSO is slower than the secondary process and that there are at least two types of primary processes which produce two decay constants. Thus the existence of two decay constants observed in gamma-ray excited GSO can be attributed to the primary excitation process.

In the current study, to investigate the primary excitation process of GSO,  $Gd^{3+}$  absorption lines in the UV region were excited by a synchrotron light source and the decay of the emissions from  $Ce^{3+}$  were monitored. We

\* Corresponding author.

<sup>1</sup> Present address: Schlumberger-Doll Research, Ridgefield, CT 06877-4108, USA

attempted to correlate the results obtained from the UV excitation with those from the gamma-ray excitation, and the origins of two decay constants in the gamma-ray excited decays were studied.

Crystallographically,  $Gd_2(SiO_4)O$  has a monoclinic structure of space group  $P2_1/c$ . There are two Gd sites in  $Gd_2(SiO_4)O$ : one Gd site has a ninefold oxygen coordination, and the other site has a sevenfold oxygen coordination. The mean distance from the former Gd site to the nine oxygen ligands is 2.49 Å, while that from the latter site to the seven oxygen ligands is 2.39 Å. Due to the different interactions with the crystal field and the lattice, the two  $Gd^{3+}$  ions are expected to show slightly different optical properties in interacting with the two  $Ce^{3+}$  ions (Ce1 and Ce2). However, in the discussion below where the interaction of  $Gd^{3+}$  with  $Ce^{3+}$  is macroscopically treated, no distinction will be made between the two  $Gd^{3+}$  ion sites, as we do not propose to describe the details of the spectroscopic properties of GSO. Rather we attempt to understand the primary process to provide a comprehensive explanation of the scintillation processes of GSO.

## 2. Experimental measurements

The GSO crystals used for this study were obtained from Hitachi Chemical Co., Ltd., which grew the GSO crystals by the Czochralski technique. The Ce concentration in the melts from which the crystals were grown varied from 0.1 to 2.5 mol%. However, the Ce concentrations in the crystals depends on the distribution coefficient of Ce in the host material  $Gd_2(SiO_4)O$ . The Ce concentrations in the crystals were analyzed by X-ray Assay Labora-

tories and the distribution coefficient of Ce was determined to be  $\sim 0.6$ , in reasonably good agreement with previous studies [7]. Six GSO samples ( $(Gd_{1-x}Ce_x)_2(SiO_4)O$ ) were used in this study. Their Ce concentrations relative to Gd are: sample No. 1 (nominal 0.1 mol%,  $x = 0.00035$ ), No. 2 (0.5 mol%, 0.0018), No. 3 (1.0 mol%, 0.0036), No. 4 (1.5 mol%, 0.0051), No. 5 (2.0 mol%, 0.0074) and No. 6 (2.5 mol%, 0.0098).

The absorption spectra were measured with a spectrophotometer (Model U-3210, Hitachi Instruments). The emission spectra were obtained with a SPEX Fluorolog-2 spectrofluorometer. The details of these optical measurements as well as those of the gamma-ray excited decay curve at room temperature have been described elsewhere [4].

The low-temperature measurements of the gamma-ray excited decay curves were made with the configuration shown in Fig. 1. Temperatures as low as 15 K were achieved with a CTI-Cryogenics refrigeration system (Model 21). The decay data were taken using the time-correlated single-photon technique [8], with a  $^{22}Na$  source and a second crystal to provide a timing reference [9]. The reference signal was produced by cerium-doped lutetium oxyorthosilicate  $Lu_2(SiO_4)O:Ce$  (LSO), which has a very high light output and a primary decay constant of 40 ns [10,11]. The GSO crystal was excited from the side. Two 511 keV gamma rays, simultaneously produced by annihilation of a positron and an electron, were used to excite both GSO and the reference LSO scintillator. All the gamma-ray excited decay curves shown here were measured without correcting for the wavelength dependence of the photocathode on the photomultiplier tube. One of two filters, S40-400 or LL-600 (Corion), was placed between

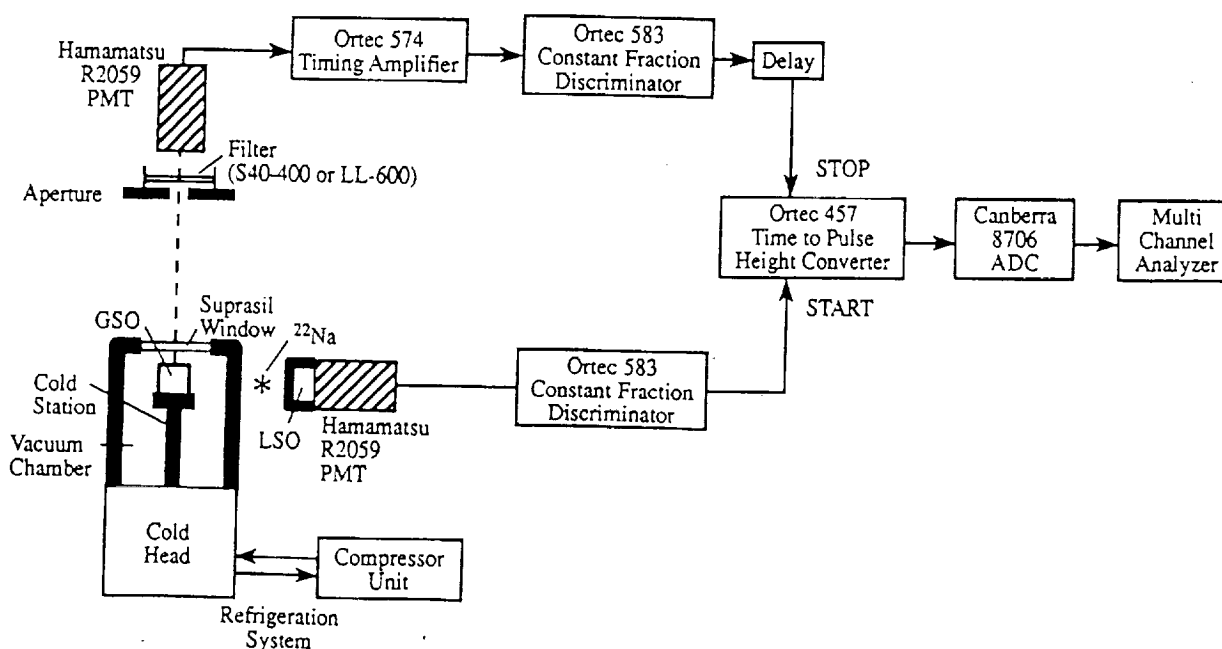


Fig. 1. Equipment and electronics used to measure gamma-ray excited decay curves at 15 K.

the GSO crystal and its photomultiplier tube to select either Ce1 or Ce2 emission. The bandpass filter S40-400 has a peak at  $\sim 400$  nm and transmits only Ce1 emission. The long wave pass filter LL-600 transmits photons which have wavelengths longer than 600 nm and is suitable for selecting only Ce2 emission.

The measurements of UV-excited decay curves as well as those of UV-excited excitation spectra were made by using the U9B beam line of the National Synchrotron Light Source at Brookhaven National Laboratory. For the former measurements, we used the single bunch mode, whose duration time is  $\sim 1.0$  ns. This light source has a repetition rate of  $\sim 5.88$  MHz, i.e., a beam repetition period of  $\sim 170$  ns. Because of the short beam period, longer decay constants than the beam period could not be measured. For the measurements of the UV-excited excitation spectra, we used the normal periodic bunch mode to get enough intensity from the light source. Monochrometers were used to select the excitation and emission wavelengths. The bandpasses of excitation and emission monochrometers were 1.7 and 10 nm, respectively. The UV-excited decay data were also taken using the time-correlated single-photon technique and were analyzed with a least-squares-fitting technique.

In the discussion below each GSO sample is labeled by its sample name, its Ce concentration in the melt or its Ce concentration in the crystal (e.g. No. 1, 0.1 mol% or 0.00035). However, neither the charge state of Ce in the crystal nor the exact concentration of each Ce center (Ce1 and Ce2) has been determined.

## Results

### 1. Comparison between UV and gamma-ray excitation

Fig. 2 shows the decay curves of  $Ce^{3+}$  on a relatively short time scale for various GSO samples excited by gamma rays. Counts are plotted on a logarithmic scale. To choose Ce1 emission, whose emission peaks at 425 nm, the S40-400 bandpass filter was placed between the crystal and the stop photomultiplier tube. This bandpass filter transmits only Ce1 emission, eliminating Ce2 emission, whose emission peak is at 480 nm. The Ce1 decay from 0.1 mol% GSO obtained with direct UV excitation into the  $Ce^{3+}$  band is also displayed in Fig. 2. The excitation and emission wavelengths were 284 and 420 nm. As can be seen, the Ce1 decays with gamma-ray excitation are much slower than the decay of Ce1 itself (22 ns). The decay constants with gamma-ray excitation decrease as Ce concentration increases from 0.1 to 2.5 mol%. Note that the gamma-ray excited decay curves of all GSO samples, when viewed with this time resolution, contain initial build-ups, indicating that the decay curve obtained with gamma-ray excitation cannot be described by a simple

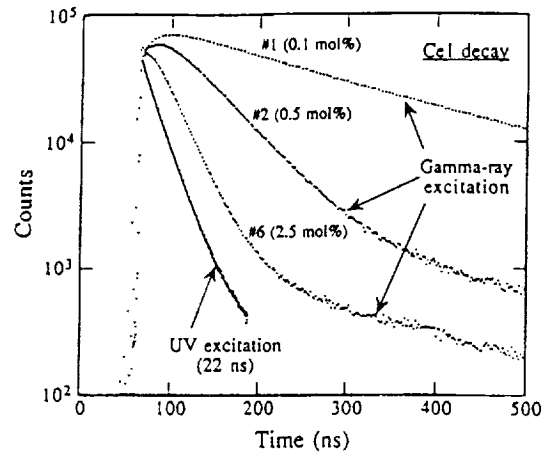


Fig. 2. Gamma-ray excited decay curves of three GSO samples and the UV excited decay curve of 2.5 mol% GSO. The latter curve has an excitation wavelength of 284 nm and an emission wavelength of 420 nm.

summation of two exponentials. The extent of this build-up, in addition, strongly depends on the Ce concentration.

Fig. 3 shows the Ce1 decay constant for various GSO samples with different Ce concentrations. The decay data were obtained with an excitation wavelength of 284 nm and an emission wavelength of 420 nm. The decay constants were calculated from a single exponential fit. The decay constant of Ce1 changes slightly from 25 ns for 0.1 mol% GSO to 22 ns for 2.5 mol% GSO. This trend of the Ce1 decay constant, i.e., a weak concentration dependence of the decay, has been previously reported [12]. Note that the strong dependence of the gamma-ray excited Ce1 decay on Ce concentration differs from that of the UV-excited (at 284 nm) Ce1 decay, which shows only a weak dependence on Ce concentration.

Since the observed decay constants of GSO with gamma-ray excitation are much longer than the decay constant of Ce1 itself, the primary process must be relatively slow. By analogy with thallium-doped sodium iodide NaI(Tl) [3], five processes in exciting the luminescent center ( $Ce^{3+}$ ) following the interaction of high energy particles are possible:

- 1) luminescence by the lattice centers ( $Gd^{3+}$ ) and absorption by the luminescent center ( $Ce^{3+}$ ) (radiative transfer);
- 2) non-radiative energy transfer from the excited lattice centers ( $Gd^{3+}$ ) to the luminescent centers ( $Ce^{3+}$ ) (including resonant transfer);
- 3) non-radiative transfer from vacancies or traps to the luminescent center ( $Ce^{3+}$ );
- 4) exciton diffusion to the luminescent center ( $Ce^{3+}$ ); and
- 5) binary (independent) diffusion of electrons and holes to the luminescent center ( $Ce^{3+}$ ).

Processes 1) and 2) will be discussed below. The possibility of the other processes will be discussed in the next section.

The  $Gd^{3+}$  ion has 7 electrons in the 4f shell, which is well shielded from the crystalline environment by two electronic shells with larger radial extension ( $5s^25p^6$ ) [13]. As a result,  $Gd^{3+}$  shows very sharp 4f–4f transitions in the UV, with wavelengths that are relatively independent of the particular Gd compound [14–19]. The transition between two 4f states of  $Gd^{3+}$  depends on both forced electric dipole radiation and magnetic dipole radiation. The electric dipole radiation is forbidden in first order and it occurs only as a consequence of a perturbation. The magnetic dipole radiation, which is about six orders of magnitude weaker than the electric dipole radiation in free atoms, is observed in the  $Gd^{3+}$  spectra from crystals with about the same intensity as the electric dipole radiation.

The absorption data for undoped  $Gd_2(SiO_4)O$  is shown in Fig. 4a. The thickness of the sample was 0.040 cm. The absorption coefficients  $\alpha$  ( $cm^{-1}$ ) are calculated using the formula  $I = I_0 \exp(-\alpha l)$ , where  $I$  and  $I_0$  indicate the intensity of the transmitted and incident light, respectively, and  $l$  is the thickness of the crystal (cm). The undoped GSO spectrum has absorption lines at 313, 308 and 302 nm, which are ascribed to the transitions from the ground  $^8S_{7/2}$  state to the three excited states  $^6P_{7/2}$ ,  $^6P_{5/2}$  and  $^6P_{3/2}$ . The absorption line at 275 nm is due to transitions from the ground  $^8S_{7/2}$  state to the  $^6I_J$  multiplets ( $J = 7/2, 9/2, 17/2, 11/2, 15/2,$  and  $13/2$ ). The excitation into the  $^6D_{9/2}$  state from the ground  $^8S_{7/2}$  state is seen at 254 nm, and the excitations into the other  $^6D_J$  multiplets ( $J = 1/2, 7/2, 3/2$  and  $5/2$ ) are observed at 247 nm. The small peak at 203 nm is due to the absorption of  $^6G_J$  ( $J = 7/2, 9/2, 11/2$  and  $5/2$ ) multiplets [20]. The lattice absorption begins at  $\sim 200$  nm.

The emission lines of  $Gd^{3+}$  in undoped GSO were observed at 278 (from the  $^6I_J$ ) and 314 nm (from the  $^6P_J$ ) with gamma-ray excitation (500  $\mu Ci$   $^{241}Am$  source) (Fig. 4b). The emission bandpass was 7.2 nm. Note that the emission wavelengths are almost identical with the absorp-

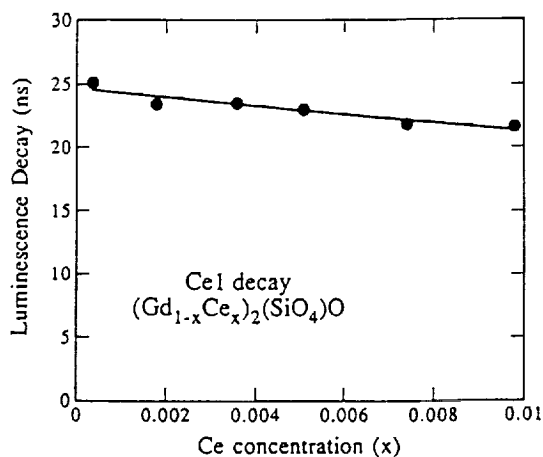


Fig. 3. UV-excited luminescent decay of Ce1 as a function of the total Ce concentration ( $x$ ). The emission and excitation wavelengths were 284 and 420 nm, respectively.

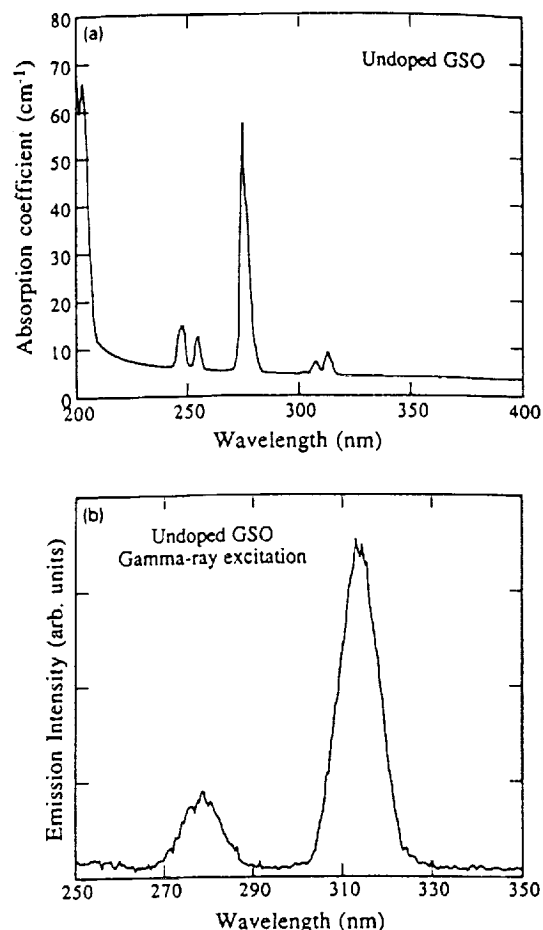


Fig. 4. Absorption (a) and emission (b) spectra of undoped GSO.

tion wavelengths. The ground state emissions from higher excited states were not seen. This is probably because the non-radiative decay rates from the higher excited states to the lower excited states ( $^6I_J$  and  $^6P_J$ ) are much greater than the radiative decay rates to the ground state and deplete the higher excited states.

The excitation spectra of 0.1 and 2.5 mol% GSO were measured for both the Ce1 and Ce2 centers, with thin GSO samples (0.20 and 0.18 mm thick, respectively) at 11 K (Figs. 5a and 5b). One excitation spectrum has a monitored emission wavelength of 420 nm (near the Ce1 emission peak), and the other excitation spectrum has a monitored emission wavelength of 550 nm (near the Ce2 emission peak). The peaks at 203, 247, 254, 275, 308 and 313 nm in Fig. 5a correspond to the  $Gd^{3+}$  absorption lines, which indicates that energy is transferred from Gd to Ce1 and Ce2 centers either by process 1) or process 2). As stated above, the excitation peaks at 284 and 345 nm are due to direct absorption by the Ce1 center, and the peaks at 300 and 378 nm are due to direct absorption by the Ce2 center. The excitation spectra of 2.5 mol% GSO (Fig. 5b) do not show as many  $Gd^{3+}$  absorption lines as in Fig. 5a since the intensities of  $Gd^{3+}$  absorption are small compared with the intensities of  $Ce^{3+}$  absorption. Note that the peak

at 250 nm is observed for the first time and ascribed to the third-lowest 5d state of Ce1 center.

Fig. 6 displays the energy levels of Gd<sup>3+</sup> within the 4f<sup>7</sup> configuration [21–23] and the absorption bands of Ce1<sup>3+</sup> and Ce2<sup>3+</sup> for the transitions between the ground 4f states and the excited 5d states. The energy levels of Gd<sup>3+</sup> are based on the data shown in Fig. 4a and previous work [20]. The energy levels of Ce1<sup>3+</sup> and Ce2<sup>3+</sup> are based on the excitation spectra of GSO at 11 K (Figs. 5a and 5b). As can be seen, the three <sup>6</sup>P<sub>7/2</sub>, <sup>6</sup>P<sub>5/2</sub> and <sup>6</sup>P<sub>3/2</sub> excited states overlap absorption bands of the lowest excited state of Ce1<sup>3+</sup> and the second excited state of Ce2<sup>3+</sup>. The <sup>6</sup>I<sub>J</sub> multiplets of Gd<sup>3+</sup> mainly overlap the absorption band of the second excited state of Ce1<sup>3+</sup>.

### 3.2. Model

As observed in Fig. 6, the excited states of Gd<sup>3+</sup> overlap absorption bands of Ce1<sup>3+</sup> and Ce2<sup>3+</sup>. In addition, the excited states of Gd<sup>3+</sup> overlap each other. Thus, in the case of high donor concentration such as in GSO, donor–donor (Gd–Gd) and donor–acceptor (Gd–Ce) inter-

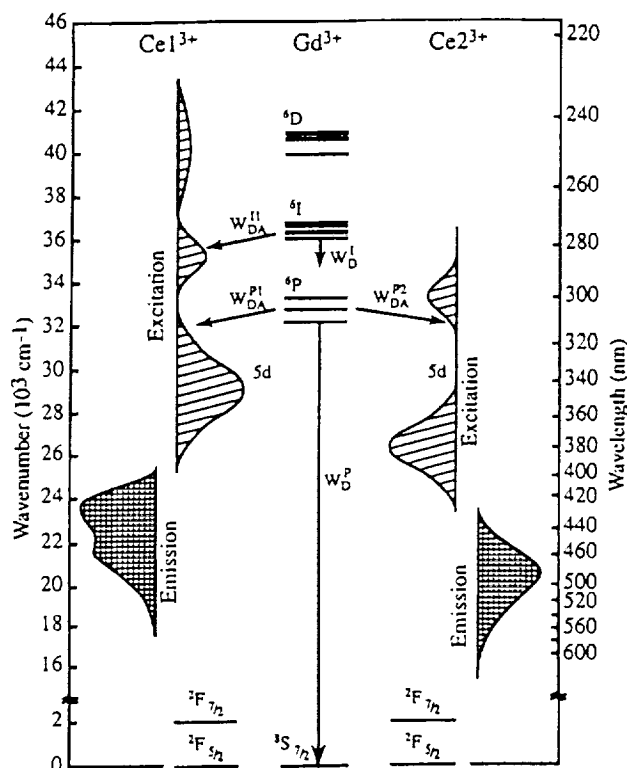


Fig. 6. Energy levels of Gd<sup>3+</sup>, Ce1<sup>3+</sup> and Ce2<sup>3+</sup> in GSO.

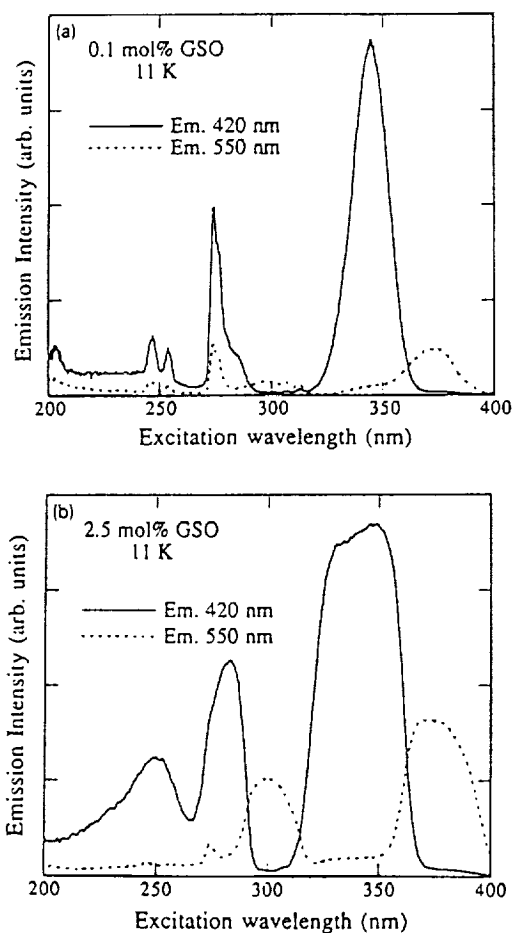


Fig. 5. (a) Excitation spectrum of 0.1 mol% GSO (0.2 mm thick sample) and (b) excitation spectra of 2.5 mol% GSO (0.18 mm) at 11 K. The excitation spectra were measured at the two emission wavelengths of 420 nm (solid line) and 550 nm (dashed line).

actions between two ions must be taken into account in describing the decay of the excited donor (Gd<sup>3+</sup>)\*. As one possible energy transfer mechanism between donor and acceptor, and between donors, let us consider resonant energy transfer. For example, between a donor and an acceptor the resonant energy transfer is given by [24]:

$$W_{da} = \frac{(2\pi)^2}{\hbar} |\langle D, A^* | H' | D^*, A \rangle|^2 \int g_D(E) g_A(E) dE = C_{da} f(R), \quad (1)$$

where an asterisk indicates the excited state of the ion,  $H'$  is the interaction Hamiltonian,  $g_D(E)$  and  $g_A(E)$  are the normalized lineshape functions for the transitions  $D^* \rightarrow D$  and  $A \rightarrow A^*$ .  $C_{da}$  is a microscopic parameter for the  $D-A$  interaction, and  $f(R)$  is the function whose form is determined by the nature of the  $D-A$  interaction. This energy transfer is non-radiative; it does not involve the emission of a photon by  $D$  and the subsequent absorption by  $A$ . Rather, it is a simultaneous deexcitation of  $D$  and excitation of  $A$ . The interactions which cause energy transfer are electrostatic coupling, magnetic coupling, and/or exchange coupling between ions. Similarly, the rate of resonant energy transfer between donors is expressed by

$$W_{dd} = C_{dd} f(R), \quad (2)$$

where  $C_{dd}$  is a microscopic parameter for the  $D-D$  interaction.

When one of the Gd<sup>3+</sup> ions (donors) is excited, the energy of this Gd<sup>3+</sup> ion can migrate through the Gd<sup>3+</sup>

Table 1  
The number of Gd<sup>3+</sup> neighbor sites and the corresponding Gd<sup>3+</sup>–Gd<sup>3+</sup> distances

Starting point	Distance (Å)	Site of neighbor	Number of neighbors
Gd1	3.360	Gd1	1
	3.671	Gd1	2
	3.724	Gd2	1
	3.791	Gd2	1
	4.176	Gd2	1
Gd2	3.520	Gd2	1
	3.573	Gd2	2
	3.724	Gd1	1
	3.791	Gd1	1
	3.803	Gd2	2
	4.128	Gd2	1
	4.176	Gd1	1

sublattice, since in GSO the Gd–Gd distance is very small (Table 1), and the acceptor concentration is low. We assume energy to migrate through the Gd<sup>3+</sup> sublattice before one of the excited Gd<sup>3+</sup> ions spontaneously (radiatively) emits a photon or resonantly transfers its energy to a nearby Ce<sup>3+</sup> or to a quenching center. This resonant energy transfer can accelerate the decay process of the excited Gd<sup>3+</sup> by the energy transfer to Gd<sup>3+</sup> centers with the shortest lifetime. The details of this energy migration through the Gd<sup>3+</sup> sublattice is discussed elsewhere [25].

### 3.2.1. Process 1) – radiative energy transfer

Process 1), that is, the radiative transfer from excited Gd<sup>3+</sup> to Ce<sup>3+</sup>, can occur since the emission lines (<sup>6</sup>P<sub>J</sub> and <sup>6</sup>I<sub>J</sub>) of the Gd<sup>3+</sup> (donor) overlap the absorption bands of the Ce<sup>3+</sup> (acceptor) (Fig. 4b). However, it will be shown that process 1) is not important on the time scale of interest. As observed for many Gd compounds [14–16,18,26] where Gd is either an activator or a lattice constituent, the decay constants of the strongly light-emitting states, <sup>6</sup>P<sub>7/2</sub> and <sup>6</sup>I<sub>7/2</sub>, are usually of the order of μs to ms. Thus, it is reasonable to assume that the Gd<sup>3+</sup> in GSO also has very slow radiative decay constants from these fluorescent states. If the radiative transfer from the Gd<sup>3+</sup> to the Ce<sup>3+</sup> occurs, that is, the Ce<sup>3+</sup> ion absorbs the photons emitted by the Gd<sup>3+</sup> without influencing the emission ability of Gd<sup>3+</sup>, then the observed decay curve of Ce<sup>3+</sup> in Fig. 2 must have very slow decay constants, of the same order as the Gd<sup>3+</sup> decay. However, the observed decay constants of Ce<sup>3+</sup> are much shorter. Thus, it is unlikely that process 1) contributes to the emission of GSO on the time scale observed from gamma-ray excitation (< 1 μs). Even on a long time scale, however, we expect that the radiative transfer from Gd<sup>3+</sup> to Ce<sup>3+</sup> does not play an important role, since the intensities of the Gd<sup>3+</sup> emission from undoped GSO with gamma-ray excitation

are very weak compared with the intensities of the Ce<sup>3+</sup> emission from doped GSO. Thus, process 1) can be ignored in considering the excitation process of Ce<sup>3+</sup>.

### 3.2.2. Process 2) – non-radiative (including resonant) energy transfer

As the energy of the excited Gd<sup>3+</sup> migrates through the Gd<sup>3+</sup> sublattice, the Gd<sup>3+</sup> system senses the average environment of acceptor ions. The average energy transfer from the donor to the acceptor is then expressed by a macroscopic (or an effective) transfer rate,  $W_{\text{eff}}$ , which is a function of four parameters ( $C_{\text{da}}$ ,  $C_{\text{dd}}$ ,  $N_{\text{A}}$  and  $N_{\text{D}}$ ).  $N_{\text{A}}$  and  $N_{\text{D}}$  are the ion densities of the acceptor and the donor, respectively;  $C_{\text{da}}$  and  $C_{\text{dd}}$  were defined earlier.  $W_{\text{eff}}$  depends linearly on  $N_{\text{A}}$  regardless of the nature of interactions between ions.

To analyze the non-radiative energy transfer process from Gd<sup>3+</sup> to Ce<sup>3+</sup>, the decay curves of 2.5 mol% GSO were measured by exciting the Gd<sup>3+</sup> absorption lines (Fig. 7). The decay curves observed with 275 and 313 nm excitation correspond to excitations of the excited <sup>6</sup>I<sub>J</sub> multiplets and the <sup>6</sup>P<sub>7/2</sub> states of Gd<sup>3+</sup>, respectively. The decay curve excited at 284 nm is a direct excitation of the Ce<sup>3+</sup> centers, and the decay curve excited at 300 nm mainly excites the Ce<sup>3+</sup> centers. The decay curve excited at 284 nm is the emission of the Ce<sup>3+</sup> and can be fit with a single exponential (22 ns). The decay curve excited at 300 nm contains the emission of both Ce<sup>3+</sup> and Ce<sup>2+</sup> and can be fit with an appropriate combination of two exponentials that have decay constants of 22 and 5 ns. On the other hand, the decay curve excited at 275 nm shows a build-up, and the decay excited at 313 nm contains a slow component. Since both wavelengths (275 and 313 nm) correspond to Gd<sup>3+</sup> absorption lines, it is reasonable to assume from these data that the energy is non-radiatively transferred from the Gd<sup>3+</sup> to the two Ce<sup>3+</sup> luminescent centers.

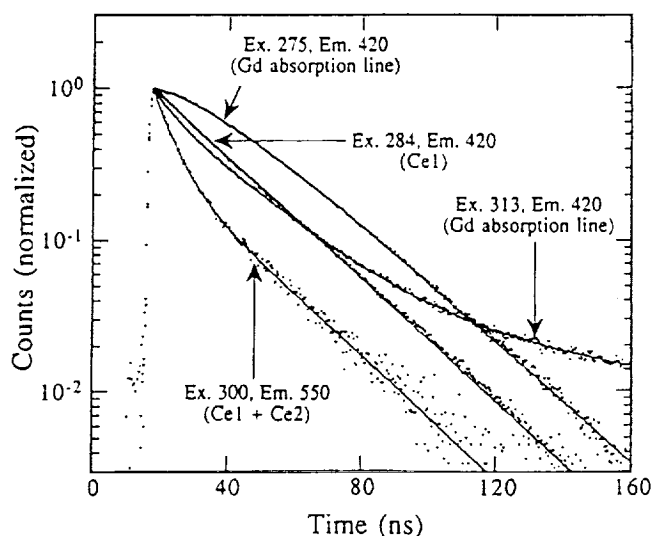


Fig. 7. The UV-excited decay curves of 2.5 mol% GSO.

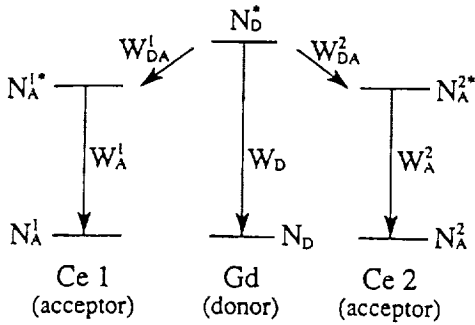


Fig. 8. Modes of decay and energy transfer in GSO.

The excited  $Ce^{3+}$  emits photons at much longer wavelengths than the absorption wavelengths (due to the large Stokes shift). Thus, back transfer from  $Ce^{3+}$  to  $Gd^{3+}$  is unlikely to occur in GSO. If we ignore the difference between the two types of  $Gd^{3+}$  ions, as discussed above, the transfer process from  $Gd^{3+}$  to  $Ce^{3+}$  and  $Ce^{2+}$  can be illustrated as in Fig. 8.  $N$  stands for the population of the ion. The effective transfer rate from the donor to the acceptor is written as  $W_{DA}^i$ , where the superscript  $i$  indicates the type of the  $Ce^{3+}$  (acceptor).  $W_D$ ,  $W_A^1$  and  $W_A^2$  represent the radiative decay rate of the excited  $Gd^{3+}$  state and the decay rate (including both radiative and non-radiative transitions) of the excited  $Ce^{3+}$  and  $Ce^{2+}$  states, respectively. Then the rate equation for each excited state can be given by:

$$\frac{dN_D^*}{dt} = -W_D N_D^* - W_{DA}^1 N_D^* - W_{DA}^2 N_D^*; \quad (3)$$

$$\frac{dN_A^{1*}}{dt} = W_{DA}^1 N_D^* - W_A^1 N_A^{1*}; \quad (4)$$

$$\frac{dN_A^{2*}}{dt} = W_{DA}^2 N_D^* - W_A^2 N_A^{2*}. \quad (5)$$

The solutions in the case where  $N_D^*(0)$  excited donors are created at  $t = 0$  and where no acceptors are excited, are:

$$N_D^*(t) = N_D^*(0) \exp[-(W_D + W_{DA}^1 + W_{DA}^2)t]; \quad (6)$$

$$N_A^{1*}(t) = N_D^*(0) \frac{W_{DA}^1}{W_A^1 - (W_D + W_{DA}^1 + W_{DA}^2)} \times \left\{ \exp[-(W_D + W_{DA}^1 + W_{DA}^2)t] - \exp[-W_A^1 t] \right\}; \quad (7)$$

$$N_A^{2*}(t) = N_D^*(0) \frac{W_{DA}^2}{W_A^2 - (W_D + W_{DA}^1 + W_{DA}^2)} \times \left\{ \exp[-(W_D + W_{DA}^1 + W_{DA}^2)t] - \exp[-W_A^2 t] \right\}. \quad (8)$$

In the case of GSO, for which the emission of the acceptor  $Ce^{3+}$  has been measured, Eq. (7) can be used to fit the decay curves.

### 3.3. Energy transfer from Gd to Ce

#### 3.3.1. Transfer from the ${}^6P_{7/2}$ states to $Ce^{3+}$

First, consider the energy transfer from the excited  ${}^6P_{7/2}$  state of Gd to  $Ce^{3+}$  and  $Ce^{2+}$ . The transition from the excited  ${}^6P_{7/2}$  state to the ground  ${}^8S_{7/2}$  state occurs only by radiative decay since the energy gap between these two states is too large to be compensated by multiphonon emission. The radiative decay rate ( $1/\tau_R$ ) of the excited  ${}^6P_{7/2}$  state has been measured for many Gd compounds [15,18,23,27,28] and has been reported to be of the order of  $\mu s$  to ms. Thus the decay of the excited  ${}^6P_{7/2}$  state can be expressed by the summation of the radiative decay and the effective transfer rate to the two  $Ce^{3+}$  ions. The excitation wavelength of 313 nm overlaps to the absorption band of the lowest excited 5d state of  $Ce^{3+}$ , the second lowest excited 5d state of  $Ce^{2+}$ , and the excited  ${}^6P_{7/2}$  state of Gd. Thus the decay curve,  $I(t)$ , excited at 313 nm (emission at 420 nm) can be fit with the following equation:

$$I(t) = N_A^{1*}(0) \exp\left(-\frac{t}{22}\right) + N_A^{2*}(0) \exp\left(-\frac{t}{5}\right) + N_D^*(0) \frac{W_{DA}^{P1}}{\frac{1}{22} - (W_D^P + W_{DA}^{P1} + W_{DA}^{P2})} \times \left\{ \exp[-(W_D^P + W_{DA}^{P1} + W_{DA}^{P2})t] - \exp\left[-\frac{t}{22}\right] \right\}, \quad (9)$$

where the first and the second terms represent the direct emission from  $Ce^{3+}$  and  $Ce^{2+}$  centers, respectively. The decay constants for the  $Ce^{3+}$  (22 ns) and  $Ce^{2+}$  (5 ns) emission are taken from the decay constant obtained from the decay curves excited at 284 and at 300 nm (Fig. 7). The third term is taken from Eq. (7) and represents the energy transfer from the  ${}^6P_{7/2}$  state of  $Gd^{3+}$  to  $Ce^{3+}$ . The  $Ce^{2+}$  emission produced by the transfer from the  ${}^6P_{7/2}$  state is ignored. As shown in Fig. 9, the decay excited at 313 nm is well fit with Eq. (9), which can be decomposed into three curves, each of which represents a term in Eq. (9). From the fit with this equation, a decay rate for the excited  ${}^6P_{7/2}$  state of  $Gd^{3+}$ ,  $W_D^P + W_{DA}^{P1} + W_{DA}^{P2}$ , of  $\sim (160 \text{ ns})^{-1}$  is obtained.

Two other excited states,  ${}^6P_{5/2}$  and  ${}^6P_{3/2}$ , were excited at 308 and 302 nm for 2.5% GSO. When exciting at 308 and 302 nm, not only the  ${}^6P_{5/2}$  and  ${}^6P_{3/2}$  states of  $Gd^{3+}$  but also the excitation bands of  $Ce^{3+}$  and  $Ce^{2+}$  are excited. The decay curves excited at 308 and 302 nm did not show long components and are composed of  $Ce^{3+}$  and  $Ce^{2+}$  decays. This is probably because the absorption intensities of  $Ce^{3+}$  and  $Ce^{2+}$  at 308 and 302 nm are much stronger than the absorption of these excited

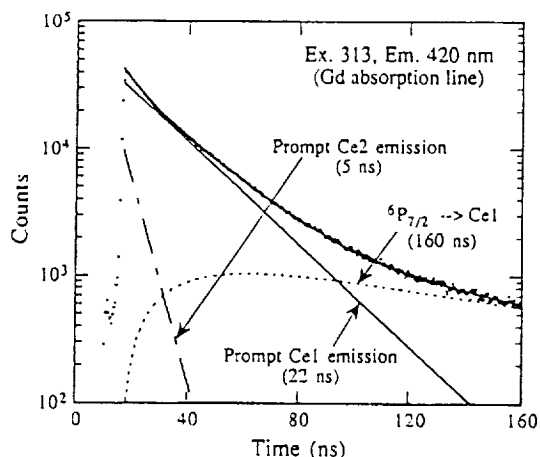


Fig. 9. The decay curve of 2.5 mol% GSO (closed circle). The excitation and emission wavelengths are 313 and 420 nm. The data were fit with Eq. (9) (solid line through the data points). The decay was decomposed into three curves, each of which represents a term in Eq. (9).

states of  $Gd^{3+}$ , and as a result it was difficult to observe the transfer effect due to these two excited states on our short time scale.

### 3.3.2. Transfer from the ${}^6I_J$ states to $Ce^{3+}$

Next consider the energy transfer from the excited  ${}^6I_J$  states of  $Gd^{3+}$  to  $Ce^{3+}$ . Because of our energy resolution ( $\sim 1.7$  nm), each state of the  ${}^6I_J$  multiplets, which usually have much smaller energy separation [20], could not be excited separately. Here we treat the  ${}^6I_J$  multiplets as a group. The  ${}^6I_J$  multiplets decay radiatively to the  ${}^8S_{7/2}$  ground state and non-radiatively to the  ${}^6P_J$  multiplets by phonon emission. The non-radiative decay rate from the  ${}^6I_J$  multiplets to the  ${}^6P_J$  multiplets is a little faster than the radiative decay rate from the  ${}^6I_J$  multiplets to the ground state, as has been shown for  $YOCl:Gd$  and  $LiYF_4:Gd$  [29]. However, the total decay rate of the  ${}^6I_J$  multiplets of  $Gd^{3+}$  is much longer than our time scale ( $< 1 \mu s$ ) for gamma-ray excitation. Based on the assumption that the decay rate of the  ${}^6I_J$  multiplets of  $Gd^{3+}$  is much longer than our times of interest, a similar equation to Eq. (9) can be used to fit the decay curve excited at 275 nm (emission at 420 nm):

$$I(t) = N_A^{I*}(0) \exp\left(-\frac{t}{22}\right) + N_D^{I*}(0) \frac{W_{DA}^{II}}{\frac{1}{22} - (W_D^I + W_{DA}^{II})} \times \left\{ \exp\left[-(W_D^I + W_{DA}^{II})t\right] - \exp\left[-\frac{t}{22}\right] \right\}; \quad (10)$$

where the first term represents the direct emission of

$Ce^{3+}$  since the wavelength of 275 nm corresponds to the absorption band of the second excited 5d state of  $Ce^{3+}$ . The second term represents the transfer from the  ${}^6I_J$  multiplets to  $Ce^{3+}$ . The transfer from the  ${}^6I_J$  multiplets to  $Ce^{2+}$  is ignored because the spectral overlap between the excited  ${}^6I_J$  multiplets and the absorption band of the second excited 5d state of  $Ce^{2+}$  is small.

Fig. 10 shows the decay curve excited at 275 nm together with the curve fit by using Eq. (10). Two decomposed curves, each of which represents the individual terms in Eq. (10), are also shown. The decay time of the excited  ${}^6I_J$  multiplets,  $(W_D^I + W_{DA}^{II})^{-1}$ , is obtained as 15 ns.

### 3.3.3. Concentration dependence of the transfer rate

The amount of the build-up observed for the gamma-ray excited decay curves shows a concentration dependence on Ce (Fig. 2). As the Ce concentration increases, the degree of the build-up decreases. Similarly, build-up is observed (for 2.5% GSO) with UV excitation (at 275 nm). The long component in the gamma-ray decay was also observed with UV excitation into the  ${}^6P_{7/2}$  states at 313 nm and this UV-excited, long decay component was found to be similar to the long decay component of the gamma-ray excited decay curve. This agreement suggests that the build-ups and slow components of gamma-ray excited decay curves could be associated with the energy transfer from  $Gd^{3+}$  to  $Ce^{3+}$ . Here we attempt to study the concentration-dependence of the transfer rate for the  ${}^6I_J$  states. The concentration-dependence of the  ${}^6P_J$  excited states could not be examined because of the short beam period ( $\sim 170$  ns) with the synchrotron source.

To study the concentration-dependence of the transfer rate, the decay curves excited at 275 nm were measured for various GSO samples. Fig. 11 shows the decay curves of five GSO samples (closed circle) excited at 275 nm. Also shown with each decay curve is a curve fit with Eq.

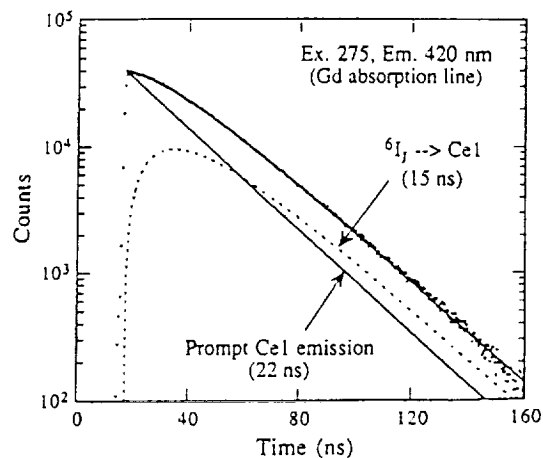


Fig. 10. The decay curve of 2.5 mol% GSO excited at 275 nm (closed circles). The data are fit with Eq. (10) (solid line) and decomposed into two curves, representing each term in Eq. (10).

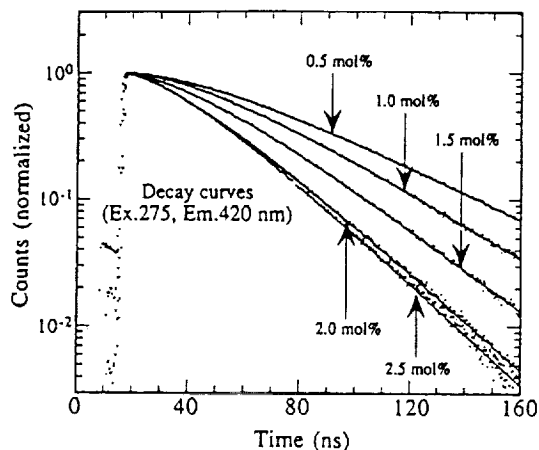


Fig. 11. The decay curve of five GSO samples excited at 275 nm. All curves have an emission wavelength of 420 nm.

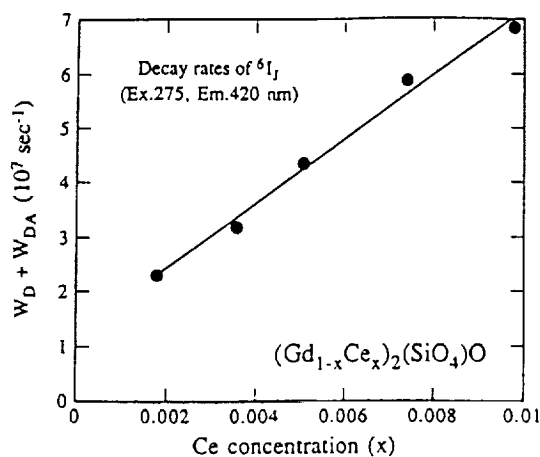


Fig. 12. Transfer rates from the  ${}^6I_J$  multiplets of  $Gd^{3+}$  to  $Ce^{3+}$ . The horizontal axis is the total Ce concentration.

(10). The decay constant of  $Ce^{3+}$  for each sample was obtained from the data in Fig. 3. The decay curves of these five GSO samples are well fit with Eq. (10). The transfer rates from the excited  ${}^6I_J$  multiplets to the  $Ce^{3+}$  were determined for each GSO sample (Table 2, column 3).

The decay rates of the excited  ${}^6I_J$  states, that is  $(W_D^I + W_{DA}^{II})$ , are displayed in Fig. 12 as a function of Ce concentration. Although the concentration of trivalent Ce concentration was not measured, we assume that  $Ce^{3+}$  concentration is proportional to the total Ce concentration obtained from chemical analysis. As expected, the decay rate,  $(W_D^I + W_{DA}^{II})$ , depends linearly on the total Ce concentration. The straight line intercepts the vertical axis at about  $1 \times 10^7 \text{ s}^{-1}$ . This implies that  $W_D^I$ , which is independent of Ce concentration, is about  $1 \times 10^7 \text{ s}^{-1}$ . However, in many other Gd compounds,  $W_D^I$  is much slower than  $1 \times 10^7 \text{ s}^{-1}$  [14,18,23,29]. Thus, the fast rate of  $W_D^I$  might be due to the energy transfer from the  ${}^6I_J$  states to quenching centers such as Gd traps or other impurities, whose contribution was not taken into account in deriving Eq. (10). The possibility of energy transfer to the Gd traps is discussed elsewhere [25].

### 3.3.4. Transfer from the ${}^6D_J$ state to $Ce^{3+}$

A sample of 2.5 mol% GSO was excited at 254 and 247 nm into the excited  ${}^6D_J$  states. The two wavelengths correspond to the excitation of the  ${}^6D_J$  multiplets and the absorption band of  $Ce^{3+}$  located at 250 nm. Since the  $Ce^{3+}$  absorption intensity at 250 nm is much stronger than the Gd absorption intensities at 247 and 254 nm, the decay curves excited at 254 and 247 nm were the same as the decay curve excited at 284 nm and no effect due to the transfer from Gd to Ce1 was observed on our short time scale.

## 4. Discussion

In the last section, data on the decay of  $Ce^{3+}$  from the excitation of the  ${}^6P_J$ ,  ${}^6I_J$  and  ${}^6D_J$  states of the  $Gd^{3+}$  ion were analyzed. A build-up and a long component were observed in the  $Ce^{3+}$  decays when  ${}^6I_J$  and  ${}^6P_J$  states of  $Gd^{3+}$  were excited. This observation suggests that the build-up and the long component seen in the gamma-ray excited decays may be associated with the energy transfer from  ${}^6I_J$  and  ${}^6P_J$  states of  $Gd^{3+}$  to  $Ce^{3+}$ .

Table 2

Decay times for different GSO samples. Decay times of the  ${}^6I_J$  states of the  $Gd^{3+}$  (column 3) were calculated from the UV-excited decays fitting Eq. (10). Decay times of the  ${}^6I_J$  (column 4) and  ${}^6P_J$  (column 5) states were also obtained from the gamma-ray excited decays using Eq. (11). All the decay times are given by their reciprocals (in ns)

Sample	Nominal Ce conc (mol%)	$(W_D^I + W_{DA}^{II})^{-1}$ (UV) (ns)	$(W_D^I + W_{DA}^{II})^{-1}$ (gamma) (ns)	$(W_D^P + W_{DA}^{P1} + W_{DA}^{P2})^{-1}$ (gamma) (ns)
	0.1	—	194	736
	0.5	43	52	397
	1.0	31	29	340
	1.5	23	23	308
	2.0	17	18	232
	2.5	15	16	220

To test this speculation, we attempted to explain the gamma-ray excited decays. We assume that  $Ce^{3+}$  is excited either by the energy transfer from  $Gd^{3+}$  (delayed emission, process 2) or excited promptly ( $< 1$  ns) [30] by any of several mechanisms including exciton capture (process 4) or a prompt electron–hole recombination process (process 5)). We also assume that the excited state,  $(Gd^{3+})^*$ , of  ${}^6I_J$  and  ${}^6P_J$  states are promptly created and then energy is transferred mostly to the  $Ce^{3+}$ . The energy transfer from the higher excited states of  $Gd^{3+}$  to  $Ce^{3+}$  is ignored since the spectral overlaps between those states and  $Ce^{3+}$  are relatively small. The time required for the  $(Gd^{3+})^*$  and  $(Ce^{3+})^*$  to be created is very short ( $1 < ns$ ) on our time scale, and it is assumed that  $(Gd^{3+})^*$  and  $(Ce^{3+})^*$  are formed at  $t = 0$ . The non-radiative energy transfer from vacancies or traps to the  $Ce^{3+}$  (process 3)) is ignored.

Using these assumptions, the  $Ce^{3+}$  decays of various GSO samples excited by gamma rays were fit with the following equation:

$$\begin{aligned}
 I(t) = & N_A^{1*}(0) \exp\left(-\frac{t}{\tau_1}\right) \\
 & + N_D^{1*}(0) \frac{W_{DA}^{11}}{\frac{1}{\tau_1} - (W_D^1 + W_{DA}^{11})} \\
 & \times \left\{ \exp\left[-(W_D^1 + W_{DA}^{11})t\right] - \exp\left[-\frac{t}{\tau_1}\right] \right\} \\
 & + N_D^{P*}(0) \frac{W_{DA}^{P1}}{\frac{1}{\tau} - (W_D^P + W_{DA}^{P1} + W_{DA}^{P2})} \\
 & \times \left\{ \exp\left[-(W_D^P + W_{DA}^{P1} + W_{DA}^{P2})t\right] \right. \\
 & \left. - \exp\left[-\frac{t}{\tau_1}\right] \right\}, \quad (11)
 \end{aligned}$$

where  $\tau_1$  represents the decay constant of  $Ce^{3+}$  and is taken from the data of Fig. 3. The first term of Eq. (11) represents the prompt emission from  $Ce^{3+}$  created by processes 4) and 5), the second term represents the  $Ce^{3+}$  emission populated through the  ${}^6I_J$  multiplets of  $Gd^{3+}$  and the third term represents the  $Ce^{3+}$  emission populated through the  ${}^6P_J$  multiplets.  $N_A^{1*}(0)$ ,  $N_D^{1*}(0)$  and  $N_D^{P*}(0)$  are the populations of excited  $Ce^{3+}$ , of the excited  ${}^6I_J$  multiplets and of the excited  ${}^6P_J$  multiplets, at  $t = 0$ . The curve from fitting the data for 2.5 mol% GSO is shown by the solid line through the data in Fig. 13. The decay curve is also decomposed into the three separate terms of Eq. (11) in Fig. 13. As seen in Fig. 13, the gamma-ray excited decay curve is reasonably well fit. Without the first term of Eq. (11), the decay curve could not be well fit. The best fit parameters are given in Table

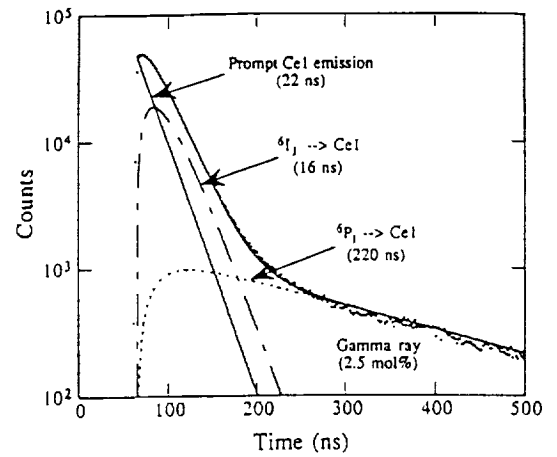


Fig. 13. The gamma-ray excited decay curve of 2.5 mol% GSO (closed circles). The data are fit with Eq. (11) (solid line through the data) and decomposed into three curves, representing each term in Eq. (11).

2. Columns 4 and 5 in table 2 show the decay rates of the  ${}^6I_J$  multiplets and of the  ${}^6P_J$  multiplets calculated from the decay curves excited by gamma radiation, respectively. The values in column 3 agree well with those in column 4, suggesting that the initial build-ups of the gamma-ray excited decay curves are due to the non-radiative transfer from the  ${}^6I_J$  multiplets of  $Gd^{3+}$  to  $Ce^{3+}$ .

The  $N_A^{1*}(0)$  and  $N_D^{1*}(0)$  can be calculated from the fitting curves. The  $N_A^{1*}(0)$  is the coefficient of the first term of Eq. (11), and the  $N_D^{1*}(0)$  is calculated from the coefficient of the second term of Eq. (11). An interesting comparison is made by taking the ratio of the  $N_A^{1*}(0)$  to the  $N_D^{1*}(0)$ . These ratios are displayed against Ce concentration in Fig. 14. The  $N_D^{1*}(0)$  denotes the population of the excited  ${}^6I_J$  multiplets which transfer energy to the  $Ce^{3+}$  and is used as a denominator in calculating the ratios, assuming that the excitation probability of the  ${}^6I_J$  multiplets of the  $Gd^{3+}$  is essentially constant from sample to sample. This assumption is reasonable since the Gd

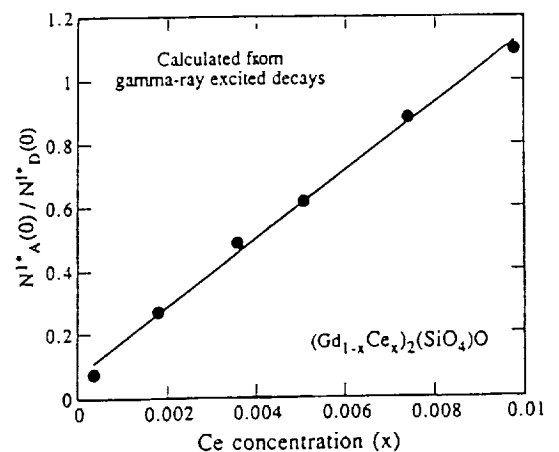


Fig. 14. The ratio of CeI population to Gd population ( ${}^6I_J$  state) at time  $t = 0$  as a function of total Ce concentration.

concentration is almost the same for each of the measured GSO samples. As can be seen in Fig. 14, the ratio of  $N_A^{1*}(0)$  to  $N_D^{1*}(0)$  depends linearly on the total Ce concentration. This linear dependence shows that the probability of prompt exciton capture or prompt electron–hole recombination at  $Ce1^{3+}$  is constant. It also shows that the rates of prompt exciton capture or prompt electron–hole recombination at  $Ce1^{3+}$  increase linearly with the increase in the Ce concentration in GSO.

The gamma-ray excited decay curve of each center was measured at 15 K (Fig. 15). The decay of  $Ce1^{3+}$  contains both the build-up and the long decay component, similar to the data taken at room temperature. The decay of  $Ce2^{3+}$ , however, does not show the build-up. The  $Ce2$  decay seems to contain a fast decay component, probably due to the prompt emission, and the long decay component, which is similar to the long decay component of  $Ce1$  decay. Thus, these results support our assumption that the  ${}^6I_J$  states do not feed the  $Ce2$  center.

In analyzing these gamma-ray excited decay curves, the effect of the non-radiative transfer from the vacancies or traps to  $Ce1^{3+}$  (process 3)) were ignored. Nonetheless, the gamma-ray excited decay curves have been successfully reproduced. These results suggest that the non-radiative energy transfer from  $Gd^{3+}$  to  $Ce1^{3+}$  and the prompt  $(Ce^{3+})^*$  creation by any of several mechanisms are the main processes in exciting  $Ce1^{3+}$  at room temperature where most gamma-ray excited decay data were taken. The origins of the two decay constants previously observed with gamma-ray excitation [2] can be attributed to the non-radiative transfer from  $Gd^{3+}$  to  $Ce1^{3+}$ . Among the five probable processes for exciting the  $Ce^{3+}$  (discussed in section 3.1), processes 2), 4) and 5) seem important. The overall scintillation mechanism for GSO can be summarized in Fig. 16. The role of Gd is to capture energy from ionizing radiation and to transfer it to  $Ce^{3+}$  ions. However, the energy transfer from  $Gd^{3+}$  to  $Ce^{3+}$  causes slow

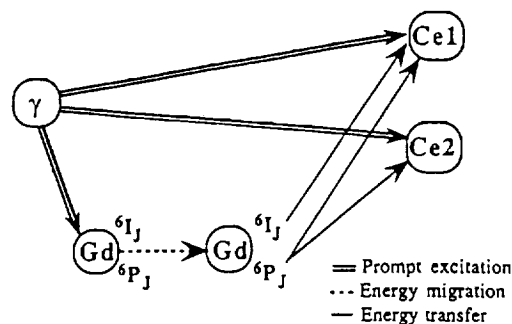


Fig. 16. Scintillation processes in GSO.

scintillation decays, which is not desirable for applications involving fast timing. The details of the prompt creation process of the excited states,  $(Gd^{3+})^*$  and  $(Ce^{3+})^*$ , have yet to be investigated.

## 5. Summary

We have shown that the gamma-ray excited decay curves of GSO have initial build-ups as well as long decay components. We also have shown that the amount of build-up in the gamma-ray excited decay curve decreases as the Ce concentration increases.

As a possible explanation for the build-ups and the long decay components of gamma-ray excited decay curves, the non-radiative transfer from  $Gd^{3+}$  to  $Ce^{3+}$  was investigated using a UV light source. The UV-excited decay curves of GSO showed that the energy transfer from the excited  ${}^6I_J$  multiplets of  $Gd^{3+}$  to  $Ce^{3+}$  produces the initial build-ups and that the energy transfer from the excited  ${}^6P_J$  multiplets of  $Gd^{3+}$  to  $Ce^{3+}$  creates the long decay components. This observation for the UV-excited decay curves leads to the speculation that the initial build-ups of gamma-ray excited decay curves from GSO are also due to the energy transfer from  $Gd^{3+}$  to  $Ce^{3+}$ .

We successfully fit the gamma-ray excited decay curves using three terms, which represent the  $Ce1^{3+}$  prompt emission, the energy transfer from the excited  ${}^6I_J$  multiplets to  $Ce1^{3+}$  and the energy transfer from the excited  ${}^6P_J$  multiplets to  $Ce1^{3+}$ . The decay rates of the  ${}^6I_J$  multiplets obtained from the gamma-ray excited decay curves agree with those obtained from the decay curve excited at 275 nm for various GSO samples, supporting our assumption.

The population of initially excited  $Ce1^{3+}$ ,  $N_A^{1*}(0)$ , was compared with the population of initially excited  ${}^6I_J$  multiplets of  $Gd^{3+}$ ,  $N_D^{1*}(0)$ . This comparison showed that the ratio,  $N_A^{1*}(0)/N_D^{1*}(0)$ , linearly increases as the total Ce concentration increases.

The origin of the two decay constants observed with gamma-ray excitation in GSO can be ascribed to non-radiative energy transfer from  $Gd^{3+}$  to  $Ce^{3+}$ .

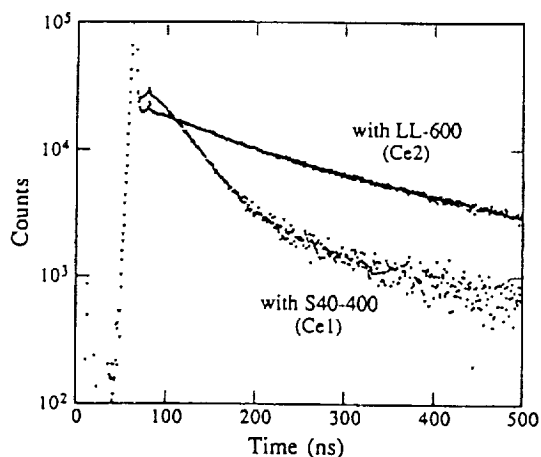


Fig. 15. The gamma-ray excited decay curves of  $Ce1$  and  $Ce2$  emissions at 15 K (from 2.5 mol% GSO).

## Acknowledgements

We are grateful to Drs. John Sutherland, John Trunk and Krzysztof Polewski in the Biology Department, Brookhaven National Laboratory for their help in obtaining the decay data. We would like to thank Drs. John J. Simonetti and Stefan Vajda at EMR Photoelectric for their valuable comments and Dr. Hiroyuki Ishibashi and Takeshi Utsu at Hitachi Chemical Co., Ltd. for providing GSO samples. We also would like to thank Dr. Oliver Mullins, Dr. Yifu Zhu and Ralph Manente for useful discussions.

## References

- [1] K. Takagi and T. Fukazawa, *Appl. Phys. Lett.* 42 (1983) 43.
- [2] C.L. Melcher, J.S. Schweitzer, T. Utsu and S. Akiyama, *IEEE Trans. Nucl. Sci.* NS-37 (2) (1990) 161.
- [3] J.B. Birks, *The Theory and Practice of Scintillation Counting* (Pergamon, 1964) chap. 4.
- [4] H. Suzuki, T.A. Tombrello, C.L. Melcher and J.S. Schweitzer, *Nucl. Instr. and Meth. A* 320 (1992) 263.
- [5] J. Felsche, in: *Structure and Bonding V13*, eds. Dunitz et al. (Springer, 1973) p. 99.
- [6] V.G. Baryshevskii et al., *Vesti Akad. Navuk BSSR, Ser. Fiz. Energet. Navuk* 4 (1991) 114 (or *The Proceedings of the BSSR Academy of Science, Power Engineering Physical Series* 4 (1991) 114).
- [7] C.L. Melcher, R.A. Manente, C.A. Peterson and J.S. Schweitzer, *J. Cryst. Growth* 128 (1993) 1001.
- [8] L.M. Bollinger and G.E. Thomas, *Rev. Sci. Instr.* 32 (1961) 1044.
- [9] M. Moszynski, C. Gresset, J. Vacher and R. Odru, *Nucl. Instr. and Meth.* 188 (1981) 403.
- [10] H. Suzuki, T.A. Tombrello, C.L. Melcher and J.S. Schweitzer, *IEEE Trans. Nucl. Sci.* 40 (4) (1993) 380.
- [11] C.L. Melcher and J.S. Schweitzer, *Nucl. Instr. and Meth. A* 314 (1992) 212; US Patents No. 4958080 and 5025151 (to Schlumberger).
- [12] V.A. Voloshin et al., Preprint ISC-91-8, Kharkov: Institute for Single Crystals-1991.
- [13] S. Hufner, *Optical Spectra of Transparent Rare Earth Compounds* (Academic Press, 1978).
- [14] P.J. Alonso, V.M. Orera, R. Cases and R. Alcala, *J. Lumin.* 39 (1988) 275.
- [15] C.T. Garapon, B. Jacquier, J.P. Chaminade and C. Fouassier, *J. Lumin.* 34 (1985) 211.
- [16] A.J. de Vries, M.F. Hazenkamp and G. Blasse, *J. Lumin.* 42 (1988) 275.
- [17] H.S. Kiliaan, A. Meijerink and G. Blasse, *J. Lumin.* 35 (1986) 155.
- [18] A.J. de Vries and G. Blasse, *J. Chem. Phys.* 88 (1988) 7312.
- [19] L.H. Brixner and G. Blasse, *Europ. J. Solid State Inorg. Chem.* 27 (1990) 581.
- [20] H.M. Crosswhite and R.L. Schwiesow, *J. Chem. Phys.* 50 (1969) 5032.
- [21] B. Di Bartolo, *Optical Interactions in Solids* (Wiley, 1968) p. 470.
- [22] H.M. Crosswhite and H.W. Moos (eds.), *Optical Properties of Ions in Crystals* (Interscience, 1967) p. vi.
- [23] P.P. Yaney, D.M. Schaeffer and J.L. Wolf, *Phys. Rev.* B11 (1975) 2460.
- [24] B. Henderson and G.F. Imbusch, *Optical Spectroscopy of Inorganic Solids* (Oxford University, 1989) chap. 10.
- [25] H. Suzuki, T.A. Tombrello, C.L. Melcher and J.S. Schweitzer, *IEEE Trans. Nucl. Sci.* (1994) in press.
- [26] D.W. Hall and M.J. Weber, *Phys. Rev.* B27 (1983) 1903.
- [27] J. Chrysochoos, B. Kumar and S.P. Sinha, *J. Less-Common Met.* 126 (1986) 195.
- [28] A.J. de Vries and G. Blasse, *J. Phys. Coll. C7* (1985) 109.
- [29] J. Sytsma, G.F. Imbusch and G. Blasse, *J. Phys. Condens. Matter* 2 (1990) 5171.
- [30] R.B. Murray, *IEEE Trans. Nucl. Sci.* NS-22 (1975) 54.

## **Appendix 3**

**Application of Continuum Analysis to Borehole Gamma-Ray  
Spectra Obtained from the German Continental Depp Drilling  
Project**

APPLICATION OF CONTINUUM ANALYSIS TO BOREHOLE GAMMA-RAY SPECTRA OBTAINED  
FROM THE GERMAN CONTINENTAL DEEP DRILLING PROJECT

ALAKH N THAKUR, JAMES R ARNOLD, AND JEFFREY S SCHWEITZER<sup>1</sup>

California Space Institute and Department of Chemistry  
University of California, San Diego, La Jolla, CA 92093-0524, USA.

<sup>1</sup> Schlumberger-Doll Research, Old Quarry Rd., Ridgefield, CT 06877-4108, USA.

ABSTRACT

Neutron induced gamma-ray spectra from borehole rock at several depths were analyzed as test samples to evaluate the usefulness of continuum spectra in deriving chemical composition information from gamma-ray spectra of thick target sources. A fast Fourier transform technique has been used to estimate the signal content of selected energy bands of the continuum spectra. Monte Carlo calculations of the modeled borehole data have been performed using the major gamma-ray energy sources to generate the corresponding detected gamma-ray spectra. Borehole spectra are compared to the simulated spectra to check the consistency of the signal distribution between the peak and the continuum. For a chosen gamma-ray line, we calculate the continuum above and below that line to find what fraction of the lower energy continuum is due to that line. The accuracy of the relative elemental concentrations determined by this method is confirmed through comparison with laboratory XRF elemental analysis of cuttings and core samples from the well. A number of tests show that using the continuum could greatly increase the sensitivity and precision of the measurement of elemental concentrations determined from gamma-ray spectra of thick target sources, for spectra having peaks of poor statistical significance. However, for thin target sources or spectra with very good statistics in their peaks, this method may not be very advantageous. This example illustrates the value of this procedure, proposed by Thakur and Arnold (1993).

## INTRODUCTION

Gamma-ray spectroscopy is a widely used technique to measure nuclide and chemical compositions of a variety of condensed materials. Major applications include radiological protection, environmental and fallout studies, biological and biomedical investigations, geological dating, environmental risk studies, atmospheric transport surveys, planetary mapping, neutron activation and nuclear reaction studies.

In parallel with the development of high-purity germanium detectors of increased efficiency and improved resolution, new techniques have been developed for applications of gamma-ray spectrometry which involve the measurement of very weak or unstable sources. Were it not for the continuum, the analysis of most peaks in a gamma-ray spectrum would be a very simple and straight forward matter of summing counts. Even very tiny peaks could then be easily analyzed. However as Op de Beek (1979) has indicated in the framework of information theory, the germanium detector is a very poor transducer and most of the mono-energetic photons that interact with the detector are registered at channels in the spectrum other than those corresponding to the full energy peak. This creation of a continuum component (traditionally known as a background component) at energies lower than the peak energy is further complicated by several other processes; for example secondary photon interactions or photons arising from interactions with the material surrounding the detector, an especially important effect in measurements on extended samples. The important point here is that all these effects can be assigned to the mono-energetic gamma-rays arising from a particular chemical source. The only contributor to the continuum not due to a chemical origin is bremsstrahlung. However this phenomenon is not significant in the energy range of 1-10 MeV considered here.

This approach to understanding gamma-ray spectra by using the continuum has been reported in several previous studies. The orbital gamma-ray spectra obtained during Apollo 15 and 16 have been examined for the possibility of obtaining concentrations of iron, titanium, aluminum, oxygen and silicon by matrix inversion of various energy bands (Davis and Arnold, 1979). The study concluded that given the resolution of Apollo gamma-ray data, oxygen and silicon concentrations do not vary

enough on the lunar surface to change appreciably the count rate of any energy band. A similar conclusion was reached using library function analysis (Bielefeld et al., 1976). Davis (1980) obtained results in good agreement with regional ground truth concentrations by a linear regression analysis. Metzger and Parker (1979) have also used fixed energy bands, of width 0.42 MeV for titanium and 1.63 MeV for iron, to get continuum information.

In this paper we investigate the continuum by taking as examples neutron activation gamma-ray spectra (both prompt and delayed) of crystalline rock obtained in a borehole with a germanium spectrometer. The composition of borehole formation rock can be estimated by the spectroscopy of neutron-induced gamma rays as is done in laboratory neutron activation analysis. The technique relies on the prompt emission of one or more characteristic gamma rays that accompanies the capture of thermal neutrons by most of the formation nuclei. Spectroscopic detection of these gamma rays allows the identification of the nuclei and a quantification of their abundances. Some important distinctions can be made between activation analysis done in a borehole and in the laboratory. In the laboratory, a stable and intense source of neutrons irradiates a small sample and elemental standards that are surrounded by an efficient detection system. In the borehole, or in other non-laboratory applications, such as planetary measurements a relatively weak and sometimes variable source is used to irradiate a semi-infinite sample whose properties alter the activation flux. The resulting gamma rays are measured by a gamma-ray detector, which is, by necessity, geometrically inefficient. Despite these obstacles, accurate elemental concentrations are required.

A great deal of research has been performed (Schweitzer, 1991) to better quantify the precision and accuracy of elemental concentration measurements and to add significantly to the current list of elements that can be measured in the borehole. Use of efficient, optimized detectors is one such strategy (Schweitzer et al., 1993; Mills et al., 1991). In this report we examine the ways to improve the accuracy and sensitivity of such statistics-limited data by using continuum information. Because our approach is not traditional, we must use some terms in an unfamiliar way. Here much of the continuum, and nearly all its variations over the formation surface, is "signal" rather than noise or

background. We use "background" to mean counts due to non-nuclear events (meson interactions, bremsstrahlung) and those not originating in the formation target.

## METHOD

### How and where the spectra were obtained

The borehole data were obtained from the pilot hole of the German Continental Deep Drilling Project (KTB) (Draxler, 1992) in Windischeschenbach, Germany. The data used here were obtained to evaluate the enhancement to elemental concentrations that could be determined in situ compared with what could be obtained with scintillation detectors (Grau et al. 1993, Schweitzer et al. 1994). The diameter of the borehole is 15 cm. It is filled with water. The detector is a high purity germanium (HpGe) crystal of approximately 5 cm diameter and 5 cm length and is shielded from neutrons by tungsten and boron carbide. This detector has a characteristic efficiency of ~ 16 % for the cobalt line at 1.3325 MeV.

Two types of neutron spectra were obtained. Prompt gamma-ray spectra from thermal neutron capture reactions were obtained with a pulsed D,T generator. The spectra were only accumulated after each pulse of neutrons was completed, eliminating gamma-rays from inelastic scattering and high-energy (n,x) reactions. These are referred to here as "C" spectra. Each "C" spectrum was accumulated for 20 minutes, consisting of 60 20-second individual spectra. Over most of the energy range to 8 MeV, resolution was approximately 12 keV. Spectra of delayed gamma-rays produced in the decay of residual radioactivity were obtained through the use of a  $^{252}\text{Cf}$  source ( $\sim 10^8$  n/s) located 5.02 m from the Ge detector. These are referred to here as "A" spectra. The "A" spectra resulted from a 10 minute irradiation, a 20 - 30 s delay until the detector was positioned opposite the irradiated region and a 10 minute detection time, again broken into individual 20 second accumulations to allow half life analysis of individual peaks. These spectra had an energy resolution of ~ 3 keV.

Even though the D,T generator produces essentially mono-energetic 14 MeV neutrons, the process of neutron slowing down to thermal energies, primarily through interactions with hydrogen and

other light nuclei, creates a spatially varying thermal neutron flux at different depths in the borehole. A procedure for dealing with this variation has been described previously (Grau and Schweitzer, 1989) but must be accounted for when analyzing data obtained at different locations, since slowing down properties are sensitive to variations in porosity and mineralogy, and thermal neutron capture probability is affected by changes in the macroscopic thermal neutron absorption cross section (either in the borehole or the rock). In addition, the neutron flux is altered by changes in the geometry of the borehole.

#### The delayed activation and capture spectra

An "A" spectrum obtained in this borehole, showing the delayed activity produced from thermal neutron capture reactions, is given in Figure 1. In this figure, spectral contributions from V, Mn, Ca and Na are evident, though their intensities are about two orders of magnitude lower than the aluminum peak at 1.778 MeV. Most of the analysis reported in this work is based on neutron capture "C" gamma-ray spectra. Focussing only on those elements associated with the rock matrix allows a measurement of the concentrations of Si, Ca, Ti, Fe, and Gd (Ellis, 1990). A neutron capture "C" spectrum, integrated for twenty minutes, is plotted in Figure 2. Several lines are identified. The hydrogen capture line at 2.2233 MeV is most prominent; the silicon capture line at 4.934 MeV and the doublet from iron capture near 7.646 MeV can also be observed. The  $^{40}\text{Ca}$  line at 6.42 MeV is almost invisible.

In our analysis we use only spectral intensities (peak, continuum) when the properties are from an individual spectrum and the factors needed to relate peak intensity to elemental concentration are the same, and thus cancel out in any comparison. However, when comparing a property of one spectrum with either another type of measurement (C with A) or with a laboratory measurement of concentration, we have "normalized" the spectral result by the necessary geophysical parameter values.

### Analysis of the gamma-ray peaks

The peak intensities are first estimated using the Ganymed program (Yadav et al., 1989; Kruse, 1979), an interactive graphics computer program for peak analysis. The peak intensities obtained here are in good agreement with those obtained previously (Schweitzer et al., 1993). Ganymed has been in use at the Max Planck Institut für Chemie, Mainz for many years, mainly for neutron activation analysis, and it has been improved to handle a number of special applications such as spectra from radiation damaged detectors, multiple peaks, and other peculiar peaks (Boynton et al., 1992). In order to fit the peaks in a spectrum, two fitting parameters, sigma and rho, can either be preset or are subject to an automatic fitting procedure. Sigma gives the width of the Gaussian portion and rho gives the point where an exponential tailing, on the low energy side, is smoothly connected to the Gaussian curve. If there is no tailing then rho is infinitely large. Rho and sigma are described by a linear relationship: an intercept and slope as a function of energy. The energy dependence of the full width at half maximum (FWHM) is a property of a particular detector. Figure 3 is the peak area determined by the Ganymed code at two energies, 7.646 MeV and 5.515 MeV, due to Fe ( $n,\gamma$ ) and Ca ( $n,\gamma$ ) reactions, respectively. We choose these two lines in the high energy region because they are the strongest high energy lines for each element, and there are no significant interferences observed from other lines. Variations with depth are caused by small timing and flux variations as well as compositional changes.

### The Fourier transform approach

A detailed description of the procedure has been given previously (Thakur and Arnold, 1993). First, a quantitative estimate of all the peak intensities were obtained with the Ganymed program. Elements were then identified by using a nuclear database library. These lines were subtracted from the gamma-ray spectra in the energy domain. This is straightforward and does not seem to pose any difficulty. If the lines were not removed in the energy domain, they would produce a high frequency signal in the frequency domain. Although it may not be necessary for the continuum analysis, when

significant, the peaks are recorded and removed before proceeding.

#### Monte Carlo Simulation of borehole data

Monte Carlo simulation has become a standard method for accurately predicting the response of nuclear well logging tools (e.g. Soran, 1988; Ullo, 1986; Pinault, 1991; Ghanem et al., 1993; Couët and Hertzog, 1992). A variety of general and specific purpose Monte Carlo codes are routinely used by nuclear tool designers and those interested in the study of subsurface formations with nuclear logs. Following those examples we performed a Monte Carlo simulation of a borehole of appropriate geometry to the KTB pilot hole. Natural alumino-silicate composition with 0.5 % water was assumed. We have used two different codes, MCNP (Briesmeister, 1986; Hendricks and Briesmeister, 1992) and ITS (Halbleib et al., 1992a; Halbleib et al., 1992b). Both codes were run on a Sun Sparc 10 workstation and on an Intel-486 based PC. The Monte Carlo model treats all components of the photon, electron and positron cascade initiated by the incident gamma rays. Photons, positrons and electrons were tracked until they either escaped from the detector or reached below a cut off kinetic energy of 1 keV, at which point the particles were considered to be stopped. Compton scattering, photoelectric absorption and pair production are taken into account in tracing the histories of the primary and secondary gamma-ray photons.

No variance reduction was attempted in the simulations since the reduction of computer time was not a critical issue in obtaining sufficient precision in the Monte Carlo calculation. A comparison between the calculated gross spectrum and a borehole spectrum shows good agreement. Figure 4 compares the continuum spectrum calculated with the Monte Carlo model with the experimental data. The simulation is seen to be imperfect but adequate for method development. Some discrepancies are due to poor discrimination between direct neutron interactions and gamma rays in the vicinity of intense peaks; small errors in detector resolution or in peak shapes (in the model, peaks are represented by Gaussian shapes) may induce large errors between the experimental and calculated spectra.

Comparison between continuum and peak ratio responses in the calculated and experimental spectra

Borehole spectra are compared to the simulated spectra to check the consistency of the signal distribution between the peak and the continuum (Thakur and Arnold, 1993). The major gamma-ray energy line sources used to calculate the corresponding continuum spectra are given in Table 1. For the continuum an energy band for each corresponding line was extracted from beneath the peak down until just above the next lowest energy gamma-ray line. The true continuum in a stated region is evaluated by subtracting the linearly extrapolated value of the continuum from energies above the line. A true peak area includes first and second escape peaks, except at lower energies where first and second escape peaks become insignificant.

## RESULTS AND DISCUSSION

Both delayed as well as capture spectra continuum are found to obey the Poisson statistical distribution. All analyses are done both in energy and frequency space for consistency and reliability. The analysis of 87 capture spectra in energy space at different depths produces a correlation (R squared) of 0.881 for the 7.646 MeV peak (Figure 5a) and 0.865 for the 5.515 MeV peak (Figure 5b). This correlation of continuum to peak area slowly becomes worse at lower energies due to interfering peaks. Continuum to peak ratio at eight energies is listed in Table 1. The scatter in the individual ratio can be visualized by the standard deviation listed in the fifth column. However, most of the errors can be assigned to errors associated with determining peak areas and not to the continuum. The 0.511 MeV photon annihilation peak has higher uncertainty, probably because of the presence of the 0.4776 MeV capture gamma-ray line from the boron in the boron carbide sleeve, which was not separated in the analysis.

The energy bands

The opportunity to extract the information from a continuum signal using the Fourier transform approach is based on the fact that transform components are (ideally) un-correlated and can be thus

encoded independently. Different energy regions can be allotted to the continuum associated with each corresponding line, and in this paper we refer to this assignment process as the band method. The Fourier transform code processes the signal frame by frame for any arbitrarily selected window size and position. In an earlier study by Thakur and Arnold (1993), a 1 MeV energy band width was found capable of distinguishing several corresponding windows of the two thick target gamma-ray spectra, since the detailed shapes of the two spectra are different. Observing such differences in energy space would be difficult. Going to smaller window size, however, quickly diminishes this advantage; at 100 keV it almost disappears. For each individual spectrum, however, a better energy band corresponding to a given source can be devised depending on the positions of prominent lines in the spectra (Table 1).

#### FFT shows Power lies in first few frequency channels

We present as examples spectra obtained from two borehole depths i.e. 1170.00 meters and 1418.71 meters. An energy band for each corresponding line was extracted down until just above the next lowest energy line appears. Figure 6a shows parts of two sample spectra between 6.15 and 7.65 MeV. These two spectra have Fe, Ca, Si lines and are such that the line intensities of the iron neutron-capture lines at 7.646 MeV that are statistically not distinguishable, with peak areas calculated as  $1779 \pm 63$  and  $1844 \pm 71$ . Although the average channel by channel difference of the two lies above zero, it only represents the signal in zeroth frequency. There is more information in the next few frequencies. The frequency domain magnitude of the two sample spectra, with a stretched view of the points in the lower frequency region, is given in Figure 6b. Comparison of Figures 6a and 6b shows how easy it is to distinguish the Compton continuum signal from noise in the frequency domain, compared to working in the energy domain, especially with a difference of small statistical significance. The Fourier transform of the difference reaches very high values at low frequencies, corresponding to the small differences in the continuum. Above the first few frequency channels, it decreases rapidly to the background. A reconstruction of the continuum difference from the FFT is discussed in Thakur

and Arnold (1993). Successive addition of the lower frequency channels improves the result up to about the fifth channel. Afterwards it does not significantly enhance the observation while meaningless (noise) fluctuations become visible. This is how a cutoff point is estimated. The cutoff channel has been found to be less than eight in all cases.

#### Successive addition of the spectra of 20 seconds each

We tested specially two sets of spectra, 60 each, of 20 seconds counting time obtained at depths of 1157 meters and 1599 meters. Each six consecutive spectra were summed on a channel by channel basis to obtain spectra, each with 2 minutes total counting time. We thus have two sets of 10 spectra each at two depths 1157 and 1599 meters.

Si and Fe peak areas at 4.934 MeV and 7.646 MeV, respectively, were determined by the Ganymed program for gamma-ray spectrum analysis. The ratio of these two lines with their Poisson errors are plotted in Figure 7a. Continuum intensity estimates for these two lines were obtained in the energy domain. The Fe/Si continuum ratio, with 99% confidence error limit, is shown in Figure 7b. Comparing these two plots clearly demonstrates the advantage of using the continuum data in such a statistically limited case, both in terms of the scatter of and confidence in the measurement. The improvement in the statistical uncertainty is consistent with the ratio of continuum to peak counting rates, on the order of 100.

#### Calcium Results

Ca is a very interesting case for demonstrating the usefulness of this technique. A peak due to Ca-49 with a half life of 8.7 minutes occurs at 3.084 MeV in the A spectra and has no interference from any other peaks in the vicinity. In C spectra a line due to Ca-40 occurs at 6.42 MeV (easily seen in the 1740 minute spectrum). However in 20 minute C spectra the Ca peak to noise ratio is very poor (Figure 8). The peak often cannot be seen, and there are small Fe peaks nearby. This makes it a suitable candidate for using the continuum analysis to make a meaningful study of the variations of

Ca in the borehole rock.

Four continuum spectra of Ca are given in Figure 9a. These are normalized to the average of all the spectra for easy comparison. Figure 9a shows two 20 minute C spectra, with high and low calcium, respectively, as predicted from the elemental concentration determined from the corresponding A spectra. Five 20 minute spectra having higher Ca content (with varying individual values) were summed to obtain 100 minutes of accumulation time, and another five spectra were similarly summed for lower Ca content.

Although for the 100 minutes counting time set the variations in the Ca continuum is clearly visible, they do have high errors. On the other hand for the 20 minutes counting time, the effects are barely seen. All four sample spectra shown in Figure 9a are Fourier transformed and their magnitudes are plotted in Figure 9b. All four can be very clearly distinguished using their magnitude and phase information. For high Ca the sign of the phase of all the frequency channels shown in the plot, except the DC, are positive. On the other hand for low Ca they are all negative.

A table of relative Ca concentration as a function of depth was thus generated using the fast fourier transform of the continuum and appropriately normalizing the resultant values. These continuum values were then compared to the Ca peak analysis results obtained from the A spectra and are shown in Figure 10. Ca peak areas from the A spectra are corrected for spectral as well as geophysical contributions. There are a number of things to keep in mind here. First of all the depths in the two cases, namely A and C, are not exactly the same. Typically the differences in the depths are within a meter. A weighted average value of the relative Ca line intensity from nearest neighboring depths was obtained as a best approximation for the A spectra and was compared to the Ca continuum from the C spectra. The errors in the Ca peak areas obtained from the A spectra are between 10 and 45 percent. Despite these difficulties and unknown effects from the fact that these two spectral types involve slightly different physics, there seems to be good agreement between the two calculations, favoring the validity and importance of this approach.

The most desirable thing is to compare the ground truth laboratory assays of the borehole rock

samples with the fourier transform C data, corrected for geophysical variations in neutron flux, geometry and macroscopic thermal neutron capture cross section. Such a comparison is shown in Figure 11, where the relative Ca abundance, obtained by this method and appropriately normalized, is compared to the, properly normalized, XRF analysis of the cutting samples (Schweitzer et al., 1993). Remarkably good agreement is obtained. Ca was chosen because peaks due to this element are very weak (Figure 8) and the above correlation using the C spectra peak areas is not satisfactory (Figure 12). To us this is the best test of the method, because the peaks are insignificant and both Fe and Si continua are present. A more detailed statistical comparison of this analysis and peak analysis of capture and delayed activation spectra compared to laboratory XRF analysis of the samples from the borehole rock cuttings is given in Table 2. Among all independently obtained results, the one obtained by continuum analysis of C spectra is clearly the best. The relative Ca values obtained by the analysis of the 6.42 MeV peak of C spectra has the highest uncertainty and scatter in the correlation.

### CONCLUSIONS

There are a number of possible ways to further improve this analysis. In this example, the scatter of the continuum to peak ratio remains within the statistical error limits. It has been found that this scatter can be further minimized by taking into account the scatter in the peak shape, which is mainly determined by sigma and rho criterion as discussed previously. Other small corrections may be considered such as scatter in the peak intensity because of contribution from other undetected gamma-ray line, changes in the detector response parameters, contribution due to delayed neutron activation and natural radioactivity. These limiting factors should become more noticeable in the lower energy region.

We believe this method of improving the significance of gamma-ray measurements has broad applicability. The information is there to be used. It seems likely to be most useful in thick target observations. Here the continuum to line ratio is much higher than for a thin target, mainly because of internal Compton scattering. In addition, the exact geometry is less critical for thick targets. This

case occurs in a variety of applications, especially in natural settings, with or without an active neutron source.

The method is also favored for high gamma-ray energies, for which the peak/Compton ratio is low. Going down from the highest important energy line, errors must necessarily accumulate. However, as the example of Ca in our work indicates, it works quite well even for a weak line lying below two stronger ones.

Historically, spectroscopic studies of extended samples with scintillation detectors rapidly realized the importance of using information from the entire gamma-ray spectrum (Hertzog, 1980; Grau and Schweitzer, 1987 and 1989; Davis, 1980), rather than just the poorly resolvable peaks obtained with scintillation detectors. The advent of germanium detectors provided easily resolved peaks, seemingly eliminating the need for evaluating the complex continuum. However, this study shows that making use of the continuum information obtained with germanium detectors, in addition to that in peaks, can provide substantially improved statistical results, and, perhaps more importantly, improved sensitivity for elements which weakly contribute to the total spectral response. These two factors can be particularly important for measurements performed outside the laboratory environment, such as planetary measurements and subsurface borehole measurements, where there is often a strong limitation on the time available for measurement, and the maximum amount of information must be obtained from the detected counts. It should be noted again that this approach is particularly useful for spectra that contain reasonably high energy gamma-rays, i.e., where the total number of counts in the spectrum from a particular element is very large when compared the number of counts contained in the photopeaks.

Future work is needed to more fully evaluate the robustness of this technique in environments where the gamma-ray scattering properties of the sample are significantly altered, either through large changes in sample densities or where variable amounts of intervening material can be introduced between the sample and detector, or laboratory measurements where results are very sensitive to geometry. One such example is in boreholes that have had a steel casing inserted to preserve the

integrity of the hole. Because of imperfect cementing practices, there may be only water or several inches of cement between the rock being studied and the steel casing that separates the spectrometer from the rock. This variation can have a dramatic effect on the shape of the gamma-ray spectrum reaching the detector.

Most of the gamma-ray continuum spectrum results from nuclear interactions in and around the detector and thus it can be used to understand the chemical composition. A method has therefore been developed to process the continuum spectra of complex gamma-ray sources. It uses the Fourier transform, which is a linear operation, to isolate information from the continuum. Here we have used the neutron induced gamma-ray spectra of borehole rock at several depths as test samples. The results from applying this procedure have been successfully compared to the results from the laboratory analysis of numerous core samples. This method with proper calibration provides high sensitivity and reliable elemental concentration information from thick target sources such as borehole formations and other complex gamma-ray spectra with weak line intensities.

### Acknowledgements

This work was supported by NASA Grant NAG 5-530 and by JPL Contract 957578. We are indebted to the KTB management, especially Prof. R. Emmermann and J. K. Draxler, for assistance in obtaining the field measurements and the laboratory analyses, and to C. Peterson and M. Kuhr for assistance with the field measurements and spectral analysis.

### REFERENCES

- Beeck Op de J. (1979) Theoretical foundations of computer techniques for the analysis of gamma-ray spectra. In *Computers in Activation Analysis and Gamma-Ray Spectroscopy*, (Eds. B.S. Carpenter, M.D. D'Agostino and H.P. Yule), Proc. Am. Nucl. Soc. Topical Conf., Mayaguez, Puerto Rico, US Dept. of Energy, CONF-780421, pp. 1-25. Tech. Inf. Center/ US Dept. Energy.
- Bielefeld M. J., Reedy R. C., Metzger A. E., Trombka J. I. and Arnold J. R. (1976) Surface chemistry of selected lunar regions. Proc. Lunar Sci. Conf. 7th, pp. 2661-2676.
- Boynton W. V., Trombka J. I., Feldman W. C., Arnold J. R., Englert P. J. A., Metzger A. E., Reedy R. C., Squyres S. W., Wanke H., Bailey S. H., Bruckner J., Callas J. L., Drake D. M., Duke P., Evans L. G., Haines E. L., McCloskey F. C., Mills H., Shinohara C. and Starr R. (1992) Science applications of the mars observer gamma ray spectrometer. *J. Geophys. Res.* 97(E5), 7681-7698.
- Briesmeister J. F. (1986), Editor, MCNP a general monte carlo code for neutron and photon transport. Los Alamos National Laboratory Report LA-7396-M, Rev. 2.
- Couët B. and Hertzog R. C. (1992) Modeling analysis of environmental effects on accelerator porosity logging measurements. *IEEE Trans. Nucl. Sci.* 39 (4), 1002-1006.
- Davis P. A. J. (1980) Iron and titanium distribution on the moon from orbital gamma ray spectrometry with implications for crustal evolutionary models. *J. Geophys. Res.* 85 (B6), 3209-3224.
- Davis P. A. J. and Arnold J. R. (1979) Iron and titanium distribution on the lunar surface as determined by matrix inversion of gamma-ray orbital data. (abstract), *Lunar Planet. Sci.* X, pp. 268-270.

- Draxler J. K. (1992) Estimation of the mineral content of crystalline rock in the KTB-Oberpfalz VB. Scientific Drilling 3, 115-125.
- Ellis D. V. (1990) Neutron and gamma ray scattering measurements for subsurface geochemistry. Science 250 (4977), 82-87.
- Ghanem S. A., Gardner R. P. and Verghese K. (1993) Monte carlo simulation of the gamma-ray backscatter lithodensity logging tool response. Nucl. Geophys. 7 (2), 197-207.
- Grau J. A. and Schweitzer J. S. (1987) Prompt gamma-ray spectral analysis of well data obtained with NaI(Tl) and 14 MeV neutrons. Nucl. Geophys. 1, 157-165.
- Grau J. A. and Schweitzer J. S. (1989) Elemental concentrations from thermal neutron capture gamma ray spectra in geological formations. Nucl. Geophys. 3, 1-9.
- Grau J. A., Schweitzer J. S., Draxler J. K., Gatto H. and Lauterjung J. (1993) Elemental logging in the KTB pilot hole-I. NaI-based spectrometry. Nucl. Geophys. 7, 173-187.
- Halbleib J. A., Kensek R. P., Mehlhorn T. A., Valdez G. D., Seltzer S. M. and Berger M. J. (1992a) ITS version 3.0: The integrated TIGER series of coupled electron/photon monte carlo transport codes. Sandia National Laboratories, SAND91-1634:UC-405.
- Halbleib J. A., Kensek R. P., Valdez G. D., Seltzer S. M. and Berger M. J. (1992b) ITS: The integrated TIGER series of electron/photon transport codes - version 3.0. IEEE Trans. Nucl. Sci. 39 (4) 1025-1030.
- Hendricks J. S. and Briesmeister J. F. (1992) Recent MCNP developments. IEEE Trans. Nucl. Sci. 39 (4) 1035-1040.
- Hertzog R. C. (1980) Laboratory and field evaluation of an inelastic neutron scattering and capture gamma-ray spectroscopy tool. Soc. Petr. Eng. J. 20, 327-340.
- Kruse H. (1979) Spectra processing with computer graphics. In Computers in Activation Analysis and Gamma-ray Spectroscopy (Eds. B.S. Carpenter, M.D. D'Agostino and H.P. Yule), Proc. Am. Nucl. Soc. Topical Conf., Mayaguez, Puerto Rico, US Dept. of Energy, CONF-780421, pp. 76-84. Tech. Inf. Center/ US Dept. Energy.

- Metzger A. E. and Parker R. E. (1979) The distribution of titanium on the lunar surface. *Earth Planet. Sci. Lett.* 45, 155-171.
- Mills W. R., Stromswold D. C. and Allen L. S. (1991) Advances in nuclear oil well logging. *Nucl. Geophys.* 5 (3) 209-227.
- Pinault J. L. (1991) Application of the monte carlo method to simulate neutron gamma logging tool behavior. *Nucl. Geophys.* 5 (3), 229-246.
- Schweitzer J. S. (1991) Nuclear techniques in oil industry. *Nucl. Geophys.* 5 (1-2), 65-90.
- Schweitzer J. S., Peterson C. A. and Draxler J. K. (1993) Elemental logging with a germanium spectrometer in the continental deep drilling project. *IEEE Trans. Nucl. Sci.* 40 (4), 920-923.
- Schweitzer J. S., Peterson C. A. and Draxler J. K. (1994) Elemental logging in the KTB pilot hole-II. Ge-based spectrometry, to be submitted to *Nucl. Geophys.*
- Soran P. D. (1988) Nuclear modeling techniques and nuclear data. *IEEE Trans. Nucl. Sci.* 35 (1), 847-851.
- Thakur A. N. and Arnold J. R. (1993) A sensitive continuum analysis method for gamma ray spectra. *Nucl. Instr. and Meth.* A325, 529-536.
- Ullo J. J. (1986) Use of multidimensional transport methodology on nuclear logging problems. *Nucl. Sci. Eng.* 92 (2), 228-239.
- Yadav J. S., Bruckner J. and Arnold J. R. (1989) Weak peak problem in high resolution gamma-ray spectroscopy. *Nucl. Instr. and Meth.* A277, 591-598.

Table 1

Major gamma-ray line energy sources used to generate the corresponding detector spectra by the Monte Carlo method (MCNP and ITS code) and the resulting associated continuum. The scatter in calculated continuum to peak ratio of the borehole gamma-ray spectra at different energies, and their individual standard deviations are also tabulated.

Line Sources	Energy [MeV]	Continuum [MeV]	Continuum/ Peak area	Standard Deviation
ANN.	0.511	0.4000 - 0.5150	66.4	373.5
H (n, $\gamma$ )	2.2233	0.8507 - 2.2273	397.8	57.6
Si (n, $\gamma$ )	3.5395	2.2283 - 3.5435	393.8	48.9
Si (n, $\gamma$ )	4.934	3.5445 - 4.9380	304.6	35.2
Ca (n, $\gamma$ )	5.515	4.9390 - 5.5190	120.6	45.7
Ca (n, $\gamma$ )	6.42	5.5200 - 6.4220	201.8	39.5
Fe (n, $\gamma$ )	7.6455	6.1344 - 7.6495	367.0	26.0
Fe (n, $\gamma$ )	9.299	7.6505 - 9.3030	352.6	23.4

Table 2

The statistical comparison of the results obtained by this analysis and a peak analysis of capture and delayed activation spectra compared to the laboratory analysis of the samples from borehole rock cuttings for calcium.

	Comparison of laboratory analysis data, of Ca using XRF technique, of cuttings with the following:		
	Ca Peak of A spectra	Ca Peak of C spectra	Ca Continuum of C spectra using FFT technique
Intercept (Relative Ca)	-5.13	16.18	2.38
Slope (Relative Ca/ Ca Wt %)	11.60	7.69	13.66
Standard Error of Slope	1.03	1.27	0.50
Standard Deviation	4.09	7.38	1.95
R Squared	0.598	0.302	0.896
No. of Observations	138	87	87
Degrees of Freedom	136	85	85

## FIGURE CAPTIONS

- Fig. 1 Delayed neutron activation spectrum ("A") with primary gamma-ray peaks identified.
- Fig. 2 Neutron capture gamma-ray spectrum ("C") obtained with a borehole spectrometer using a germanium detector.
- Fig. 3 Peak area of the 7.646 and 5.515 MeV lines of the C spectra as a function of depth. The Poisson errors are between 3.6 and 7.9 percent; other errors are present (see text).
- Fig. 4 A continuum spectrum calculated by a Monte Carlo method is compared to the gamma-ray continuum spectrum obtained in a borehole.
- Fig. 5a Comparison of peak area at 7.646 MeV to its corresponding continuum in the C spectra. The continuum is estimated in energy space and is arbitrarily scaled for convenience.
- Fig. 5b Comparison of peak area at 5.515 MeV to its corresponding continuum in the C spectra. The continuum is estimated in energy space and is arbitrarily scaled for convenience.
- Fig. 6a Two sample spectra having comparable peak areas for the line at 7.646 MeV. First and second escape peaks are also shown. Peaks are indistinguishable within statistical errors.
- Fig. 6b Frequency domain Fourier transform of the two spectra of Fig. 6a. The solid line is the difference of the two. A difference in the lower frequency region is clearly noticeable.
- Fig. 7a Fe/Si peak ratio in C-spectra at two depths with a counting time of 2 minutes for each sample.
- Fig. 7b Fe/Si continuum ratio of the corresponding lines of Fig. 7a with 99 % confidence error limit showing improved precision.
- Fig. 8 Ca peak at 6.42 MeV in one 20 minute spectrum and in all 87 spectra summed together (1740 minutes).
- Fig. 9a Ca continuum spectra at depths with high and low relative Ca content with counting times of 20 minutes and 100 minutes each.
- Fig. 9b Frequency space transforms of the Ca continuum shown in Fig. 9a. The lower twenty frequency channels are shown.
- Fig. 10 Continuum FFT estimates of Ca in C spectra compared with the 3.084 MeV peak area of the A spectra due to Ca. All values are appropriately normalized.
- Fig. 11 Continuum FFT estimates of Ca compared to laboratory XRF analysis of borehole cutting samples. All values are appropriately normalized.
- Fig. 12 6.42 MeV peak area of C spectra due to Ca compared with laboratory XRF analysis of borehole cutting samples. All values are appropriately normalized.

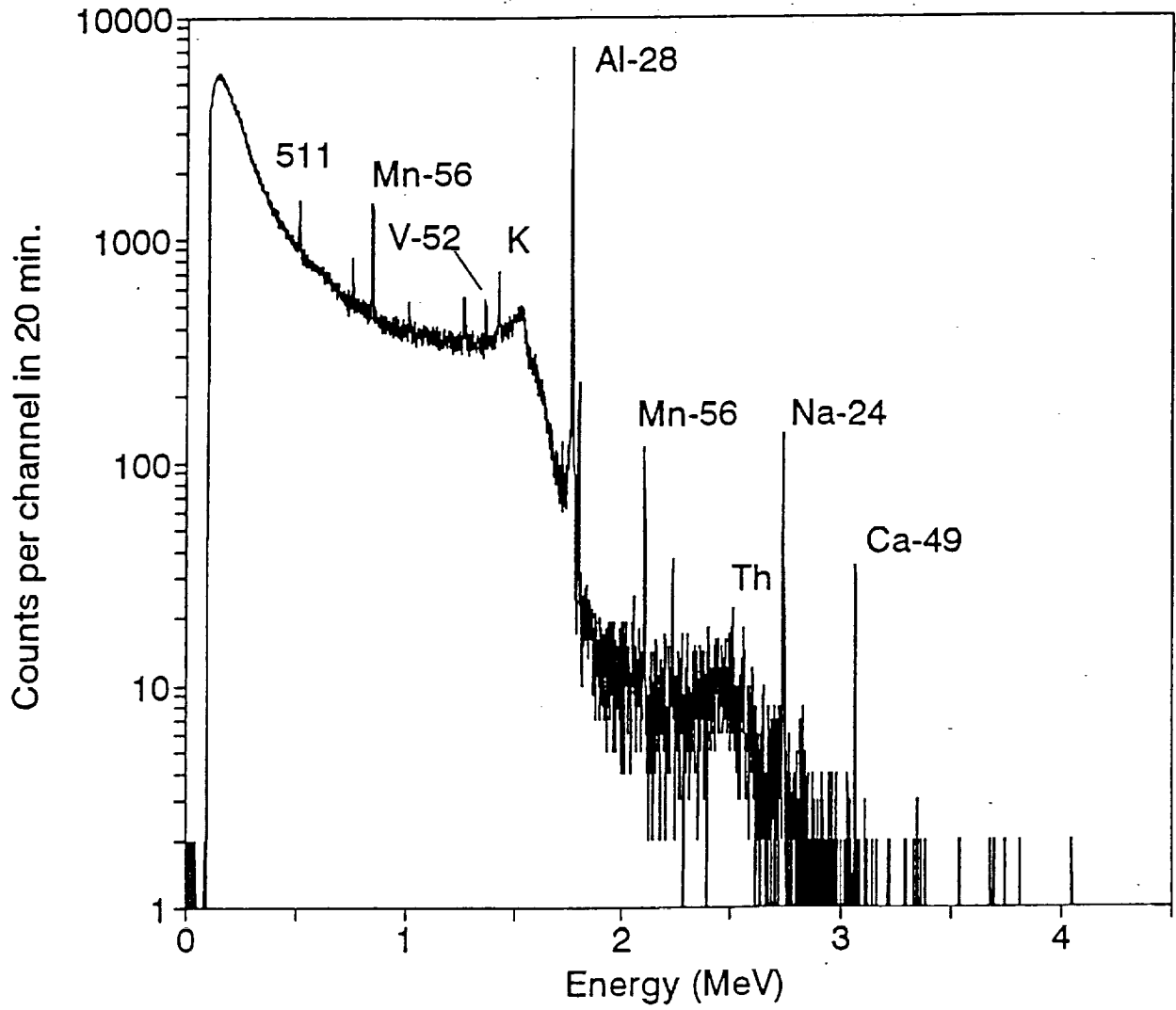


Fig. 1

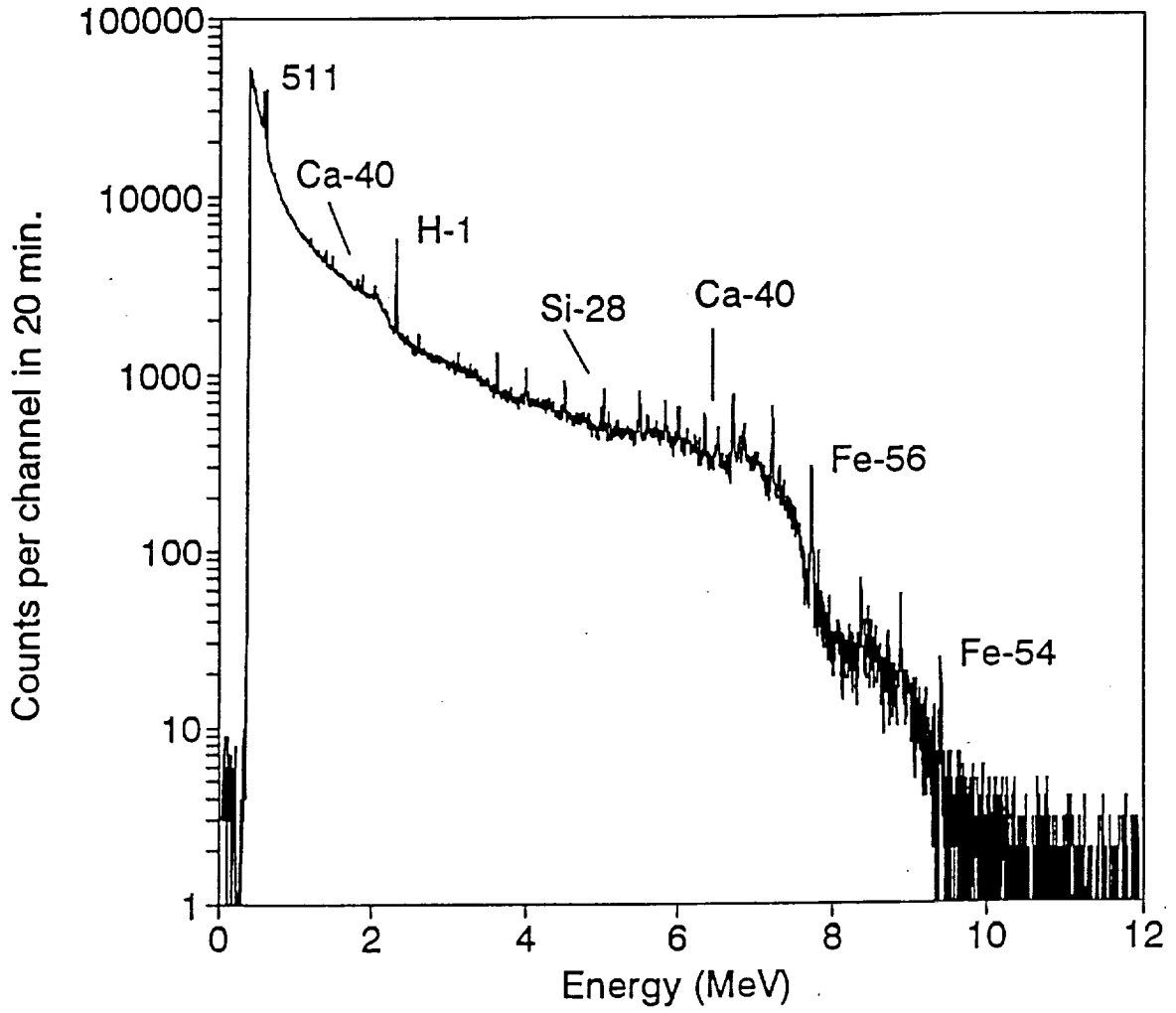


Fig. 2

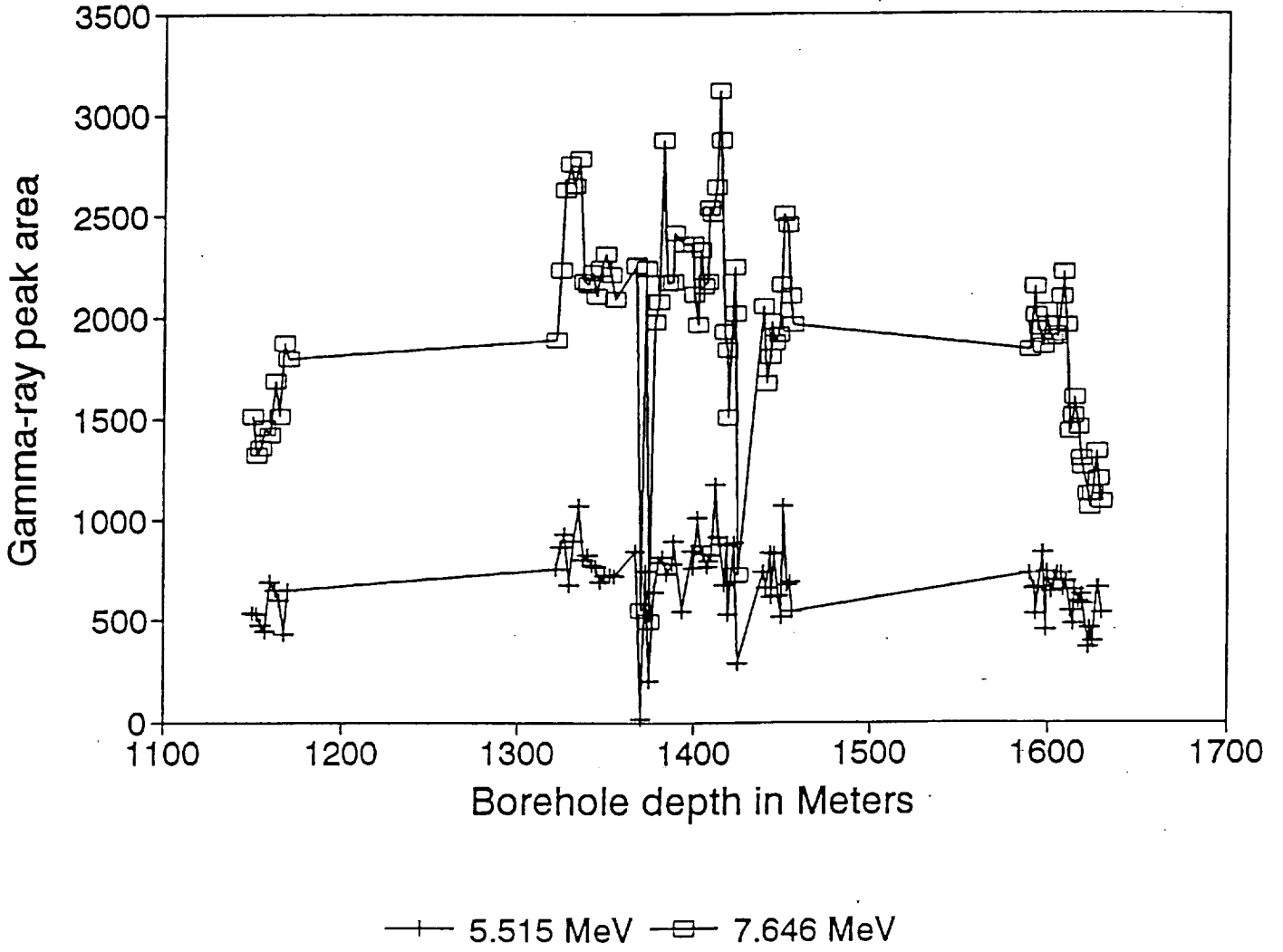


Fig. 3

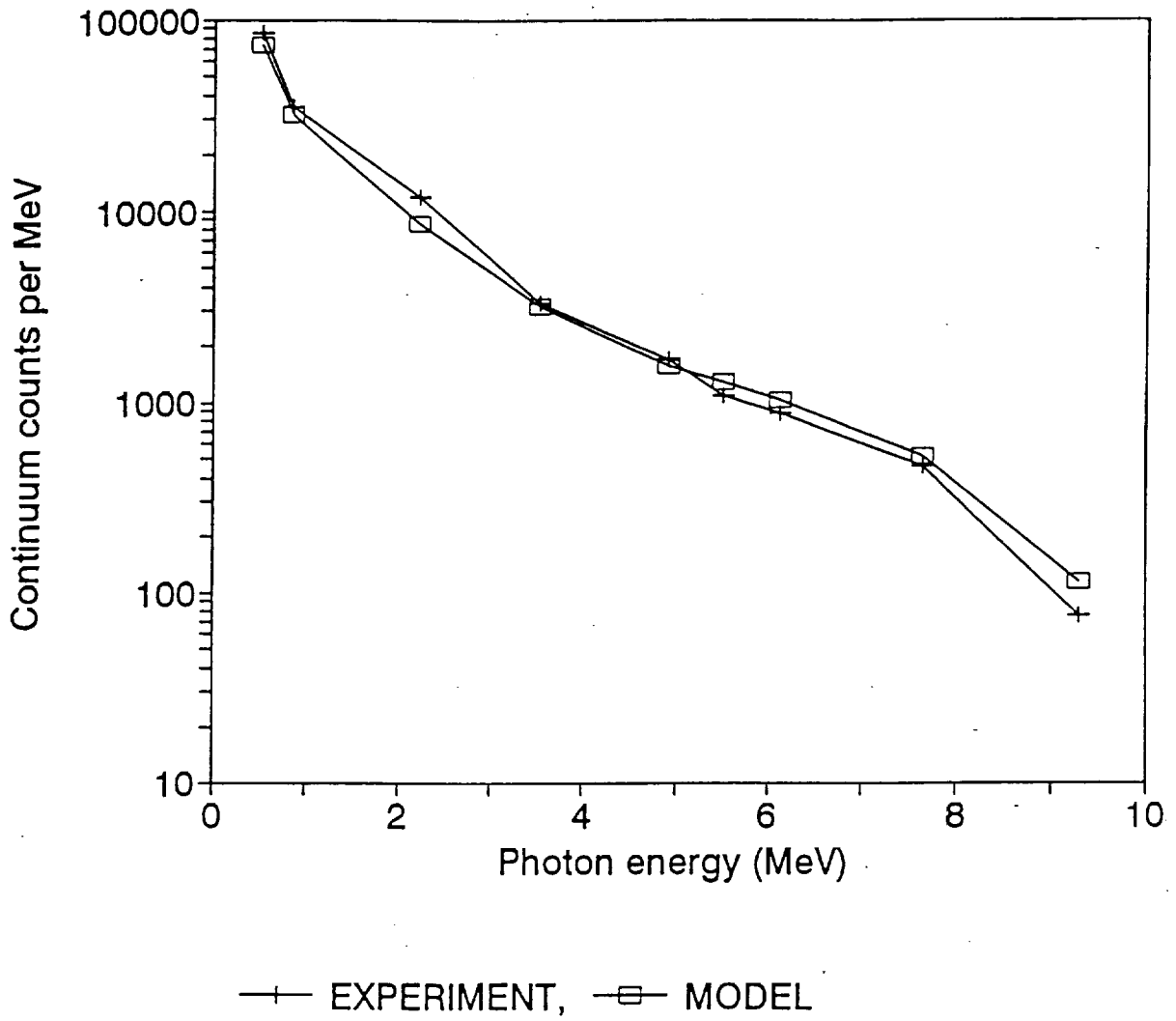


Fig. 4

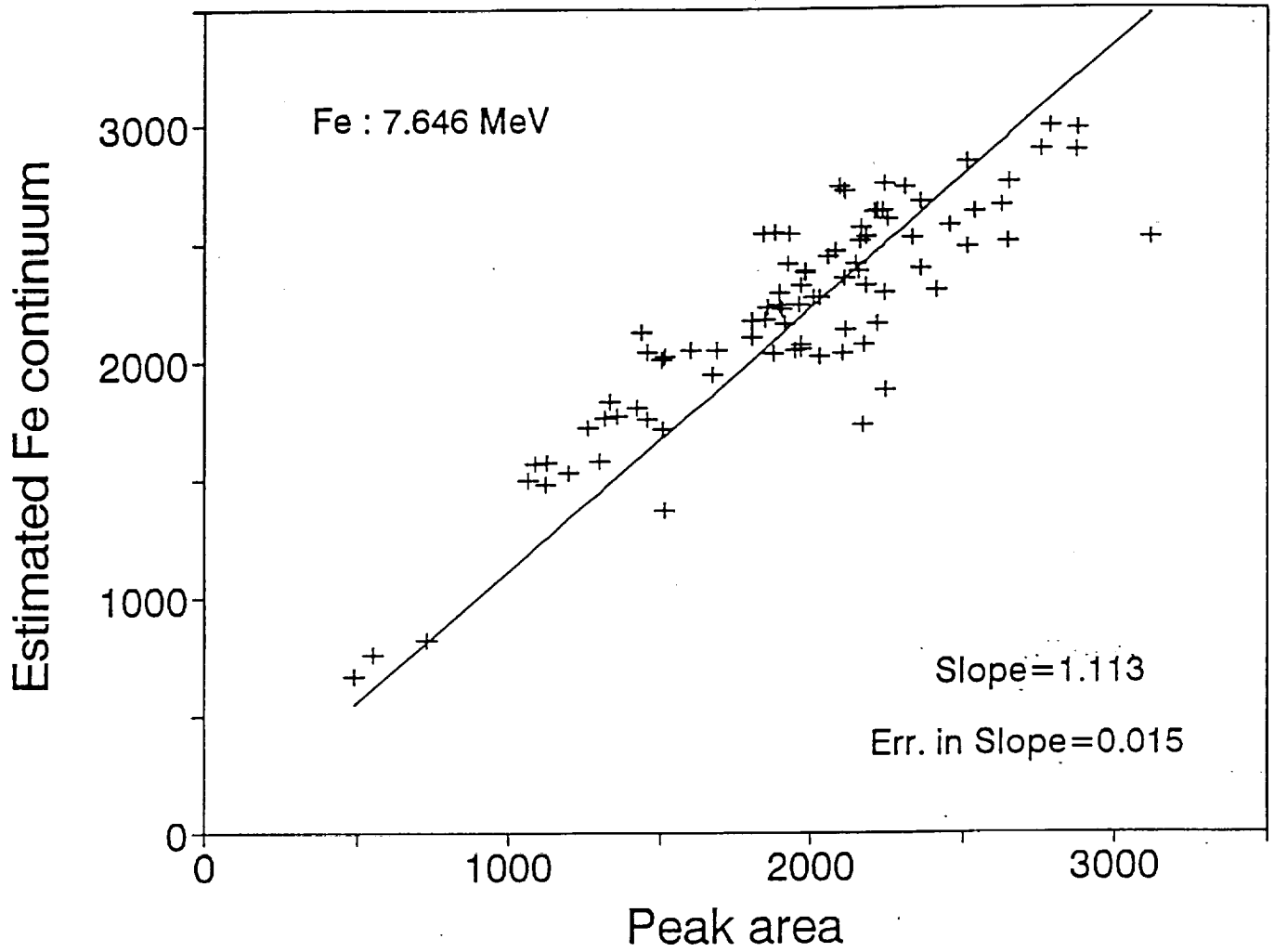


Fig. 5a

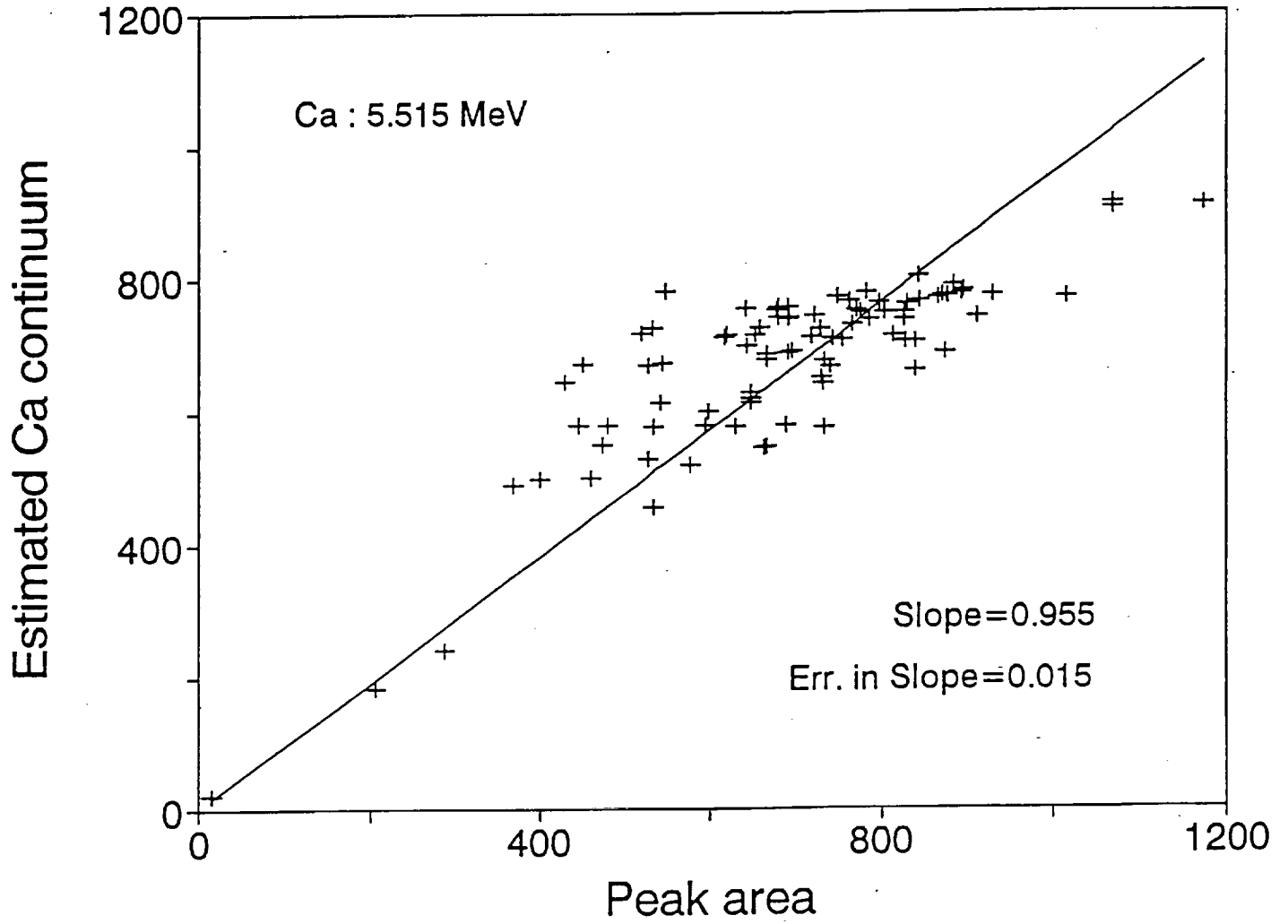


Fig. 5b

Table 1: Inorganic Scintillators

Crystal	Z	Density (g/cm <sup>3</sup> )	Refractive Index	Hygro- scopic	Radiation Length (cm)	$\lambda$ Fast Component (nm)	$\lambda$ Slow Component (nm)	Decay Fast Comp (ns)	Decay SlowComp (ns)	Yield % NaI <sup>a</sup>	Light Yield (phot/MeV)
BGO	75	7.13	2.19	no	1.11	480	-	300	-	13	8200
BaCl <sub>2</sub>	50	3.90	-	-	-	-	-	1.2, 3.5	-	-	25000
BaF <sub>2</sub>	53	4.88	1.49	no	2.06	220	310	0.60	620	5 <sup>b</sup>	2200 <sup>b</sup>
BaI <sub>2</sub>	54	5.15	-	no <sup>c</sup>	-	190-340	-	6	-	-	-
BaLiF <sub>3</sub>	51	5.24	-	-	2.13	240-440	-	<25	-	5	2200
BaYb <sub>2</sub> F <sub>8</sub>	63	6.99	-	-	1.3	>310	-	-	-	-	-
CaF <sub>2</sub>	17	3.19	1.44	no	-	435	-	940	-	40	24000
CaWO <sub>4</sub>	67	6.12	1.92	no	-	430	-	500	20 $\mu$ s	50	18000
CdI <sub>2</sub>	52	5.67	-	-	1.5	540	-	3	-	-	-
CdWO <sub>4</sub>	65	7.90	2.2 - 2.3	no	1.06	540	-	5 $\mu$ s	-	40	15300
CeCl <sub>3</sub>	51	3.90	-	-	-	-	-	4.4, 23	-	-	28500
CeF <sub>3</sub>	53	6.16	1.68	no	1.7	310	340	5	30	4	4000
CeF <sub>3</sub> (Ca)	53	6.10	-	slightly	1	340	-	30	-	-	-
CsBr	50	4.40	-	no	-	250	390	.07	>500	5	900
CsCaCl <sub>3</sub>	47	2.90	-	-	-	205-305	-	<1	-	10	5000
CsCl	52	4.00	-	no	-	240-270	390	.88	>500	5	900
CsF	53	4.11	1.48	very	2.0	390	-	2.80	4.40	5	2500
CsI	54	4.53	1.80	slightly	1.86	320	> 400	10	> 1 $\mu$ s	4	2000
CsI(Na)	54	4.53	1.84	yes	1.86	420	-	630	-	75	39000
CsI(Tl)	54	4.53	1.80	slightly	1.86	565	-	1 $\mu$ s	-	45	52000
Gd <sub>2</sub> SiO <sub>5</sub>	59	6.71	1.85	no	1.38	440	-	56	600	25	10000
KCaF <sub>3</sub>	17	3.00	-	-	-	140-190	-	<2	-	5	2200
KLuF <sub>4</sub>	63	4.80	-	-	2	165-200	-	1.5	-	-	170-400
KMgF <sub>3</sub>	15	3.16	-	-	7,72	140-190	180	1.5	-	2	3500

<sup>a</sup> Relative Pulse Height with a Bialkali Photocathode

<sup>b</sup> Fast Component only

<sup>c</sup> Unstable in Air

Crystal	Z	Density (g/cm <sup>3</sup> )	Refractive Index	Hygro- scopic	Radiation Length (cm)	$\lambda$ Fast Component (nm)	$\lambda$ Slow Component (nm)	Decay Fast Comp (ns)	Decay SlowComp (ns)	Yield % NaI <sup>a</sup>	Light Yield (phot/MeV)
KYF4(Rb)	33	3.60	-	-	-	140-190	-	1.9	-	5	2200
LSO	66	7.40	1.82	no	1.14	420	-	12	42	75	-
LXe	54	3.06	1.5	-	2.77	170	-	3 - 25	-	-	26000
LaF3(Ce)	53	>5.9	1.70	-	-	290, 305	-	3-27	-	-	2200
LaF3(Nd)	53	5.94	1.70	no	-	173, 245	-	6.3	-	5	200
LiBaF3	51	4.90	-	-	2.3	200-230	-	1.9	-	5	2200
LiI(Eu)	52	4.08	1.96	yes	-	470	-	600	1.4 $\mu$ s	35	11000
LiYbF4	64	6.09	-	-	1.56	400-500	-	<25	-	5	2200
NaI(Tl)	51	3.67	1.85	yes	2.6	415	-	230	1.5 ms	100	38000
PbCO3	76	6.6	1.80	no	-	475	-	5.6	27, 155	<1	-
RbCaF3	31	2.83	-	-	-	-	-	1	-	5	2200
RbF	35	3.60	-	yes	-	200, 380	-	1.3	-	5	2200
ThF4	85	6.32	-	-	1.18	330, 450	-	<25	-	-	-
Y3Al5O12	33	4.56	-	-	3.5	550	-	65	-	12	14000
YAlO3(Ce)	33	5.55	1.94	no	2.63	350-390	-	17-35	-	30	18500
YSO	35	4.54	-	-	-	400	500	37	82	25	-
ZnO	29	5.61	2.02	no	-	385	-	-	-	40	-
ZnS(Ag)	28	4.09	2.35	no	-	450	-	200	-	150	-
ZnWO4	64	7.84	2.20	no	1.12	475	-	5 $\mu$ s	20 $\mu$ s	26	9500

<sup>a</sup> Relative Pulse Height Measured with BiAlkali Photocathode.

Table 2a: Promising High Density Scintillators

Crystal	Z	Density (g/cm <sup>3</sup> )	Refractive Index	Hygroscopic	Radiation Length (cm)	$\lambda$ Fast Component (nm)	$\lambda$ Slow Component (nm)	Decay Fast Comp (ns)	Decay SlowComp (ns)	Yield % NaI <sup>a</sup>	Light Yield (phot/MeV)
BGO	75	7.13	2.19	no	1.11	480	-	300	-	13	8200
CaWO <sub>4</sub>	67	6.12	1.92	no	-	430	-	500	20 $\mu$ s	50	18000
CdWO <sub>4</sub>	65	7.90	2.2 - 2.3	no	1.06	540	-	5 $\mu$ s	-	40	15300
Gd <sub>2</sub> SiO <sub>5</sub>	59	6.71	1.85	no	1.38	440	-	56	600	25	10000
LSO	66	7.40	1.5	no	1.14	420	-	12	42	75	-
ZnWO <sub>4</sub>	64	7.84	2.20	no	1.12	475	-	5 $\mu$ s	20 $\mu$ s	26	9500

<sup>a</sup> Relative Pulse Height with a Bialkali Photocathode

Table 2b: Promising Medium Density Scintillators

Crystal	Z	Density (g/cm <sup>3</sup> )	Refractive Index	Hygroscopic	Radiation Length (cm)	$\lambda$ Fast Component (nm)	$\lambda$ Slow Component (nm)	Decay Fast Comp (ns)	Decay SlowComp (ns)	Yield % NaI <sup>a</sup>	Light Yield (phot/MeV)
LSO	66	7.40	1.82	no	1.14	420	-	12	42	75	-
NaI(Tl)	51	3.67	1.85	yes	2.6	415	-	230	1.5 ms	100	38000
YSO	35	4.54	-	-	-	400	500	37	82	25	-
CsI(Na)	54	4.53	1.84	yes	1.86	420	-	630	-	75	39000
CsI(Tl)	54	4.53	1.80	slightly	1.86	565	-	1 $\mu$ s	-	45	52000

<sup>a</sup> Relative Pulse Height Measured with Bialkali Photocathode.

## Compact PMTs

Schlumberger-EMR has a line of photomultipliers well suited to well logging applications in extremely harsh conditions. The expertise was developed and successfully applied Measurement-While-Drilling (MWD) operations, which subject the tool and detector to shock levels in excess of 500 g in a continuous fashion, and high levels of random vibrations. Problems arising from size limitations led to the development of compact PMTs with similar characteristics but a drastically reduced size. Tests conducted in 1993 for the qualification of this novel detector showed no performance degradation while allowing a smaller detector package. An added advantage was the development of extremely compact power supplies that use the volume around the electron multiplier structure. This development allowed operation of the detector to higher count rates than before, with higher reliability and linearity, while still reducing the original detector size.

The original size of a 1.25" diameter photomultiplier was 4.2" long. The compact PMT of the same diameter is 2.5" long when fully packaged with its biasing resistor network and the shock resistant potting. The integrated power supply brings the package to 3.1" length with no change in diameter. The power supply delivers up to 2400 V and operates up to 150°C, with a higher temperature version being finalized in the first half of 1994.

A similar approach is being applied to larger diameter ( 2" - 3" ) photomultipliers. A 3" photomultiplier can be packaged to a length of 3.5". This technology is being employed in the  $\gamma$ -ray detector for the NEAR project.

It is worth mentioning that these photomultipliers were developed for a large range of temperatures up to 200°C. The photocathodes are being matched to the various emission characteristics of the scintillating crystals, including, but not limited to, NaI(Tl), BGO, and GSO ( gadolinium oxyorthosilicate). Detectors including these scintillators are being successfully used in various applications.

## Short Term Plans

- Microchannel Plate (MCP) PMTs

Replacing the multiplying structure in a PMT by a set of Multi Channel Plates could result in a significant length and weight reduction. MCP-PMTs provide an imaging capability which might considerably enhance the performance of present X-ray detection systems. Prototypes of such MCP-PMTs exist. The performance characteristics of these devices will be investigated.

- Channel Electron Multiplier (CEM) PMTs

The main topic of this investigation is to determine if Channel Electron Multipliers can replace the classical PMT with an advantage in size, weight, or performance.

- Other solid state electron multiplication devices

There are several possibilities to employ Avalanche Photo Diodes (APDs) to replace some parts of the multiplying structure in a classical PMT.

- Miniature Detectors

Certain combinations of scintillating crystals, compact PMTs, and integrated power supplies offer unique characteristics of compactness, reliability, and performance for specific applications. The most promising combinations will be evaluated.

- Space Qualification of Integrated Power Supplies

The miniaturized power supplies mentioned above have excellent characteristics of stability, ruggedness, and operating temperature range. When used with the small size PMTs they use the available space very efficiently and improve the high count rate linearity. They contain both passive and active surface mount components. The space worthiness of these power supplies will be evaluated.

Appendix 1

## A NEUTRON ACTIVATION GAMMA RAY SPECTROMETER FOR PLANETARY SURFACE ANALYSIS

J.G. Bradley

Jet Propulsion Laboratory, 306-336  
California Institute of Technology  
4800 Oak Grove Drive  
Pasadena, California 91109

J.S. Schweitzer, J.A. Truax  
Schlumberger-Doll Research  
Old Quarry Road  
Ridgefield, Connecticut 06877

A. Rice, T.A. Tombrello  
California Institute of Technology, 200-36  
Pasadena, California 91125

### ABSTRACT

A pulsed DT neutron generator system, similar to that used in commercial well logging, offers the possibility of performing accurate elemental analyses to depths of tens of centimeters in a few seconds with the probe on the body's surface. Through time-phased measurements of the gamma-ray spectrum synchronized with the neutron pulses, concentrations of hydrogen, carbon and key mineral forming elements can be determined even with a low-resolution spectrometer. If a high resolution spectrometer is used, the number of elements measured and the sensitivity for measurement is increased. An implanted probe system, such as in a comet or ice cap penetrator, would offer the highest possible sensitivity.

An inexpensive neutron probe system based on modifications of the Schlumberger well-logging system has been proposed for the Discovery/Venera/SAGE Mission to Venus and the Mars Polar Pathfinder. Preliminary experiments on a simulated Venusian surface indicate that high quality results can be obtained.

### INTRODUCTION

There are a number of planned and contemplated NASA, ESA, and Russian solar system lander missions that will characterize planets and small bodies over the next ten years. These include missions to the Moon, Mars, Venus, asteroids and comets. Except for gamma-ray spectrometers, the existing suite of "demonstrated" instruments can only characterize the first fraction of a millimeter of the surface for elemental composition unless drilling or excavating techniques are used. Cosmic-ray induced activation analysis by gamma-ray counting can determine the composition of significant volumes, but only with tens of hours counting time for high quality measurements.

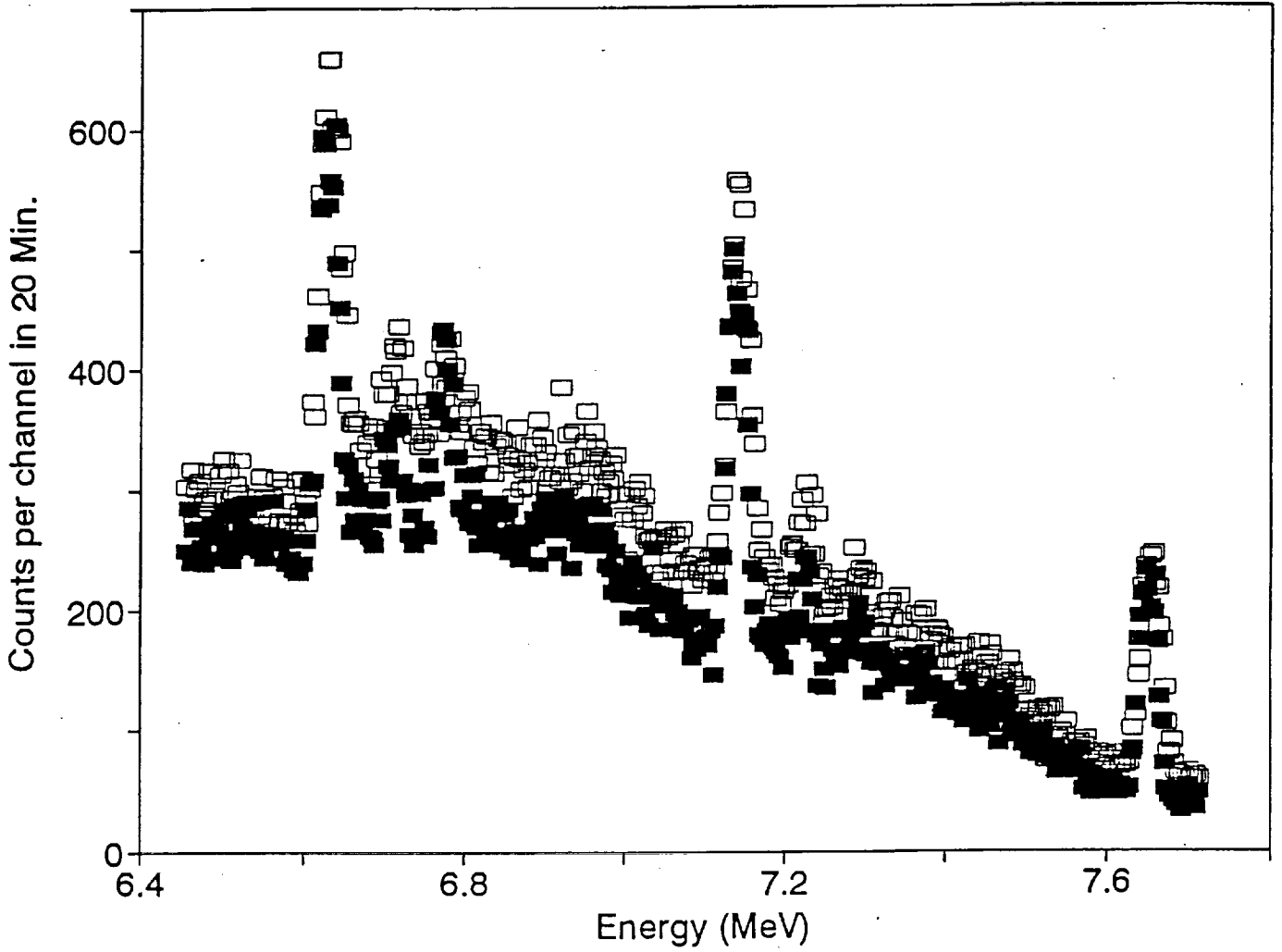
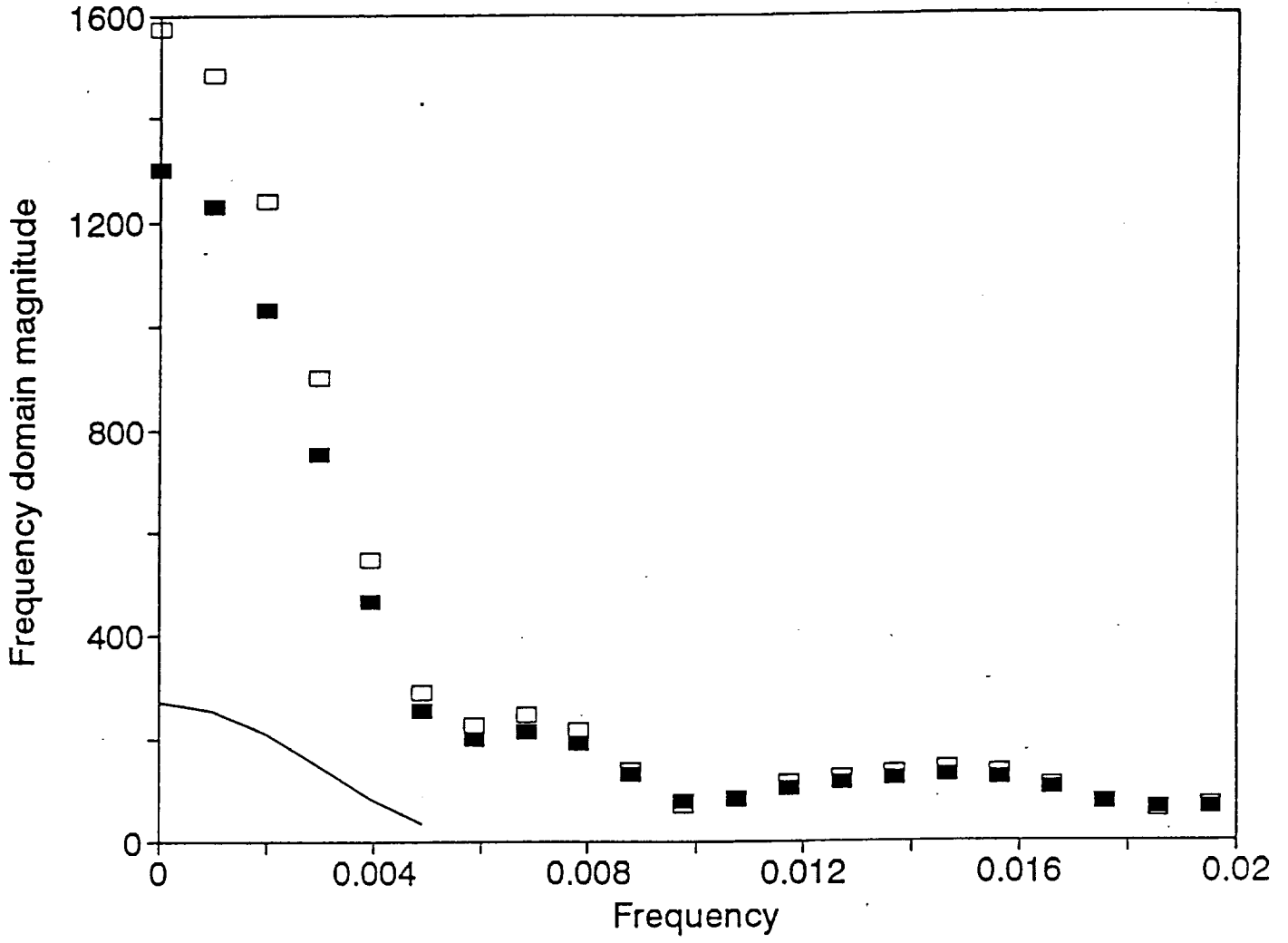
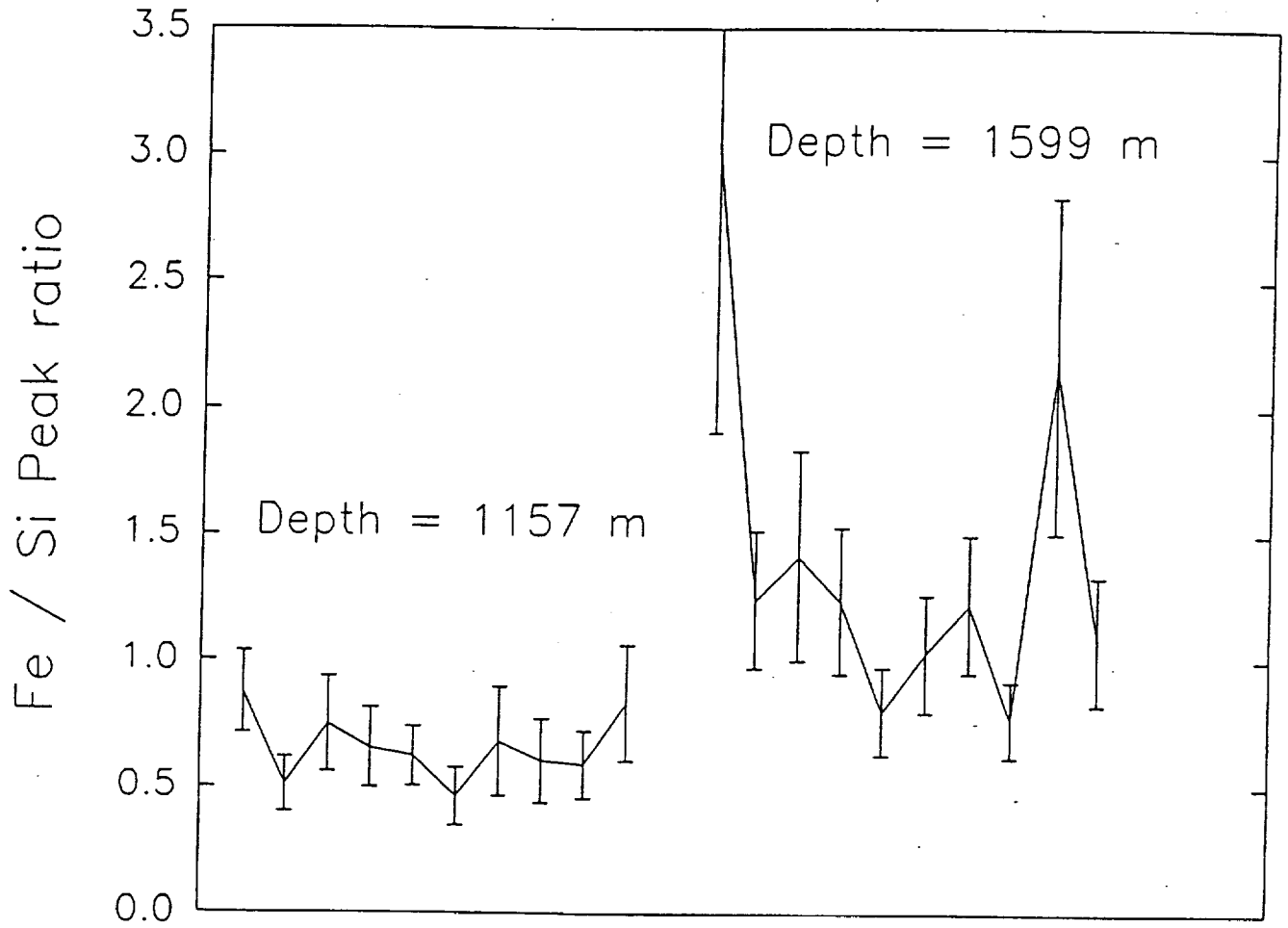
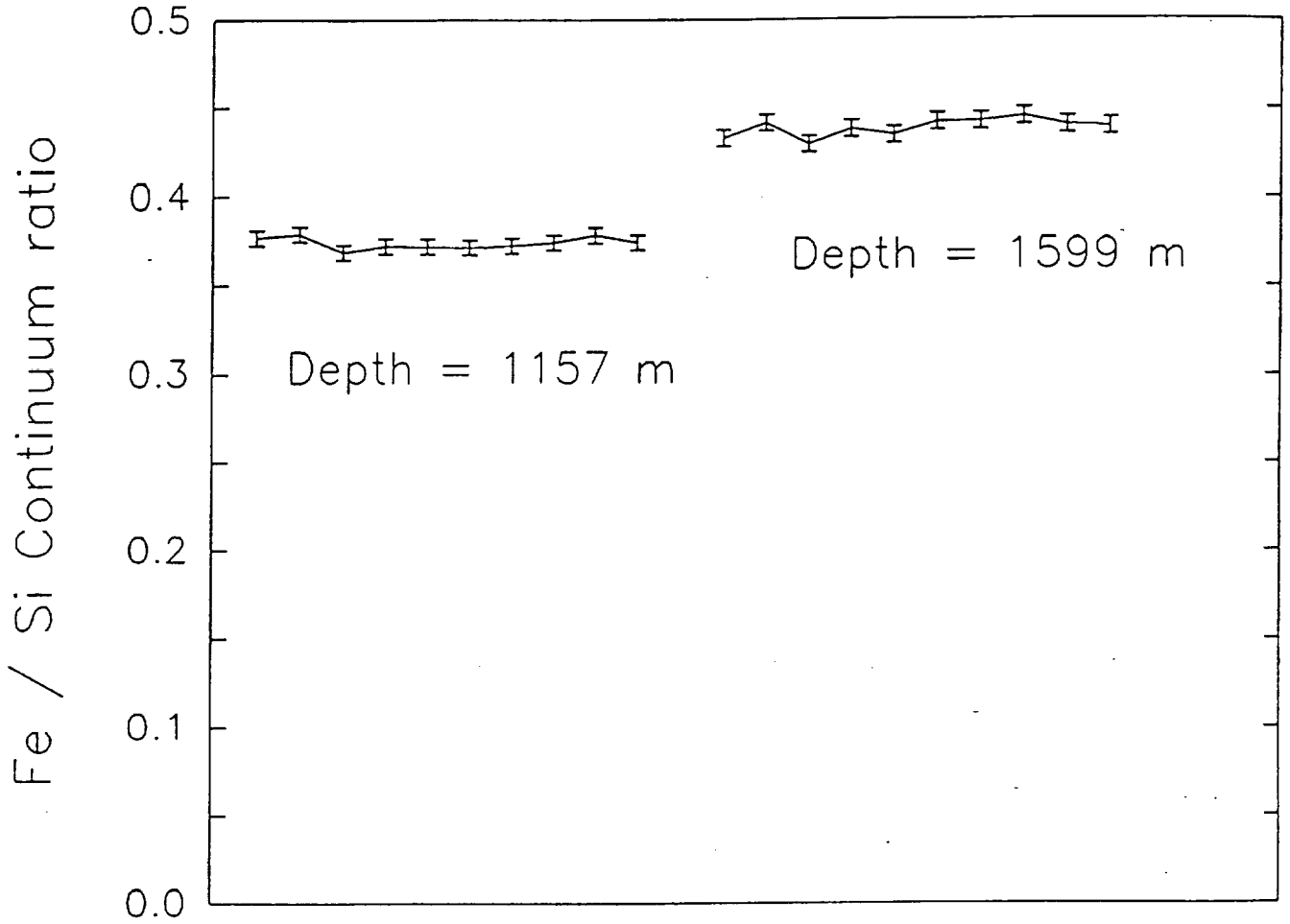


Fig. 6a





2 Min. accumulation spectra



2 Min. accumulation spectra

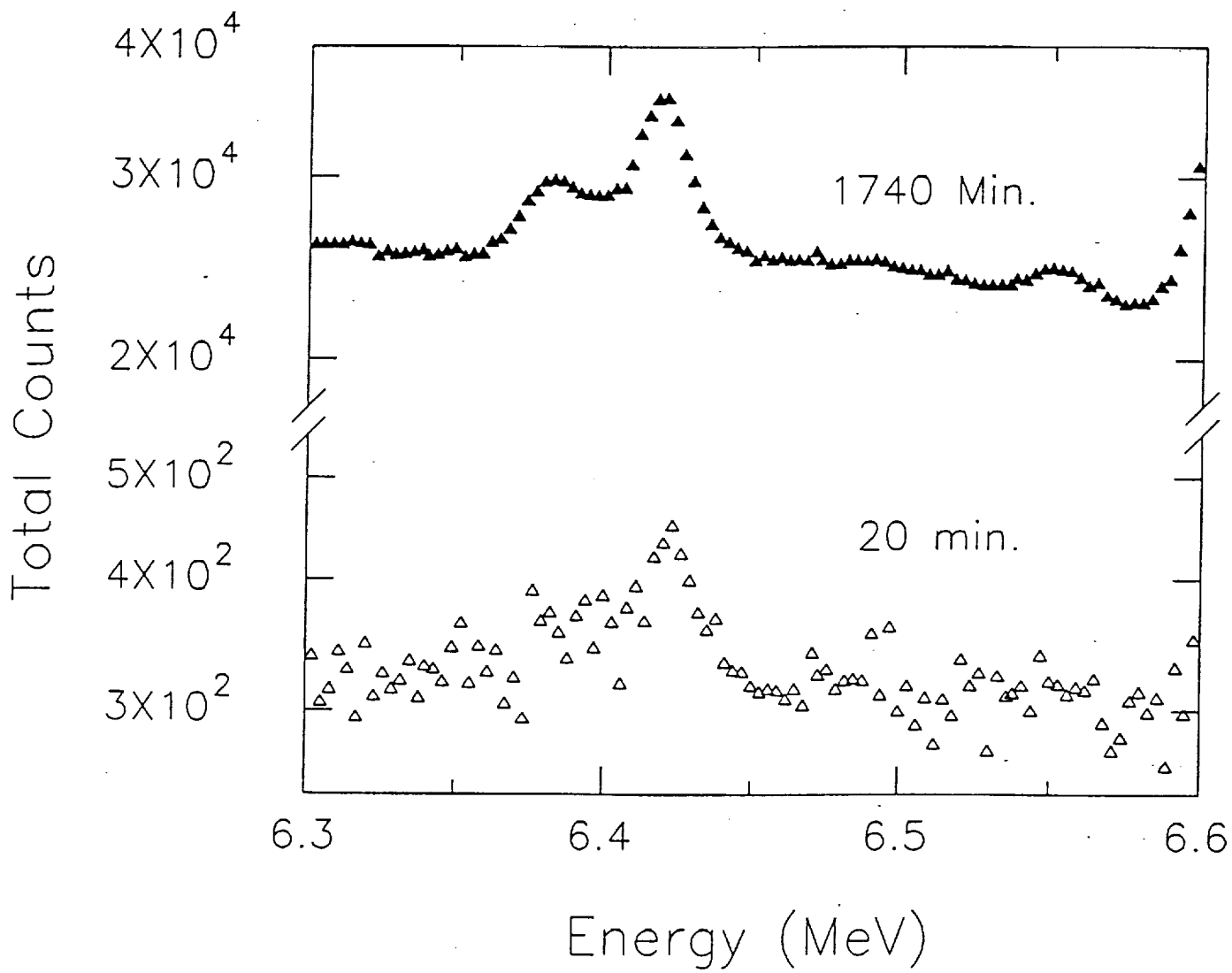


Fig. 8

RELATIVE COUNTS

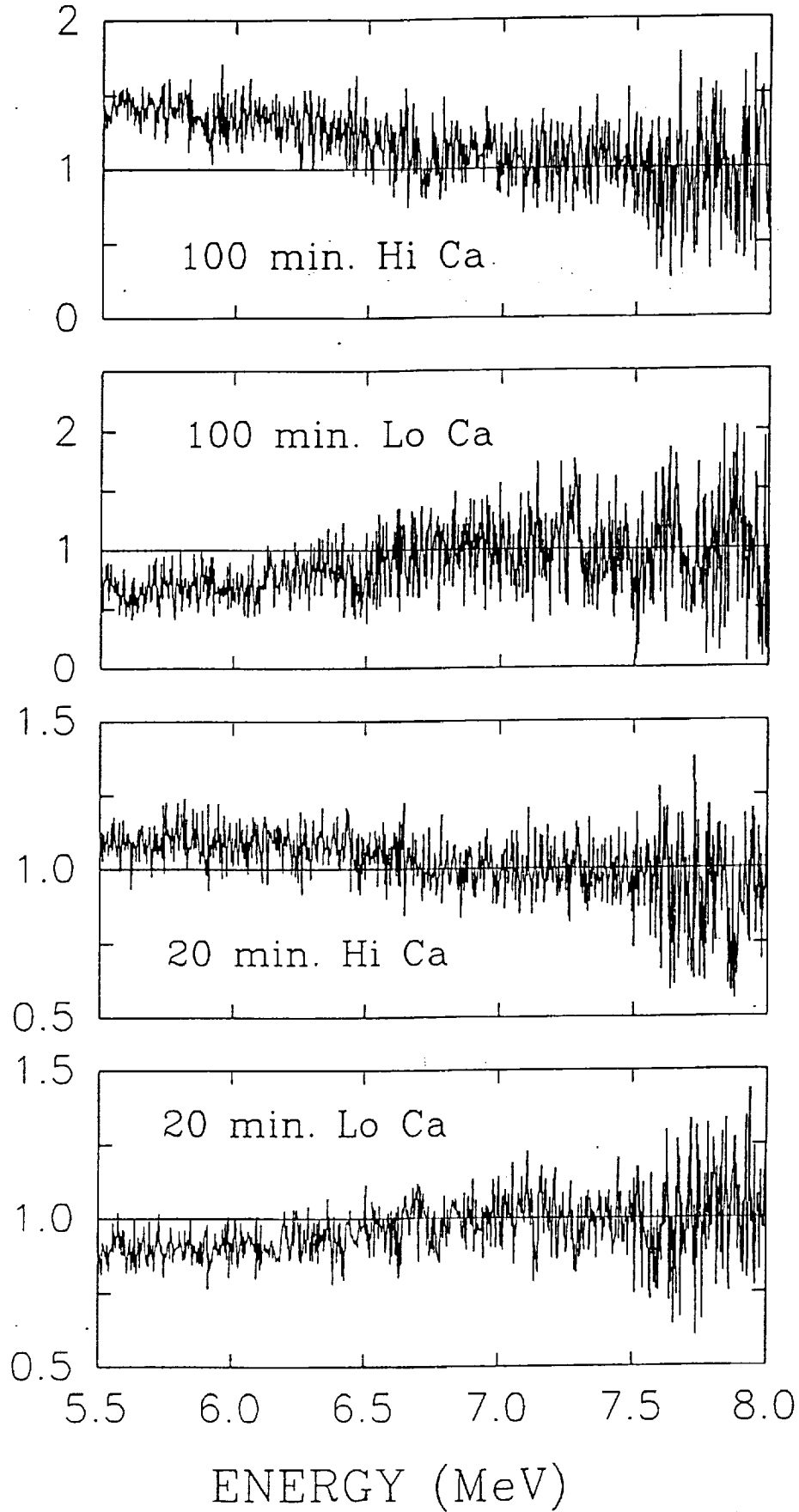


Fig. 9a

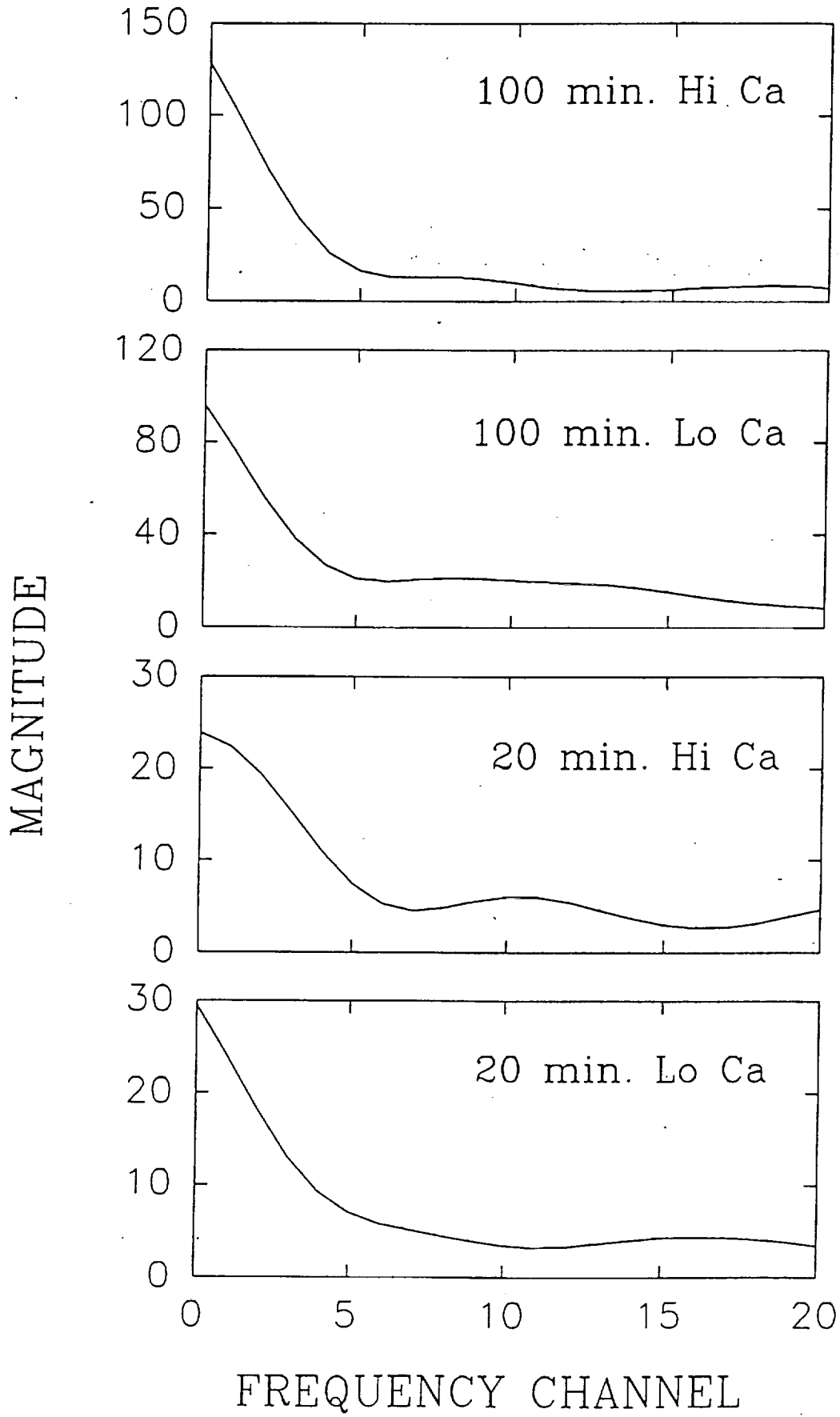
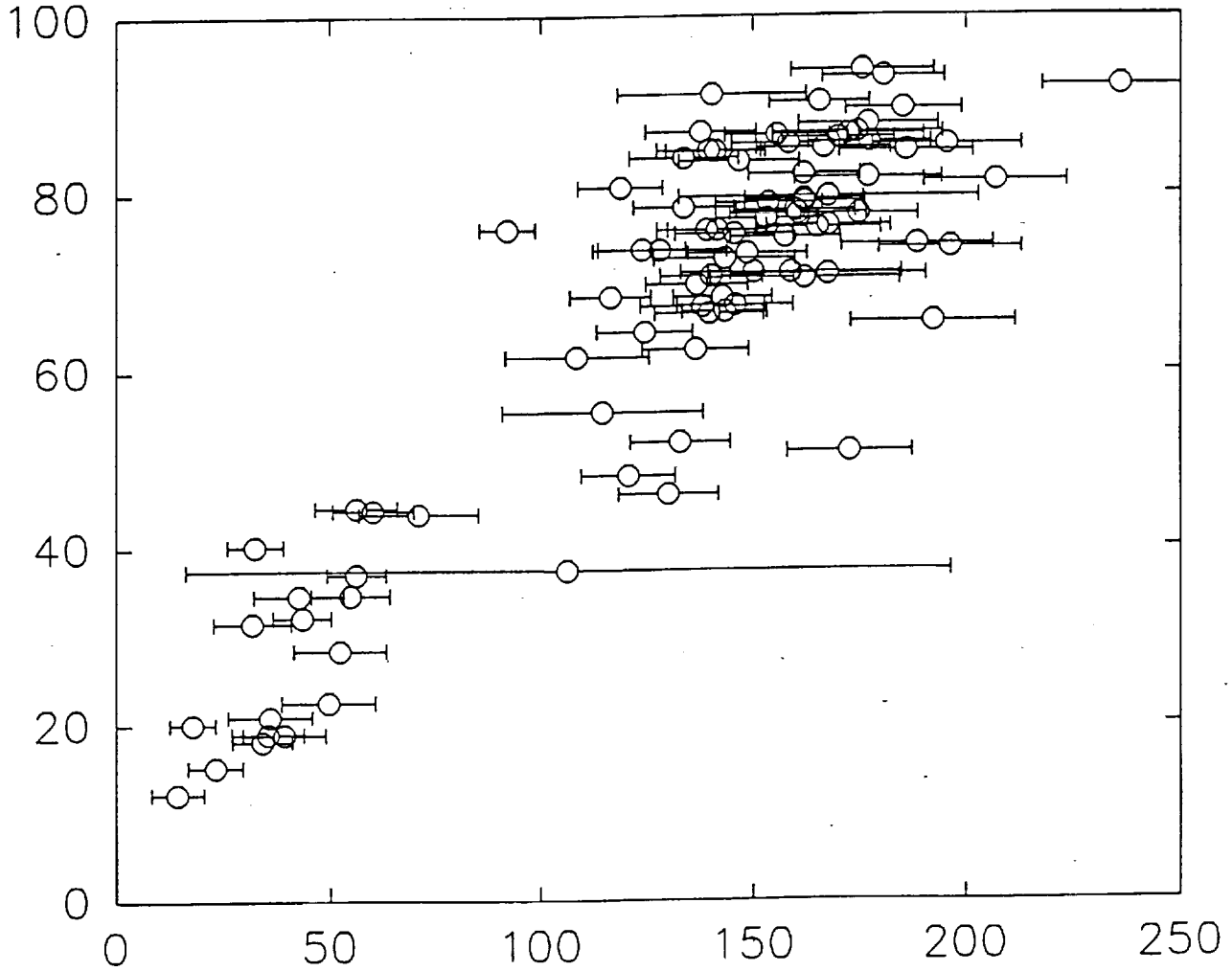


Fig. 9b

Relative Ca continuum in C spectra (FFT)



Relative Ca from 3.084 MeV peak of A spectra

Fig. 10

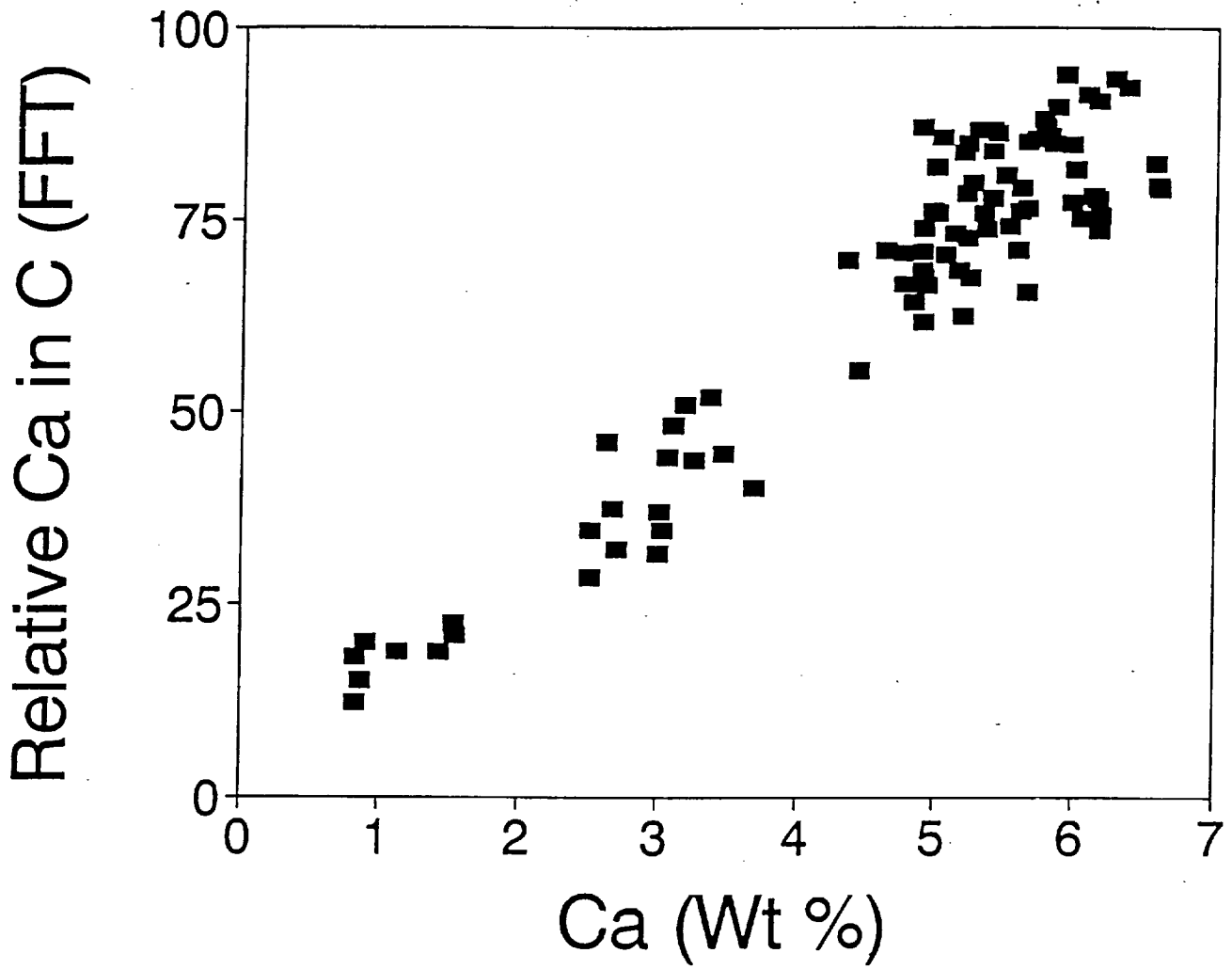


Fig. 11

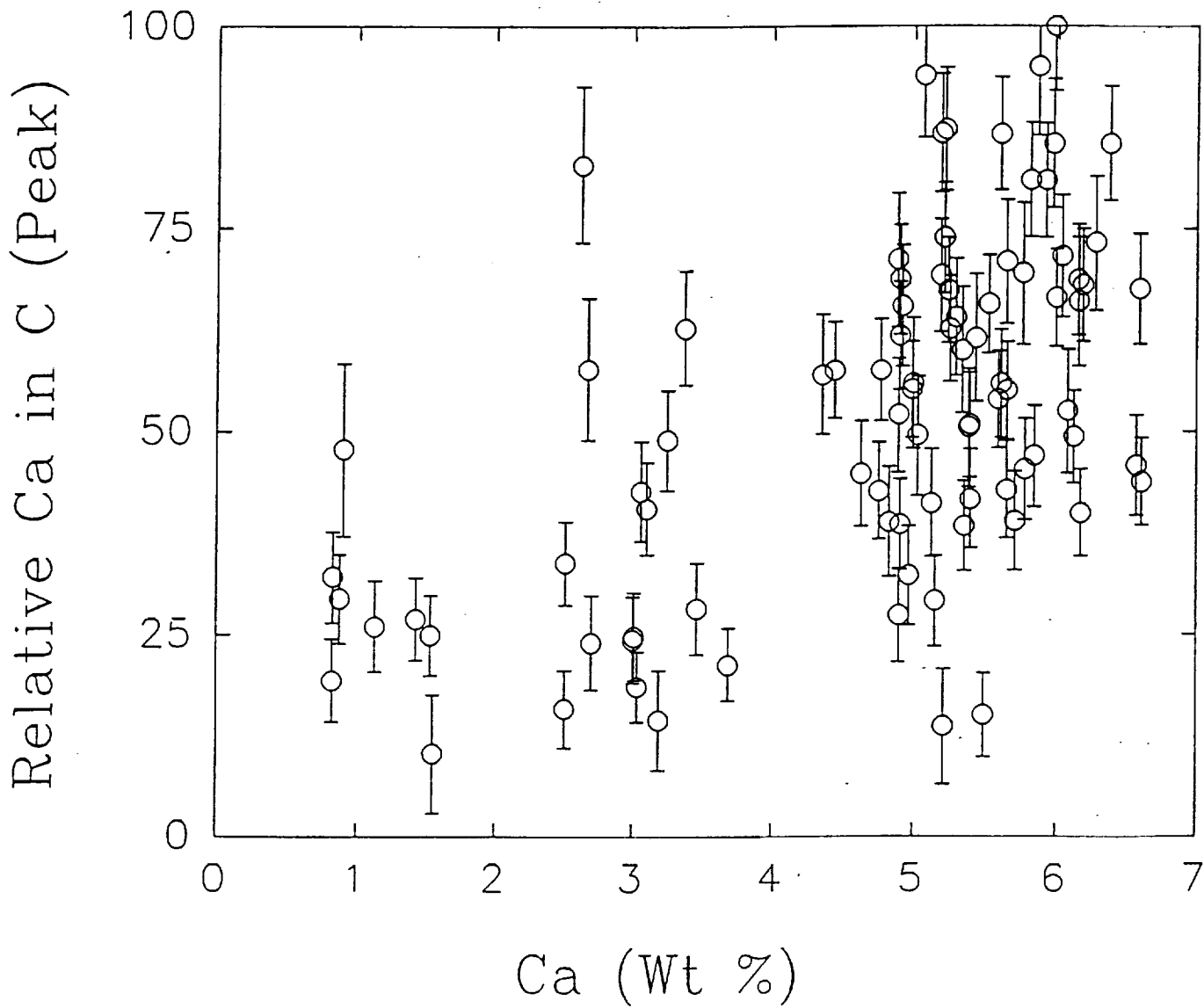


Fig. 12

## Appendix 4

Evaluation of CdTe Detectors for X and  $\gamma$  Ray Detection

**Schlumberger**

**EMR PHOTOELECTRIC**  
P.O. BOX 44, PRINCETON, NEW JERSEY 08542-0044  
TELEPHONE: 609-799-1000  
TELEX: 5106015604 FAX: 609-799-2247

## **Evaluation of CdTe Detectors for X and $\gamma$ Ray Detection**

Karl-Ludwig Giböni

EMR Photoelectric

15 August, 1994

**Abstract:** Cadmium telluride was originally used as X- and  $\gamma$ - ray detector material more than 25 years ago. Although a complete understanding of all the effects limiting the performance of these detectors is still lacking, standard detectors of good quality are commercially available. Especially for applications in space explorations these detectors exhibit clear advantages. The properties of these detectors for X-ray spectroscopy were investigated. Earlier reported polarization effects were not observed. The detectors can be used at temperatures up to 100° C, although with reduced energy resolution. At room temperatures the FWHM for the 122 keV  $^{57}\text{Co}$  line is of order 5 keV. The thickness of the detectors is still limited to about 2 mm. These detectors become fully efficient at bias voltages above 200 V. Due to the slow movement of the holes in CdTe, long pulse shaping times in excess of 2  $\mu\text{sec}$  are required for full efficiency.

## Outline

1. Introduction
  2. Detector Properties
    - 2.1 Leakage Current
    - 2.2 Bias Voltage
  3. Detector Performance
    - 3.1 Rate Capability
    - 3.2 Energy Resolution and Efficiency
    - 3.3 Long Time Stability
    - 3.4 Temperature Dependence
  4. Conclusions
- References
- Table Captions
- Figure Captions

## 1. Introduction

The potential of cadmium telluride as nuclear detectors was recognized more than 25 years ago.<sup>1</sup> The high atomic number and the large density promised to revolutionize the development of X- and  $\gamma$ -ray detectors. The fabrication<sup>2</sup> of good spectroscopic detectors, however, turned out to be more difficult than expected. After a rapid initial progress, the improvements slowed down, limited by the complex problems of growing crystals with the required perfection. Whereas the intense research invested in germanium and silicon paid off with large detectors of high quality and superb performance, most of the interest in compound semiconductor research vanished. The study of CdTe and other room temperature detectors was restricted to a few specialized laboratories. With the continued effort, however, the quality of the detectors reached a stage where applications are realistic, and in many cases these semiconductors offer advantages over scintillators.

CdTe is a compound material exhibiting semiconducting behavior. Together with  $\text{HgI}_2$  and the more recent  $\text{Cd}_{(1-x)}\text{Zn}_x\text{Te}$ , or CZT, it remains the only material sufficiently advanced in its development to be considered for practical detector applications. A survey of the list of all possible materials<sup>3</sup> reveals that no other material promises to be significantly better suited to justify the enormous research effort required for its development into nuclear detectors.  $\text{HgI}_2$  shows several severe drawbacks for many applications, and CZT was strongly affected by hole trapping at least until the recent availability of high purity starting materials. The properties of standard CdTe detectors, on the other hand, appear well adapted for X-ray detection up to about 200 keV.

The quality of CdTe detectors is intimately linked to the perfection of their crystal lattice. Impurities and lattice defects, like interstitials and vacancies, introduce trapping centers for the charge carriers and degrade the detection properties of the crystal. The physical problems are far more complex in compound semiconductors than in germanium or silicon. Research continues to identify the nature and the effect of these carrier traps in order to devise techniques to reduce their influence. Eventually this will result in even better and, most likely, larger detectors.

CdTe detectors are commercially available with good quality. The volume of the available crystals of spectrometer grade is limited to a fraction of a cubic centimeter, but the properties of the material, including high Z, high density, and 'room temperature' operation, make the available standard detectors a valuable alternative.

For most of the tests described in this report, standard detectors<sup>4</sup> were used. The area of the detectors was limited to  $5 \times 5 \text{ mm}^2$ . The thickness was 2 mm, corresponding to the maximum thickness of CdTe spectroscopy detectors currently available.<sup>5, 6</sup>

## 2. Detector Properties

Cadmium Telluride is a compound semiconductor<sup>7</sup> significantly different from the better known germanium detectors. The main properties of CdTe are listed in the following table. The most obvious difference is the large band gap of 1.47 eV, enabling the operation of nuclear detectors at room temperatures. The operating temperature directly influences the leakage current and thus the energy resolution.

Properties of CdTe		
Atomic Number	48,52	
Density	6.06	g/cm <sup>3</sup>
Bandgap	1.47	eV
Average Energy per Pair	4.43	eV
Mobilities	Electrons	1050
	Holes	80
Typical Electrical Field	500	V/cm
$\mu\tau$ Product	Electrons	$2 \cdot 10^{-3}$
	Holes	$4 \cdot 10^{-4}$
Max. Detector Thickness	2	mm
Crystal Structure	Zincblende	
Saturation Carrier Speed	$10^7$	cm/s
Fano Factor (theor.)	.04	

### 2.1 Leakage Current

In an ideal semiconductor detector no charges would be in the conduction band unless they have been liberated by an interaction of an ionizing particle. This means, no current would flow in the device with the bias voltage applied except for the signals from ionizing events. At extremely low temperature the current in a semiconductor is indeed negligible. At elevated temperatures, however, electrons can pick up sufficient energy to cross the band gap. The resulting current, the so called leakage current, grows with increasing temperature and bias voltage. CdTe detectors show an appreciable leakage current of order 10 nA at room temperature and at an electrical field strength of 1 kV/cm. This current increases the noise, and thus reduces the energy resolution of the detector.

The leakage current was measured for a sample of eight CdTe detectors. When the bias voltage

is initially applied, the current sets in with a high value, and then decreases within 20 to 30 minutes to its final value. The effect is caused by charge carrier traps which are slowly depleted under the influence of the electrical field. The final leakage current corresponds to an equilibrium state, where as many traps are filled as others are opened. This equilibrium value depends on both the ambient temperature and on the applied bias voltage. The behavior of the leakage current in the eight detectors during the first 60 minutes is shown in fig. 1. Once the equilibrium value is reached, the response to any variations in the applied voltage follows with the same time constant. The overall change in leakage current with time is less than 50 %. The influence of this time dependent effect on the measurement should be minimal, since normally a few minutes pass between biasing the detector and data taking.

CdTe detectors are cut from large ingots, mostly Cl-doped n-type material. The current flow is inhibited by blocking contacts formed on either side of the crystal. Both contacts are made in the same way, resulting in a basically symmetric detector. A CdTe detector is the direct solid state equivalent of an ionization chamber. In a real detector, however, the currents measured in the two polarities are not exactly equal. This asymmetry is caused by differences in surface preparation. The best polarity of the bias voltage is determined experimentally by the manufacturer choosing the lower of the two leakage currents.

For the eight detectors the reverse current was measured in an attempt to find a correlation with the overall performance. Five of the eight detectors showed current values comparable within a factor 2 in both polarities, demonstrating that the detectors are indeed nearly symmetric. In two of the detectors, however, the reverse current was several hundred nA at low bias voltages. The reverse current in the last detector was about a factor 5 higher. No systematic difference in the performance of these detectors to the others could be established. There was also no correlation between the leakage currents in the two polarities.

## **2.2 Bias Voltage**

The bias voltage, and thus the electric field strength, determines the operating point of the semiconductor. It can be chosen in a wide range. A low voltage is desirable to reduce the leakage current for a good energy resolution. High field strength are, however, required to increase the speed of the charge carriers, and to guarantee complete charge collection in the entire volume of the detector.

For 2 mm thick detectors the maximum bias voltage is normally specified as 100 to 150 V. The highest voltage which still warrants a safe operation for a specific crystal can be determined by measuring the leakage current versus the applied field. Figure 2 shows this dependence for one of the detectors. The current rises linear with the voltage up to a value of 260 V. Afterwards the curve rises steeper and is non-linear. The detectors can be safely operated in the linear region. The increase in bias voltage by more than 50 % above the specification translates directly into a higher rate capability due to the increased speed of the charge carriers.

### 3. Detector Performance

To evaluate the detector performance eight  $5 \times 5 \times 2 \text{ mm}^3$  detectors were used. The crystals are glued in a Lucite ring according to fig. 3. This construction sufficiently protects the detectors while minimizing the amount of material which absorbs X-rays in front of the active volume. Exposure to light enhances the noise in the detectors, and experiments have to be performed in a light tight enclosure.

#### 3.1 Rate Capability

The rate capability is determined with an  $^{241}\text{Am}$  and a  $^{57}\text{Co}$  source at a variable distances from the CdTe crystal. The signals from the detector are recorded in a Multi Channel Analyzer to monitor the spectrum. While moving the source closer to the detector the observed rate increases. Figure 4 shows the spectra for the  $^{241}\text{Am}$  source at different distances, and fig. 5 is the equivalent result for  $^{57}\text{Co}$ . In the  $^{57}\text{Co}$  spectra an additional peak at 60 keV is generated by tungsten X-rays from shielding material within the source container. The eight spectra of each test correspond to different spacings between source and detector, consecutively decreasing.

The observed spectra retain their shape up to very high rates. Then, the probability of two interaction within the shaping time of the amplifier increases, and a tail above the source energy starts to build up. The  $^{241}\text{Am}$  source was sufficiently strong to completely deform the shape of the spectrum at the shortest distance. Up to very high count rates the resolution does not suffer. An indication for the energy resolution is the separation of the 122 keV line and the small 136 keV contribution from  $^{57}\text{Co}$  in fig. 5.

The rate increases up to a maximum of 78 kHz. Bringing the source even closer, and thus increasing the true rate in the detector further, causes the number of correctly identified photons to decrease, as expected for a paralyzable detector. Each pulse paralyzes the detector for the time  $\tau$  in which the charge carriers drift to the electrodes. An additional photon interacting during this interval can not be separated from the original event and contributes to the total energy measurement. The dead time is mainly determined by the speed of the holes, since they are more than a factor 10 slower than electrons.

The detector used in these tests was a  $6 \times 6 \times 2 \text{ mm}^3$  crystal. It was integrated in a system with its amplifier and the power supply. The system was optimized by the manufacturer<sup>8</sup> for the best resolution, and could only be operated up to a bias voltage of 70 V.

The detectors used for the other studies did not have this instrumental limitation. The bias voltage could be safely increased to 250 V. The velocity of the charge carriers in CdTe is linear to the electric field in all the practically accessible range of operation. The velocity follows the relation:

$$(1) \quad v = \mu E$$

E : electric field strength  
 v : velocity of charge carriers  
 μ : mobility    μ<sub>electron</sub> : 1100 cm<sup>2</sup>/Vsec  
                          μ<sub>hole</sub> : 80 cm<sup>2</sup>/Vsec

This relation is displayed in fig. 6 for the electrons and the holes, separately. As a comparison, the corresponding velocities for germanium at 77 K are also shown, with a saturation appearing already at low fields. Increasing the bias voltage for a 2 mm thick detector from 70 V to 210 V increases the speed of the carriers by a factor 3 and directly increases the rate capability.

### 3.2 Energy Resolution and Efficiency

All detectors used for the present studies belong in the class of so called "Grade A Spectrometers", thus they are the best standard quality commercially available. They are preselected by the manufacturer for a good energy resolution, namely 5 - 8 keV FWHM for the 122 keV <sup>57</sup>Co line. A large spread in the resolution of individual detectors can not be expected. The energy resolution obtained in a specific set up, however, may be worsened by many other parameters.

These parameters include the capacitance of the detector as seen by the amplifier, but, foremost, the noise generated by the leakage current. Figure 7a shows the eight <sup>57</sup>Co spectra with different bias voltages at room temperature. As can be seen from the separation of the 122 and 136 keV lines the resolution deteriorates with increasing voltage. The influence of the noise can be reduced by filtering the signals and discriminating against the frequencies governing the noise contribution. This is achieved by shortening the shaping time constant of the amplifier. Reducing the shaping constant from the 1 μsec (fig. 7a) to 0.5 μsec reduces the contribution from noise (fig. 7b). This can be best observed at the highest bias voltages. For 0.25 μsec (fig. 7c) the 122 keV and the 136 keV lines remain well separated even at 250 V. With this shaping constant the resolution does not change with increasing voltage.

The decrease in shaping time also decreases the period in which drifting charges in the detector contribute to the measured signal amplitude. If the shaping time is much less than the transit time of the charge carriers, particularly the holes with their low mobility, events occurring close to the negative contact will be preferably selected. For events with long drift paths the charge collection is still in progress while a pulse height is already recorded. This effect, known as ballistic deficit, is more pronounced in CdTe than in germanium detectors because of the much smaller carrier mobilities. Additionally, the mobilities for electron and holes are substantially different. That means, even for short time constants the electrons will be entirely collected, whereas only holes generated close to the negative contact will be able to fully contribute to the registered pulse height.

The effect of the different mobilities and, consequently, collection times for the two sorts of carriers is demonstrated in fig. 8, 9, and 10. Figure 8 shows temporal development of the integrated charge measured for γ-ray interactions at varying depth in the detector for a bias

voltage of 50 V. The first pulse shape stems from an event which occurred very close to the cathode. The slow holes have no distance to travel. The electrons drift the full 2 mm and determine the rise time. For the further plots of fig. 8 the events take place progressively further away from the cathode. A clear break in the leading edge of the pulse can be observed when all electrons reached the anode and only holes are still drifting with their reduced velocity. In the last plot of fig. 8, finally, the  $\gamma$ -ray interacts near the anode, and the rise time of the observed pulse is equal to the transit time of the holes. Figure 9 and 10 show a similar sequence for 100 V and 200 V bias voltage, respectively. The increase in carrier velocities, both electron and holes, reduces the average rise time of the pulses, but the two component structure of the pulses and the spread in the rise time is still present.

It is interesting to observe nearly straight rises for both the electron and the hole component in fig. 9 and 10. This means that all the carrier travel the full distance to the electrode. At 50 V the pulses induced by holes show a distinct rounding. During the long time of travel holes are trapped with an appreciable probability. Once trapped these holes do no more contribute to the rise in pulse height.

Since the holes are more than ten times slower, their transit time will govern the maximum charge collection time according to:

$$(2) \quad t_m = d / (\mu_h * E)$$

$t_m$  : maximum transit time  
 $d$  : detector thickness  
 $\mu_h$  : 80 cm<sup>2</sup>/Vsec  
 $E$  : Electric field strength

The longest rise time  $t_m$  corresponds to 10  $\mu$ sec for 50 V and to about 2.5  $\mu$ sec for 200 V applied to the 2 mm detector. In the absence of noise, shaping constants much longer than these values would be desirable. They would guarantee complete charge collection and, therefore, the best possible resolution with full efficiency.

In practical measurements much shorter shaping time constants are often preferred. Shorter time constants provide a better noise filtering. If the time constant is below the maximum drift time, however, events with extended hole drift occurring close to the anode are wrongly measured with too low a signal. In the measured spectra these events are shifted away from the peak area and appear as background at lower energies. At low bias voltages these events with long drift time are also affected by hole trapping reducing the measured energy even further. Removing these events and placing them in the background at lower energies seems to improve the resolution of the detector. This practice, however, significantly reduces the efficiency of the detector. For low source energies this drop in detection efficiency is difficult to observe since most photons interact shortly after they entered the dense material of the detector. Deliberately the arrangement of the detector is chosen such that the radiation enters via the cathode. With the reduced average depth of photon interactions, the signals are shorter due to a reduced probability of long drift paths for holes. Choosing a thinner detector would provide the same resolution and efficiency.

In order to determine the relative efficiency of the detector the number of events under a

Gaussians are plotted in fig 11 versus the applied bias voltage. The observed rate with a shaping time of 1  $\mu$ sec continues to rise, and only starts to enter a plateau at about 200 V. The 0.5  $\mu$ sec and the 0.25  $\mu$ sec data do not saturate up to the highest voltage of 250 V. At constant voltage the number of events detected with 0.5 and 0.25  $\mu$ sec is lower than the 1  $\mu$ sec data because of the reduced efficiency.

### 3.3 Long Time Stability

Early CdTe detectors were plagued by polarization effects<sup>7</sup>, i.e. a decrease of the efficiency and a reduction in pulse height after long periods of operation. The time constant for the polarization were normally several hours. The efficiency and the pulse height returned to their initial values after the detector was turned off for a short period. Special treatments of the CdTe crystals were developed to counteract this effect. In more recent publications polarization effects were only reported under extreme conditions<sup>9</sup>, e.g., under intense irradiation with rates of more than 1 MHz. These studies indicated a diminishing effect at high bias voltages and elevated temperature.

Contrary to expectation, some of the detectors showed a slight increase of the efficiency during a ten hour period at low bias voltages. This behavior is opposite to standard polarization effects. The amplitude of the signals, however, seemed unaffected.

In order to investigate the effect further, measurements with a batch of eight detectors were performed at a bias voltage of 80 V. The count rates in an energy window from 150 keV to 250 keV were automatically recorded every 5 minutes. The count rates for four of the detectors remained constant over more than 10 hours. The rate in the other four detectors did change during this period by a few percent. The development of the rates in all eight detectors is shown in fig. 12. Whereas detector 1 to 4 show only statistical fluctuations, the rates for detector 5 to 8 slowly rise. The increase is strongest for detector 8 with about 2.5 %. The leakage current was constant for all eight detectors in this time period, thus the increase in count rate is uncorrelated. Also, no correlation of this effect with any other detector parameter could be established. The voltage was then raised to 240V for fig. 13. The initial rise in count rate is no more discernible

The detectors can be classified into two groups, detector 1 to 4 with no change in count rate, and detector 5 to 8 showing an increase at low bias voltages. Incidentally, the two groups of detectors were manufactured at different times and belong to different batches. According to the manufacturer slight difference in the forming of the contacts can be responsible for this behavior. Since all detectors are extensively tested for long time before shipment, the detectors can be easily screened for this effect.

### 3.4 High Temperature Operation

Contrary to  $\text{Hgl}_2$ , cadmium telluride does not undergo an irreversible phase change below its melting point. The maximum temperature of CdTe detectors is therefore high, limited by the onset of migration of the chlorine dopant. Safe limits for the highest operating temperature<sup>10</sup> with bias voltage applied are specified as 120°C. In practical applications the performance of the detector, especially the energy resolution, will deteriorate and become unacceptable below this temperature. Sample CdTe detectors were repeatedly tested for extended time periods up to 100°C. The high temperature operation did not affect their performance, and no degradation of the detectors was observed.

The most obvious change at elevated temperatures is the increase of the leakage current. The current rises exponentially with the temperature as can be seen in fig. 14. At 100°C the current is about 10  $\mu\text{A}$ , or nearly 1000 times the value at room temperature. Such a high current causes a severe noise which totally overshadows events at low energies.

Due to the large current the voltage drop across the bias resistor is no more negligible. Since the supply voltage could not be raised to compensate for this drop, the bias resistor had to be decreased from 100 M $\Omega$  to 10 M $\Omega$ .

While the detector was heated  $^{57}\text{Co}$  spectra were recorded. Figure 15 shows the spectra for the range from room temperature to 101°C. The bias voltage was 200 V, and the shaping constant was 0.25  $\mu\text{sec}$ . At 24° C the two lines at 122 keV and 136 keV can be clearly separated. Going to higher temperatures the separation of the two lines progressively worsens. At 77°C the 136 keV line is no more discernible. The width of the peak depends on the leakage current, and thus on the applied bias voltage. Figure 16 shows the development of the spectrum at constant temperature of 101°C with bias voltages ranging from 66 V to 242 V. The tungsten peak at about 60 keV from the source shield was not suppressed during these measurements. The spectra are cut off at a slowly increasing threshold. Below this threshold the noise dominates the signals. The cut-off energies range from 40 keV at low voltages to 70 keV at 240 V.

The energy resolution for the 122 keV is shown in fig. 17 in dependence of the operating temperature. The three curves correspond to three different bias voltages. At room temperature the resolution is slightly worse than measured earlier due to the smaller bias resistor. At high temperatures the increased current is the main source for the additional noise. At the highest temperature of 101°C the energy resolution is about 35 keV for a bias voltage of 250 V. Lower voltages reduce the current and in turn improve the resolution.

For these high temperature tests the signals were shaped with a time constant of 0.25  $\mu\text{sec}$ . This reduced the noise caused by the high leakage current. As discussed earlier a 2 mm thick detector is not totally efficient even at bias voltages of 250 V, but longer constants diminish the noise filtering as can be seen in fig. 18 and 19. The spectra in fig. 18 were recorded with 0.5  $\mu\text{sec}$ , and 1.0  $\mu\text{sec}$  was used for fig. 19. The bias voltage was 200 V. These data compare directly with the spectra acquired with 0.25  $\mu\text{sec}$  in fig. 15. All data were recorded at a detector temperature of 92°C. The increase from 0.5  $\mu\text{sec}$  to 1.0  $\mu\text{sec}$  at 200 V worsens the shape. Not only is the peak much wider, but also the noise level is increased.

#### **4. Conclusions**

Cadmium telluride detectors are efficient X- and  $\gamma$ -ray detectors for room temperature operation. Their best energy resolution is 4 - 5 keV FWHM for the 122 keV  $^{57}\text{Co}$  line. This resolution is not as good as germanium detectors, but better than scintillators which are normally used to avoid the cryogenic cooling of the detector. Standard detectors are commercially available up to  $10 \times 10 \text{ mm}^2$  area and a thickness of 2 mm.

Full efficiency of the CdTe material can be reached by biasing the detectors higher than normally advertised. A 2 mm thick detector biased with 200 V delivers signals with 2  $\mu\text{sec}$  rise time, well within the range of standard shaping amplifiers. The choice of bias voltage and shaping constant, however, depends on the specific application. Lower voltages or shorter time constants improve the resolution due to reduced noise or better noise filtering. An reduced efficiency and lower rate capability, however, are the price for this improvements of the spectra.

In earlier literature polarization effects were reported, i.e., the pulse height and thus the detected count rate diminishes with time. Changes in manufacturing of the detectors were successful in suppressing this effect. Polarization is no more observed with newer detector models.

The most attractive feature of CdTe detectors in the laboratory is the room temperature operation. Outside the laboratory, however, the detectors may be used at substantially higher or lower temperatures. In a first study the high temperature behavior was investigated. The detector can be operated at elevated temperatures. With increasing temperature the leakage current increases, and the added noise reduces the energy resolution of the detector. CdTe detectors were operated up to  $101^\circ \text{C}$ . At this value the energy resolution was reduced to 35 keV FWHM for the 122 keV  $^{57}\text{Co}$  line. This might be tolerable for some applications.

Going to lower temperatures it is known that the energy resolution of CdTe detectors is improved. A minimal value for the resolution is expected at  $-10^\circ$  to  $-20^\circ \text{C}$ . A further series of tests is planned to verify this expectations. Especially for space applications the temperature range from Dry Ice to room temperature is very interesting. Recent publications<sup>11</sup> report very good results of CdTe detectors coupled to miniature Peltier coolers.

## References

1. W. Akutagawa, K. Zanio, and J. W. Mayer; CdTe as a Gamma Detector; Nucl. Instr. and Meth. **5 5** (1967) 383
2. F.V. Wald and G. Entine; Crystal Growth of CdTe for  $\gamma$ -Ray Detectors, Nucl. Instr. and Meth. **1 5 0** (1978) 13
3. G. A. Armantrout, S. P. Swierkowski, J. W. Sherohman, and J. H. Yee; What Can Be Expected From High Z Semiconductor Detectors; IEEE Trans. Nucl. Sci. NS-24 No.1 (1977) 211
4. Eurorad, 14 Rue Lenôtre, Mittelhausbergen, 67200 Strasbourg, France
5. P. Siffert; Current Possibilities and Limitations of Cadmium Telluride Detectors; Nucl. Instr. and Meth. **1 5 0** (1978) 1
6. E. Sakai; Present Status of Room Temperature Semiconductor Detectors; Nucl. Instr. and Meth. **1 9 6** (1982) 121
7. R. C. Whited and M.M. Schieber; Cadmium Telluride and Mercuric Iodide Gamma Radiation Detectors; Nucl. Instr. and Meth. **1 6 2** (1979) 113
8. Radiation Monitoring Devices, Inc., 44 Hunt Street, Watertown, MA 02172
9. D. Vartsky, M. Goldberg, Y. Eisen, Y. Shamai, R. Dukhan, P. Siffert, J.M. Koebel, R. Regal, and J. Gerber; Radiation Induced Polarization in CdTe Detectors, Nucl. Instr. and Meth. **A 2 6 3** (1988) 457
10. P. Siffert, CRNS Strasbourg; private communication
11. A.Kh. Khusainov; Cadmium Telluride Detectors with Thermoelectric Cooling, Nucl. Instr. and Meth. **A 3 2 2** (1992) 335

## Figure Captions

1. Development of the leakage current during the first 60 minutes after biasing for the eight detectors.
2. Dependence of the leakage current on the bias voltage for one detector at room temperature. The current first rises linearly up to 260 V and then rises faster.
3. View of the  $5 \times 5 \times 2 \text{ mm}^3$  detector mounted in a Lucite ring.
4. Spectra of  $^{241}\text{Am}$  from a  $6 \times 6 \times 2 \text{ mm}^3$  detector, operated at 70 V. The different spectra correspond to different source detector spacings, and thus different rates. The rate in the full spectrum is indicated.
5. Spectra of  $^{57}\text{Co}$  from a  $6 \times 6 \times 2 \text{ mm}^3$  detector operated at 70 V. The different spectra correspond to different source detector spacings, and thus different rates. The rate in the full spectrum is indicated. The peak at 60 keV is caused by tungsten shielding in the source.
6. Drift velocity of the electrons and holes in CdTe versus applied field strength. For comparison, the velocities for electrons and holes in germanium at 77 K are also shown.
7. Energy resolution for a 2 mm thick CdTe detector versus applied bias voltage for 3 different values of the shaping time constant  $\tau$  of the main amplifier
  - a.  $\tau = 1 \text{ }\mu\text{sec}$
  - b.  $\tau = 0.5 \text{ }\mu\text{sec}$
  - c.  $\tau = 0.25 \text{ }\mu\text{sec}$
8. Observed pulse shapes for  $\gamma$ -ray interactions at different depths in the 2 mm thick detector with a bias voltage of 50 V. The pulse is the integrated charge at the cathode of the detector. The first plot shows an interaction very close to the cathode. The location then is progressively deeper in the detector for the other plots. The pulse height is in arbitrary units.
9. Pulse shapes for  $\gamma$ -ray interactions at different depths in the 2 mm thick detector with a bias voltage of 100 V. These pulses are the equivalent to fig. 8, but at higher bias voltage.
10. Pulse shapes for  $\gamma$ -ray interactions at different depths in the 2 mm thick detector with a bias voltage of 200 V. These pulses are the equivalent to fig. 8, but at higher bias voltage.
11. Number of events falling under a Gaussian fit to the spectra of the 122 keV Co line in dependence of the bias voltage. The accumulation time for the spectra was constant, thus the number of events represents the relative efficiency of the detector. The data points correspond to the 3 different shaping time constants.
12. Development of the count rate in the 8 detectors with a bias voltage of 80 V during the

first 11 hours after turn on. The count rate was measured for  $\gamma$ -rays in the energy range from 150 to 250 keV. Note the expanded scale ranging from 7 to 9 in arbitrary rate units to graphically enhance the effect of the rising count rate in some of the detectors!

13. Development of the count rate in the 8 detectors with a bias voltage of 240 V. during the first 11 hours after turn on. The count rate was measured for  $\gamma$ -rays in the energy range from 150 to 250 keV.
14. Leakage current versus temperature for a  $5 \times 5 \times 2 \text{ mm}^3$  detector at 260 V bias voltage.
15. Spectra of  $^{57}\text{Co}$  for 6 different temperatures between  $24^\circ$  and  $101^\circ \text{ C}$  with a bias voltage of 200 V.
16. Spectra at  $101^\circ \text{ C}$  for bias voltages ranging from 66 V to 242 V.
17. Energy resolution for the 122 keV  $^{57}\text{Co}$  line versus temperature of the CdTe detector.
18.  $^{57}\text{Co}$  spectra for 200 V and 100 V bias voltage for three different shaping time constants, 0.25  $\mu\text{sec}$ , 0.5  $\mu\text{sec}$ , and 1  $\mu\text{sec}$ .
19.  $^{57}\text{Co}$  spectra with 200 V bias voltage and 0.5  $\mu\text{sec}$  shaping constant for six different temperatures between  $24^\circ\text{C}$  and  $101^\circ\text{C}$ .

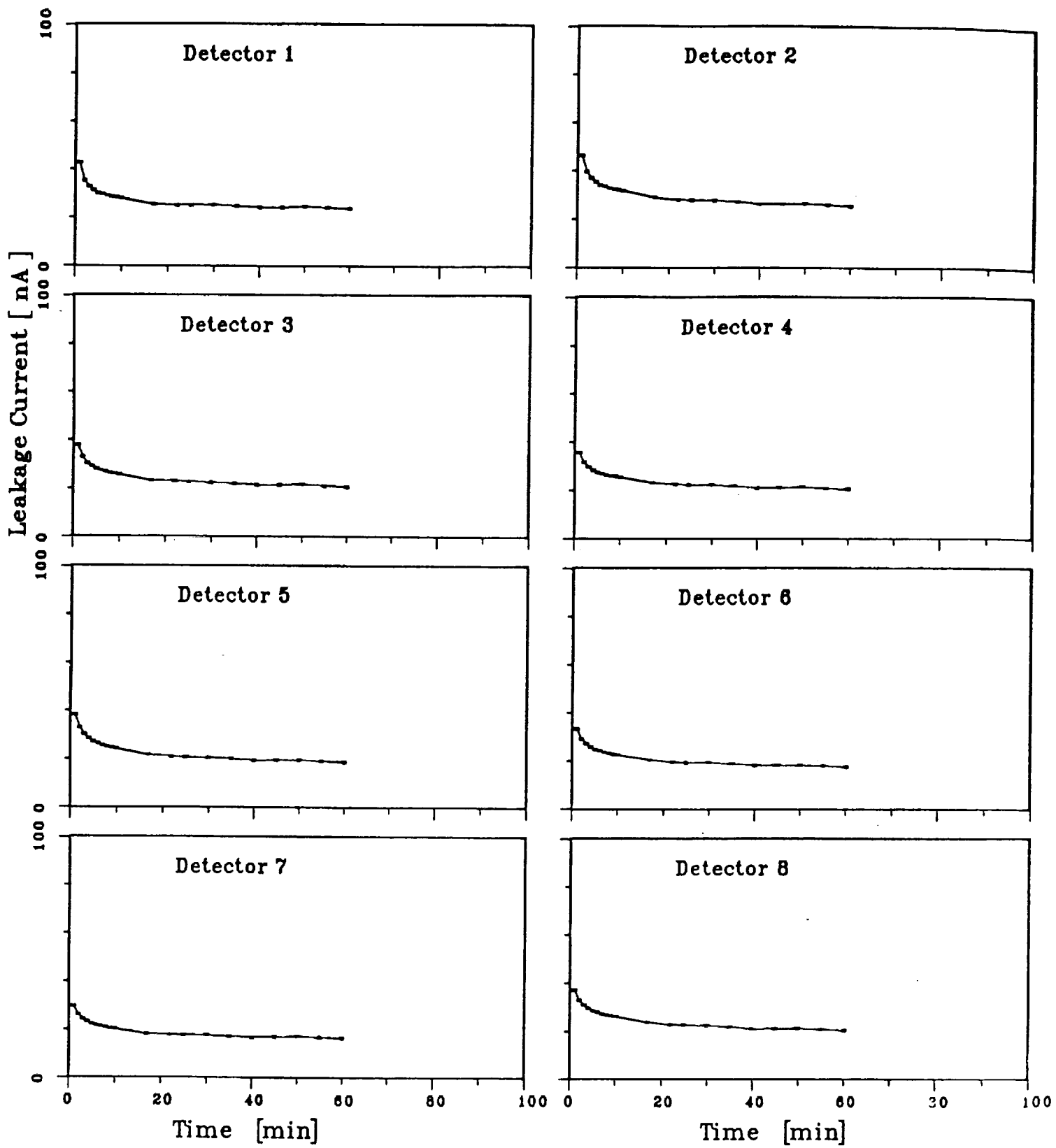


Fig. 1

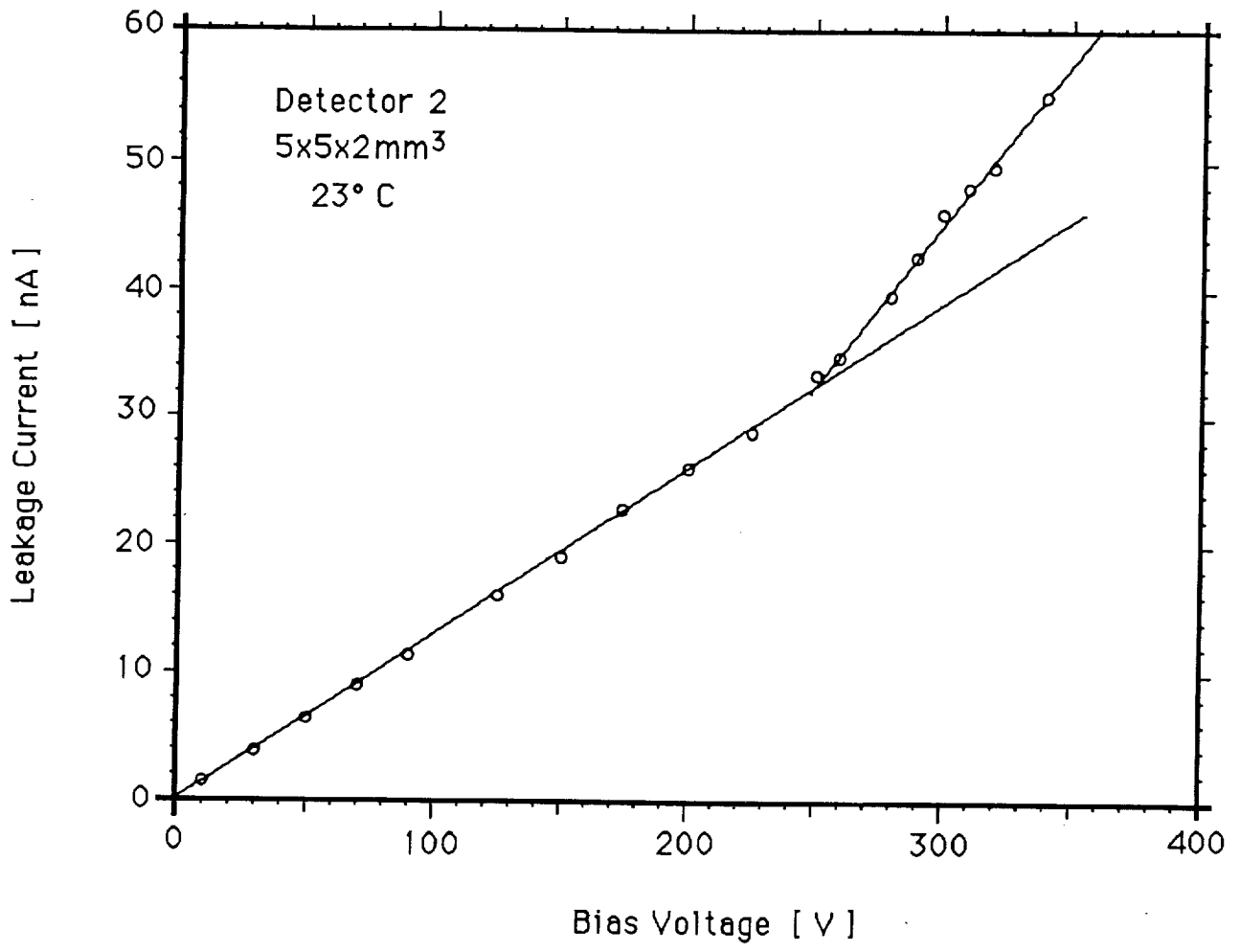


Fig. 2

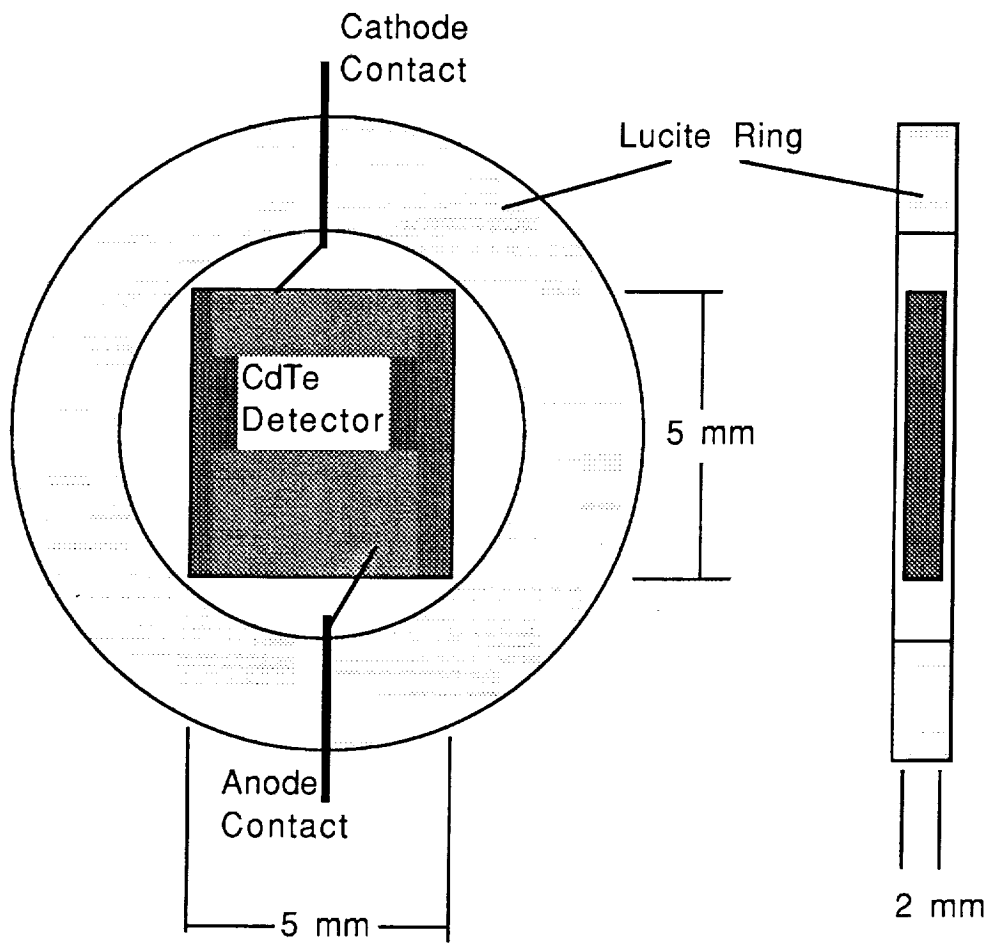


Fig. 3

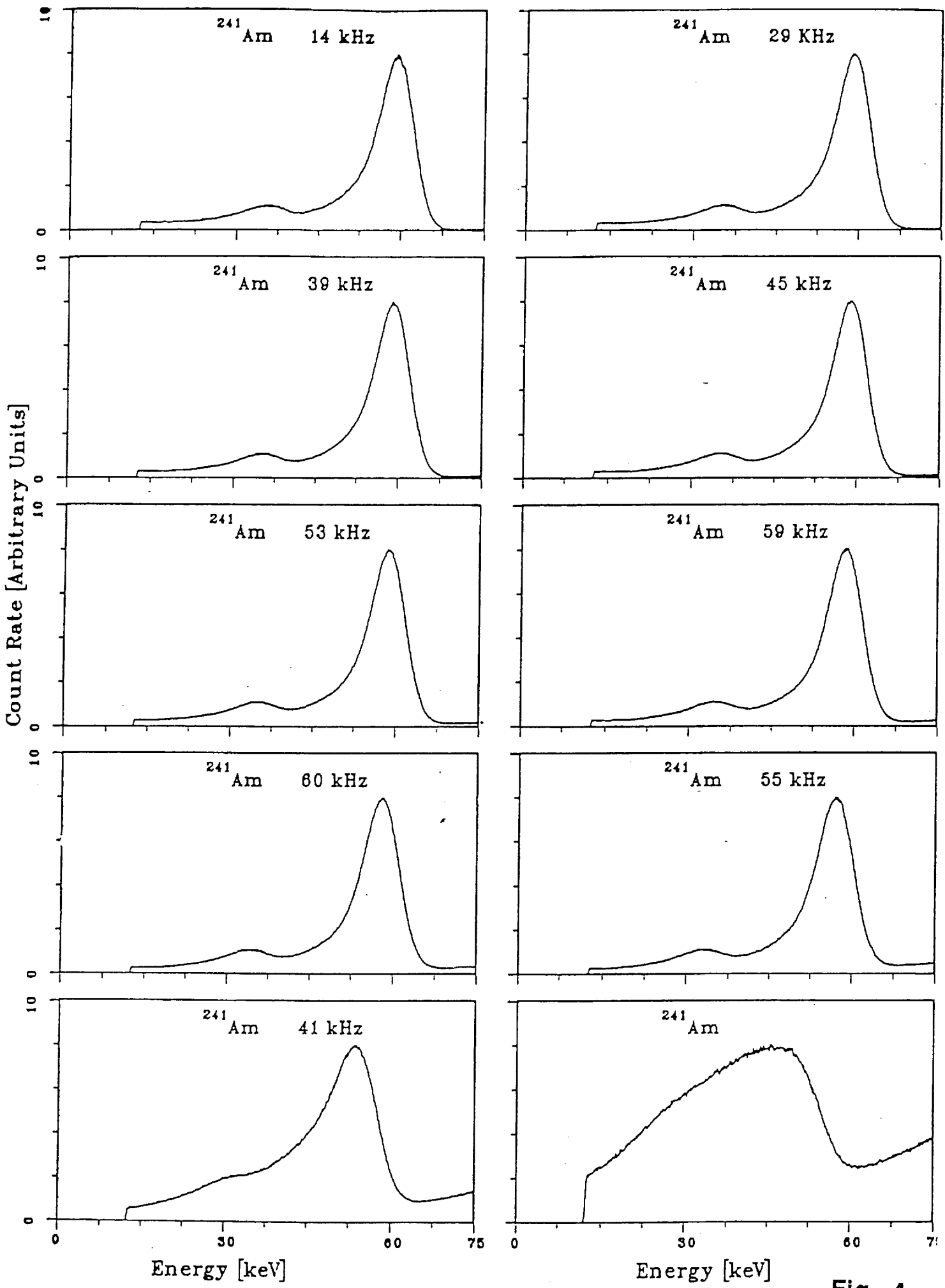


Fig. 4

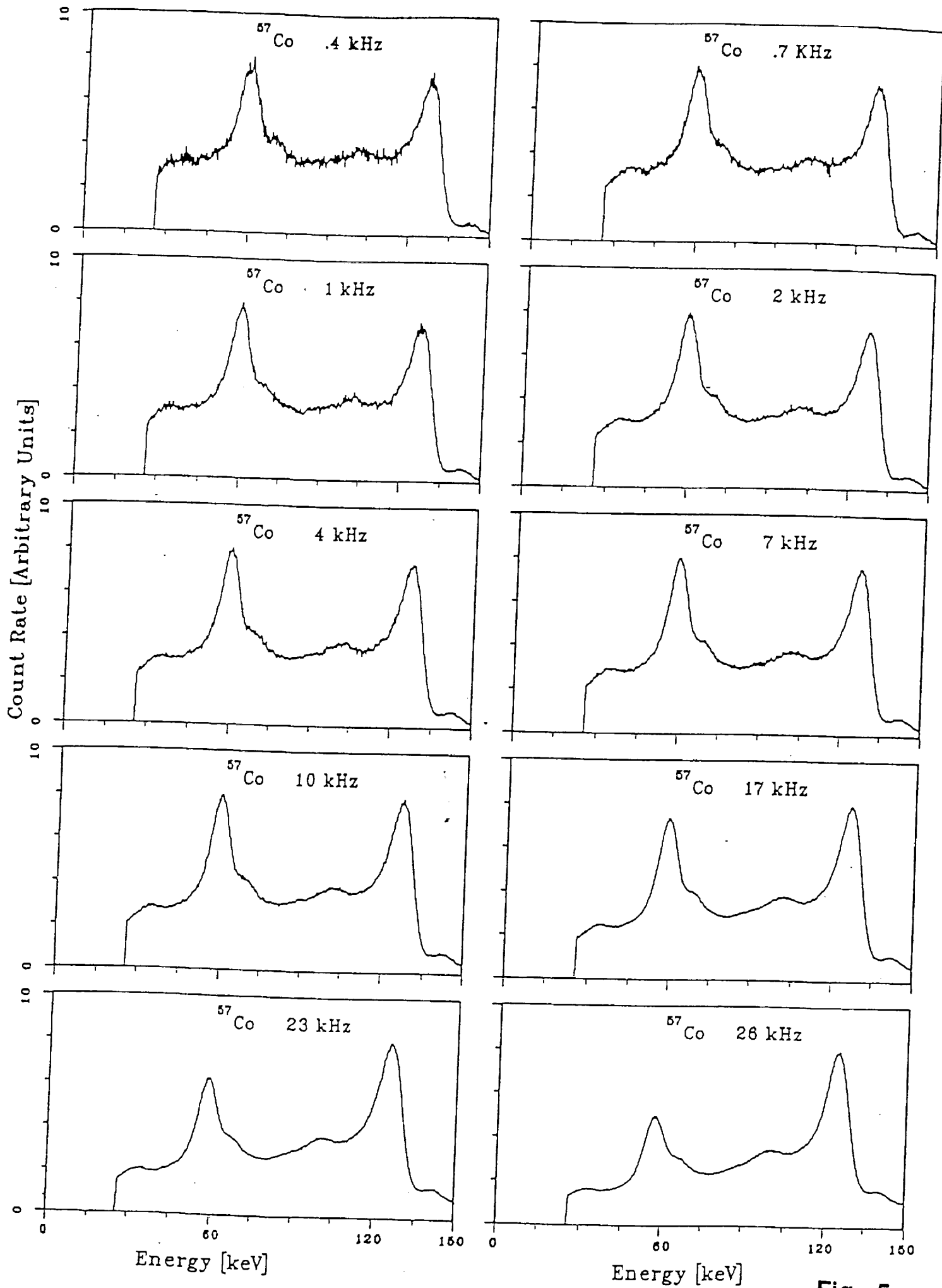


Fig. 5

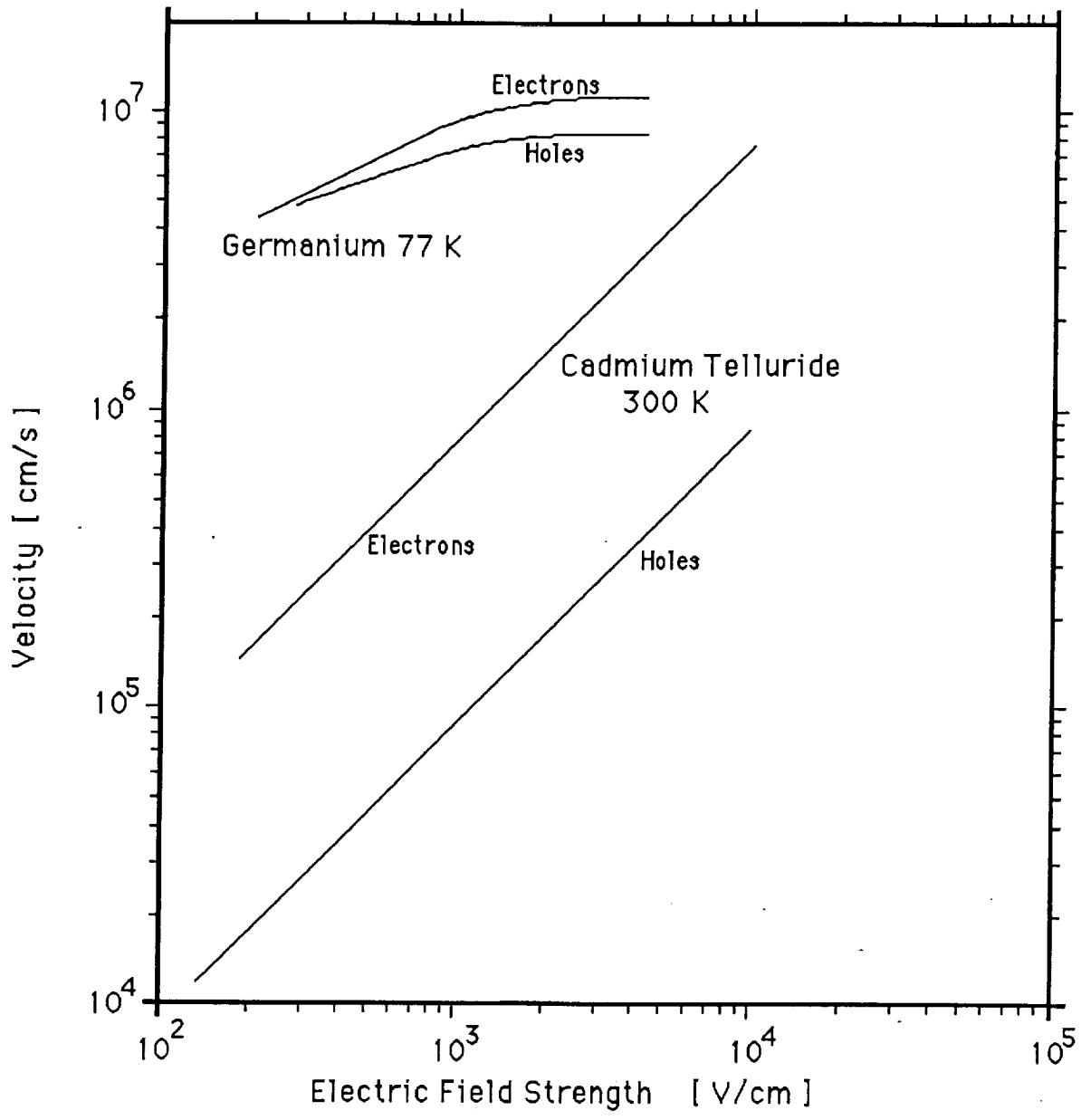


Fig. 6

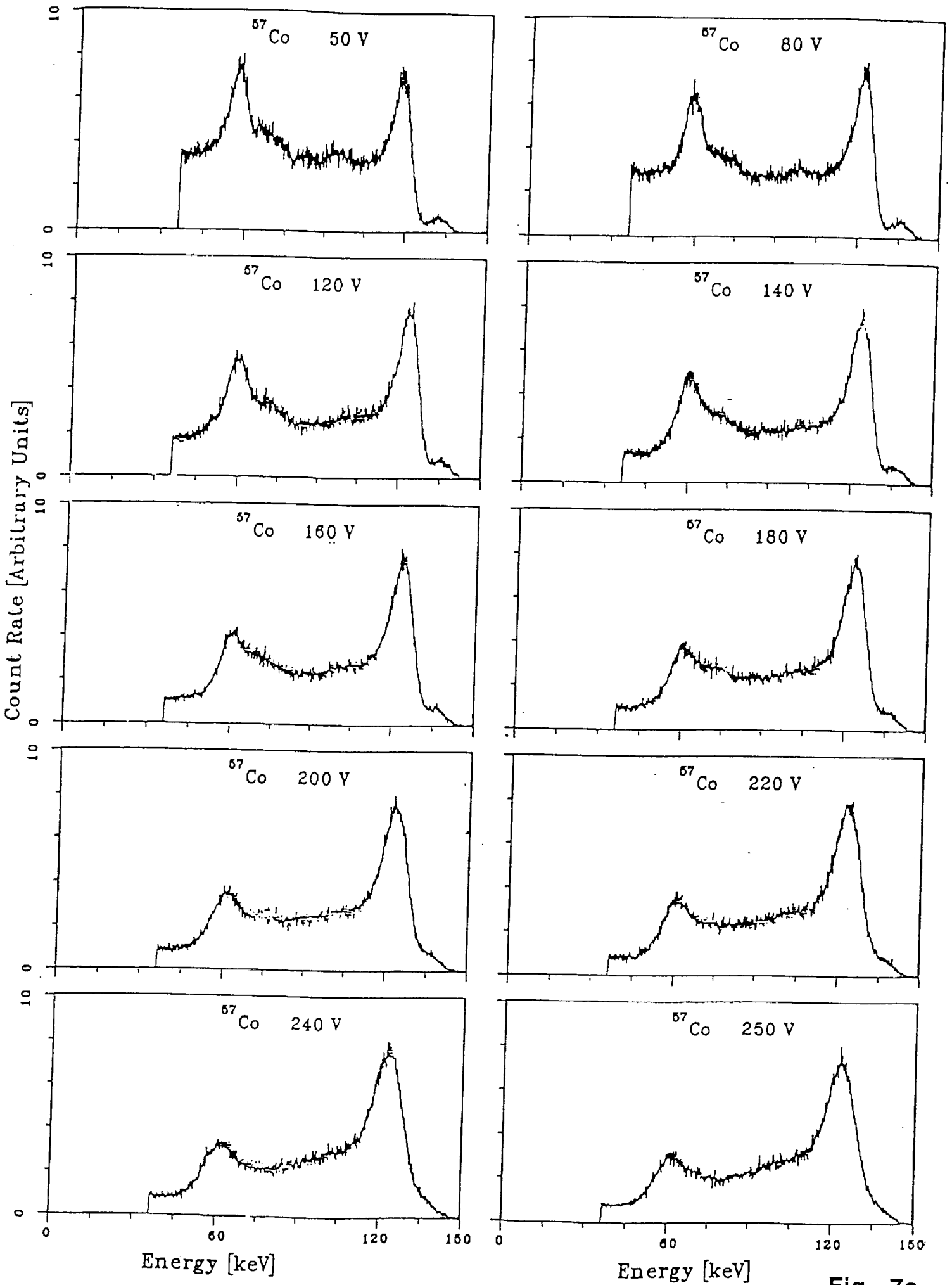


Fig. 7a

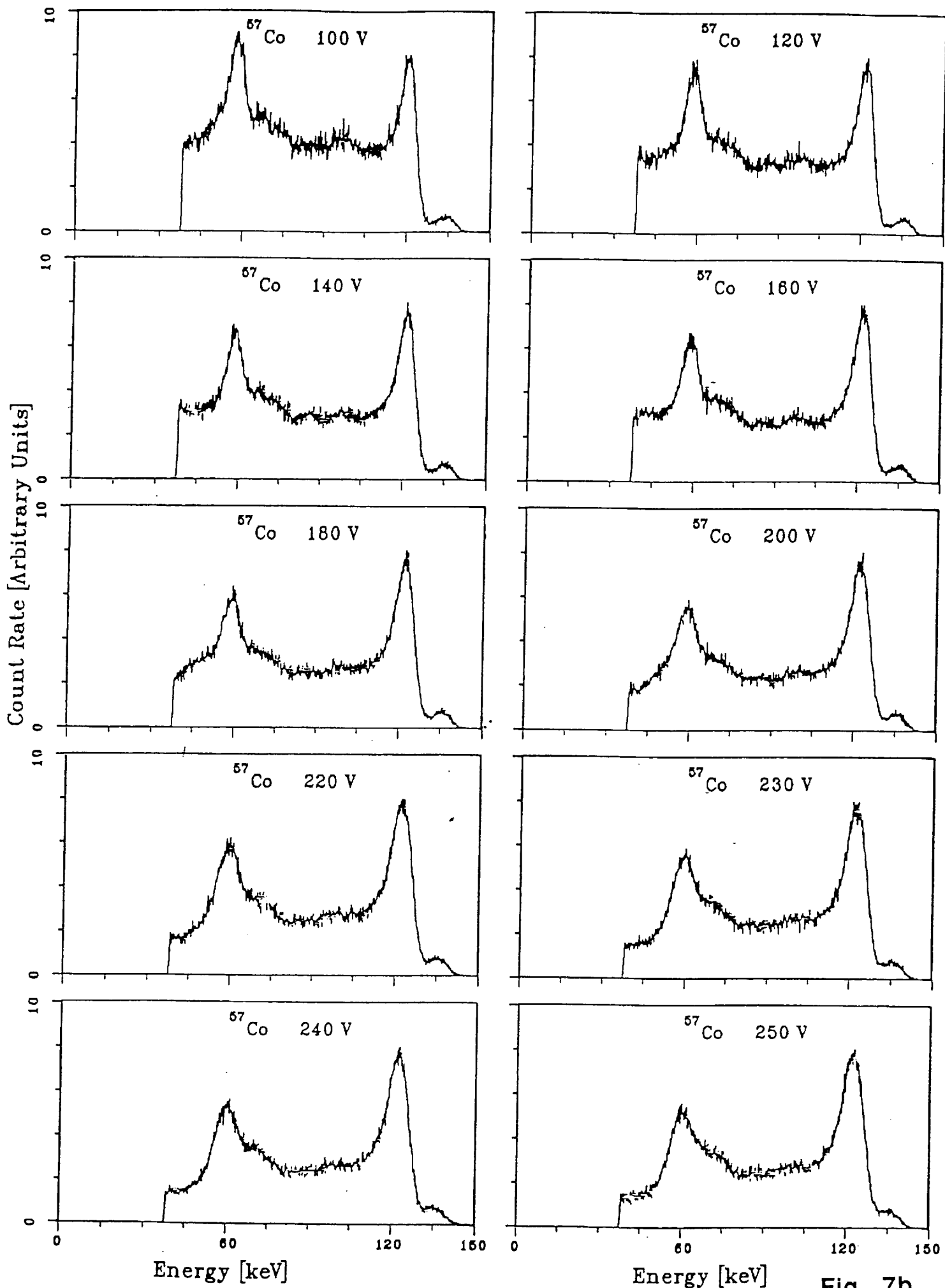


Fig. 7b

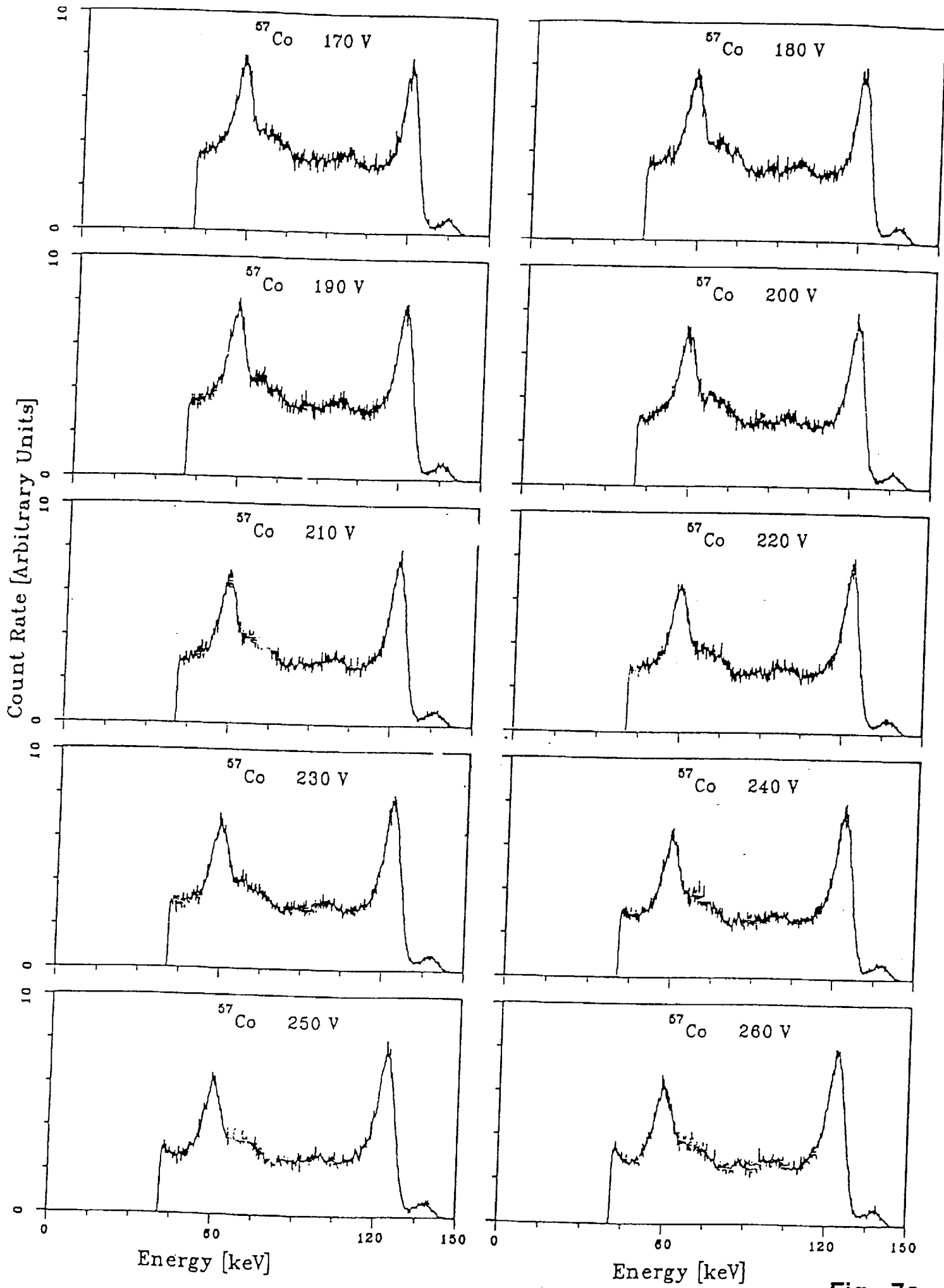


Fig. 7c

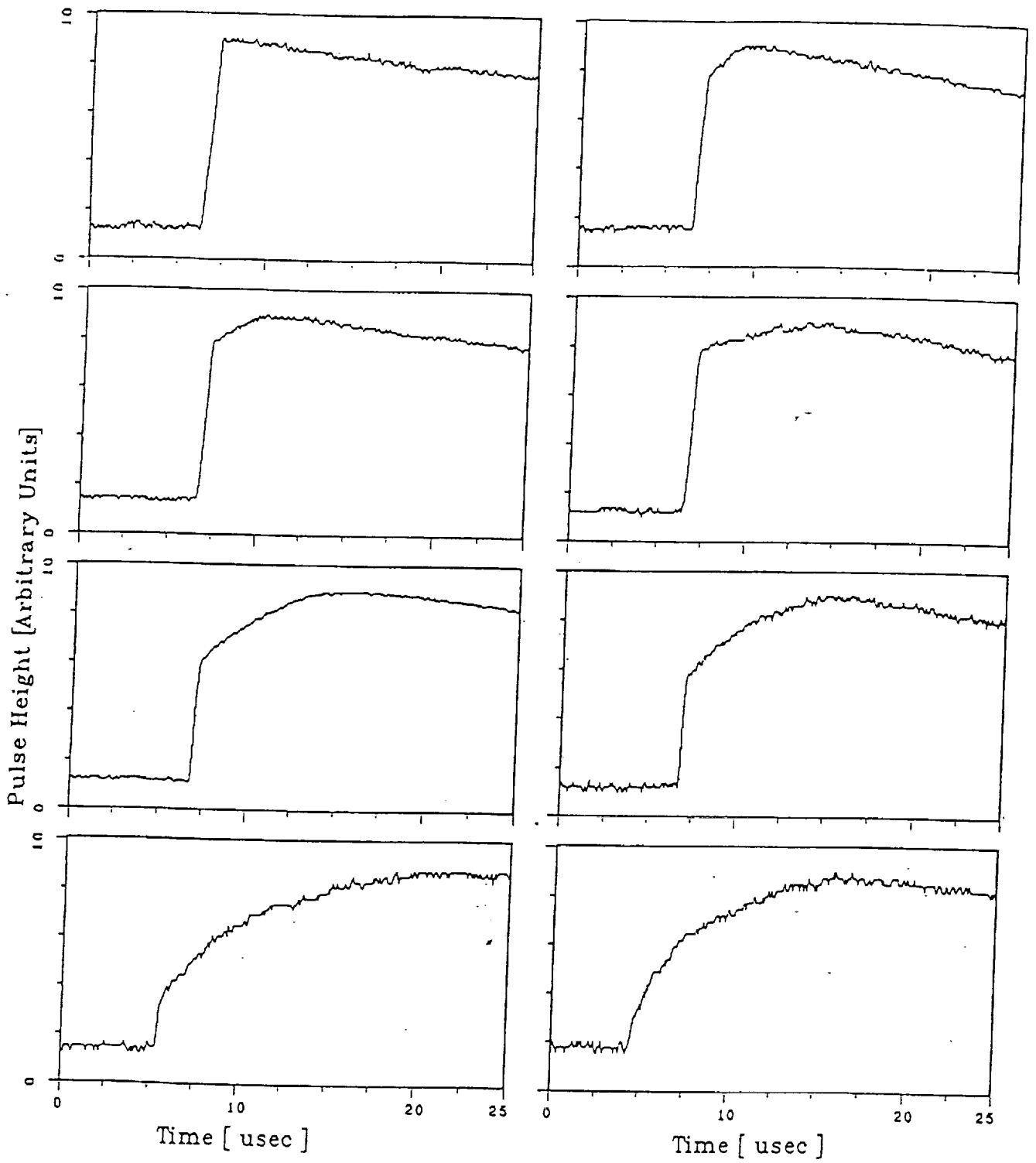


Fig. 8

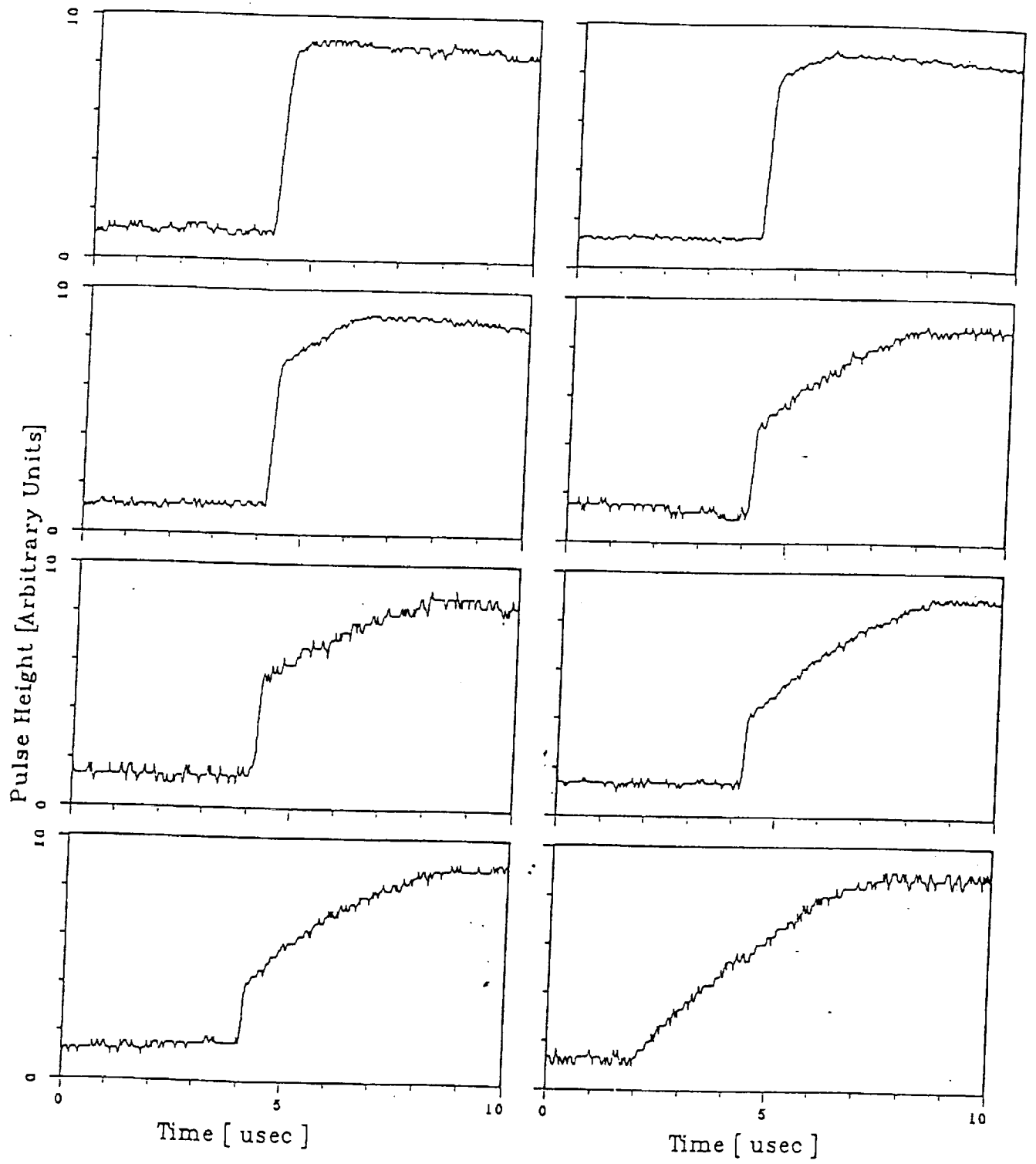


Fig. 9

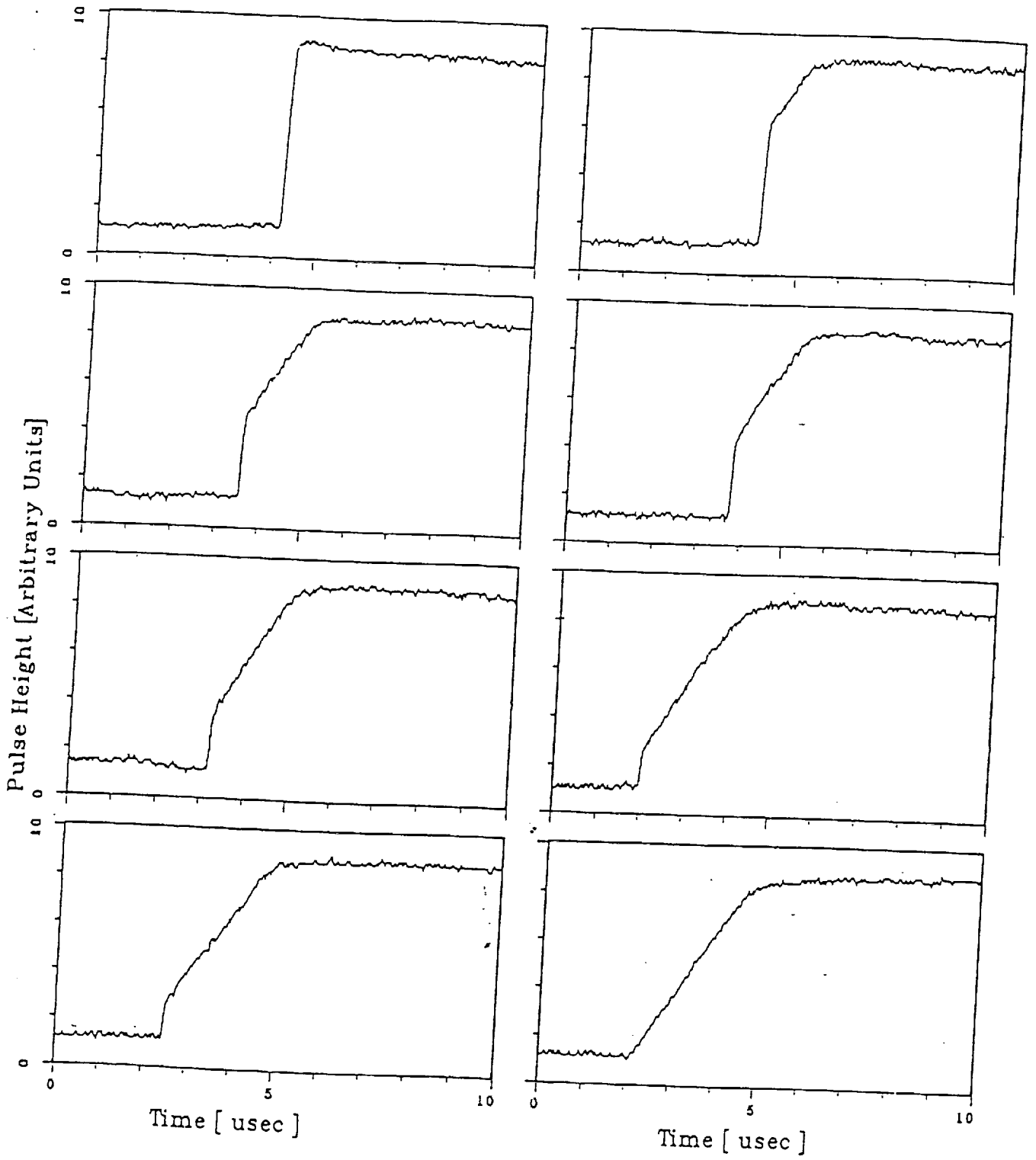


Fig. 10

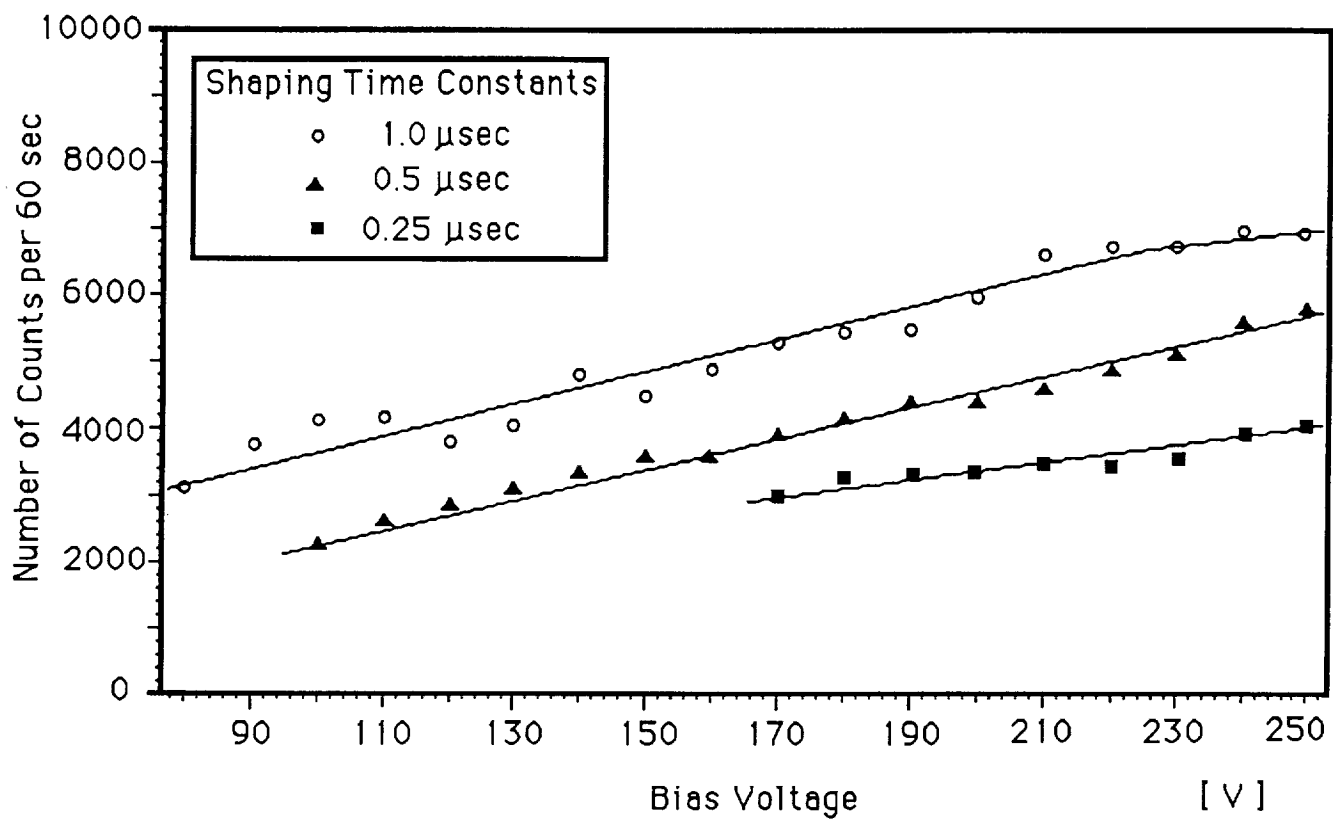


Fig. 11

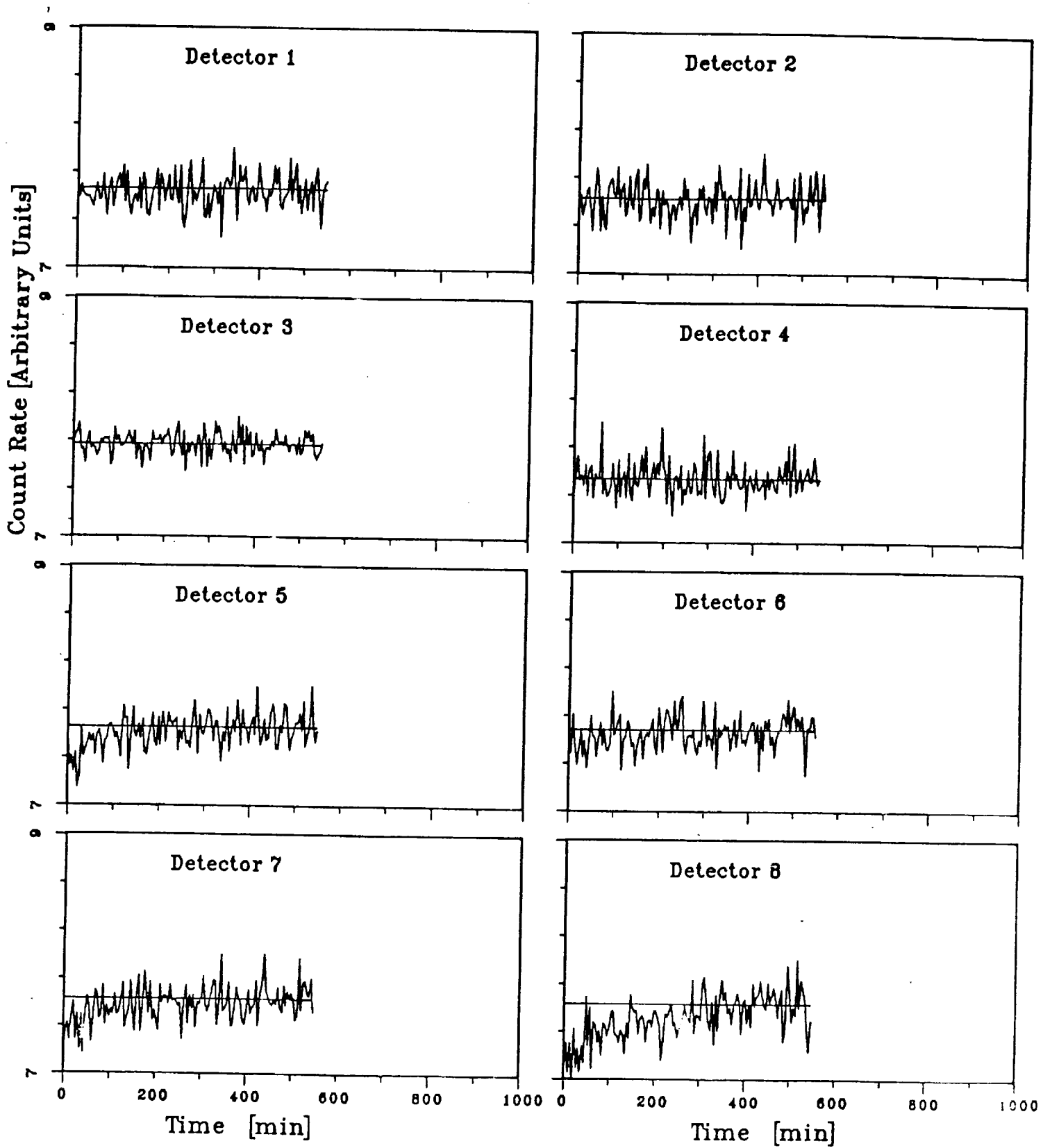


Fig. 12

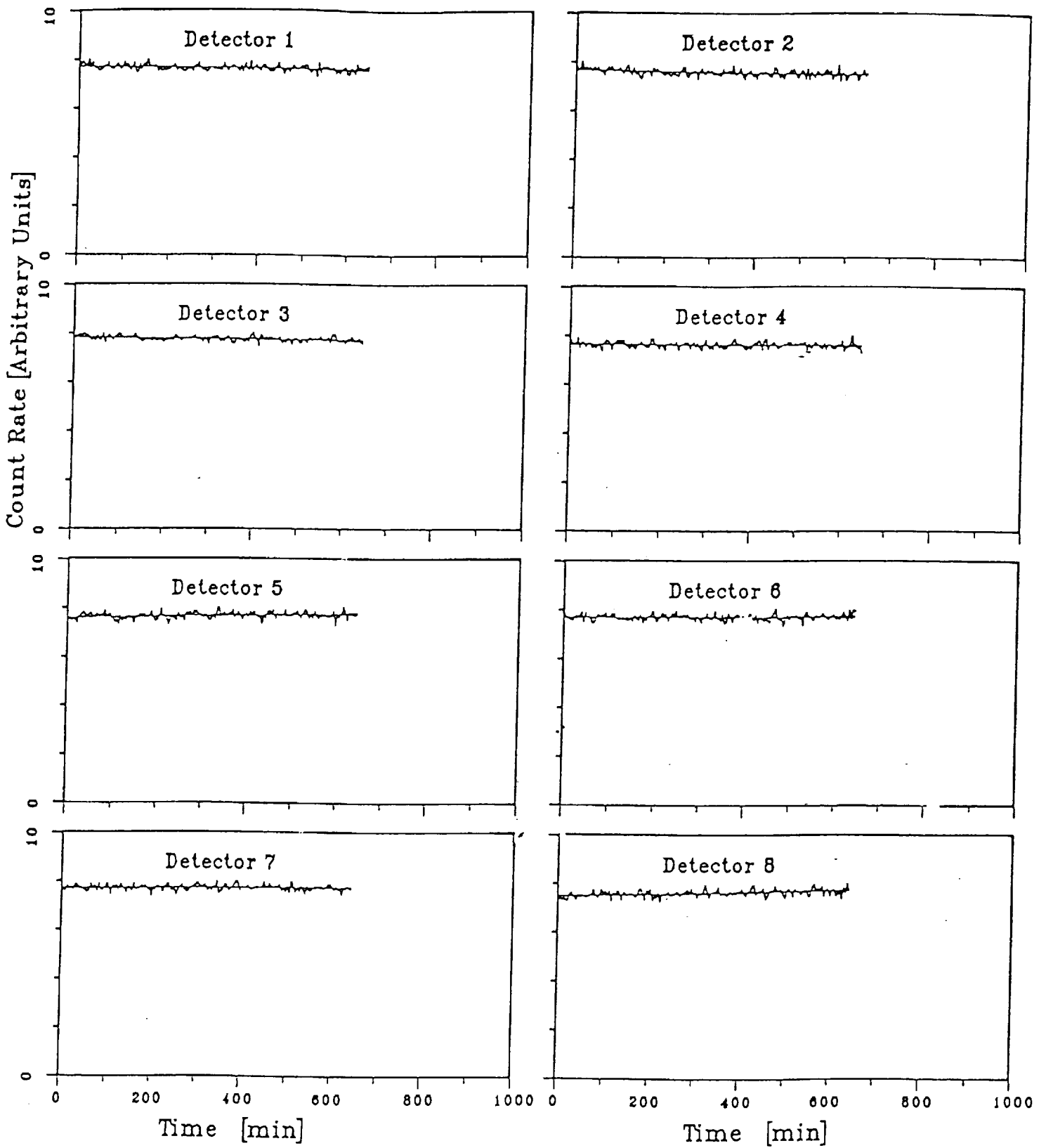


Fig. 13

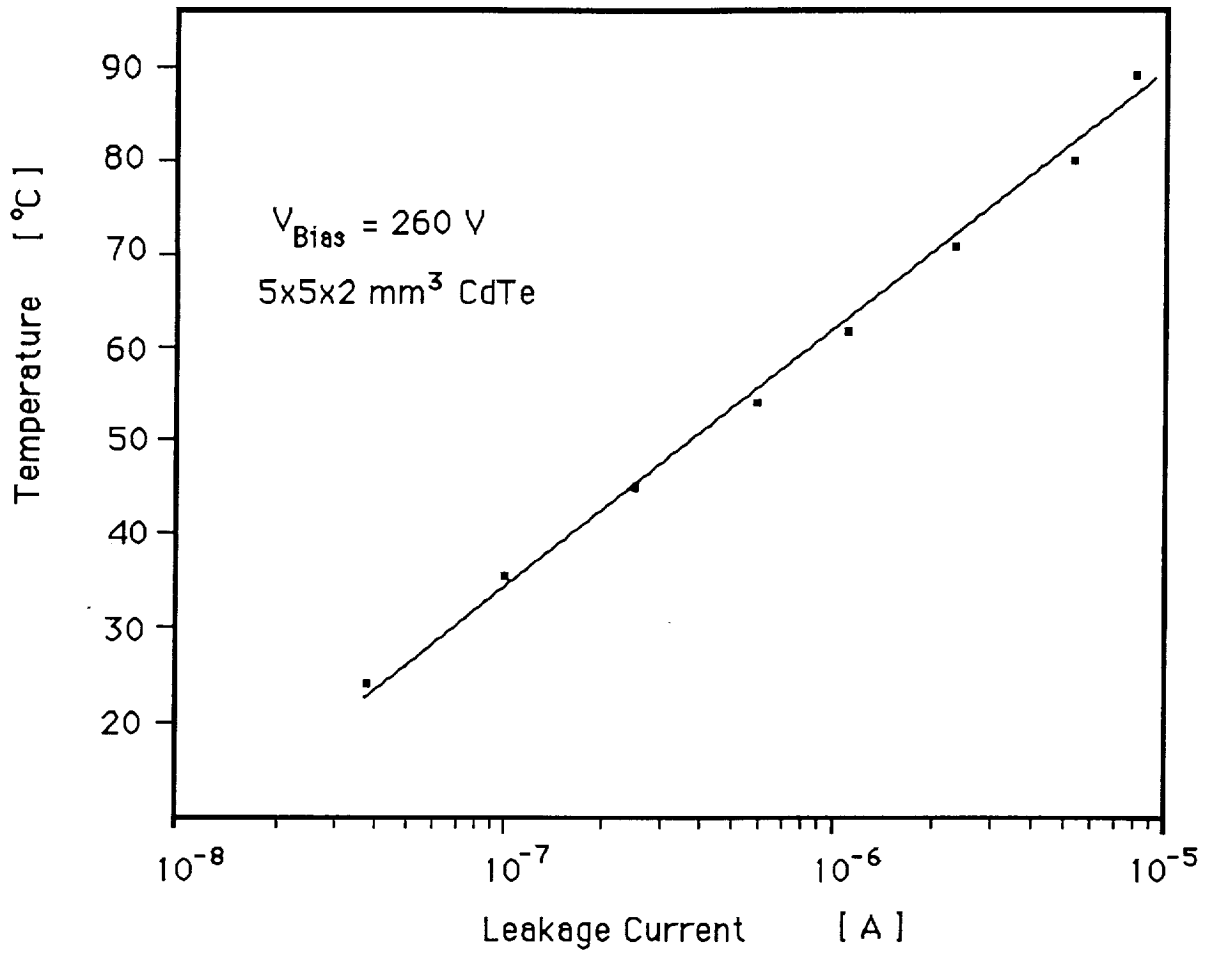


Fig. 14

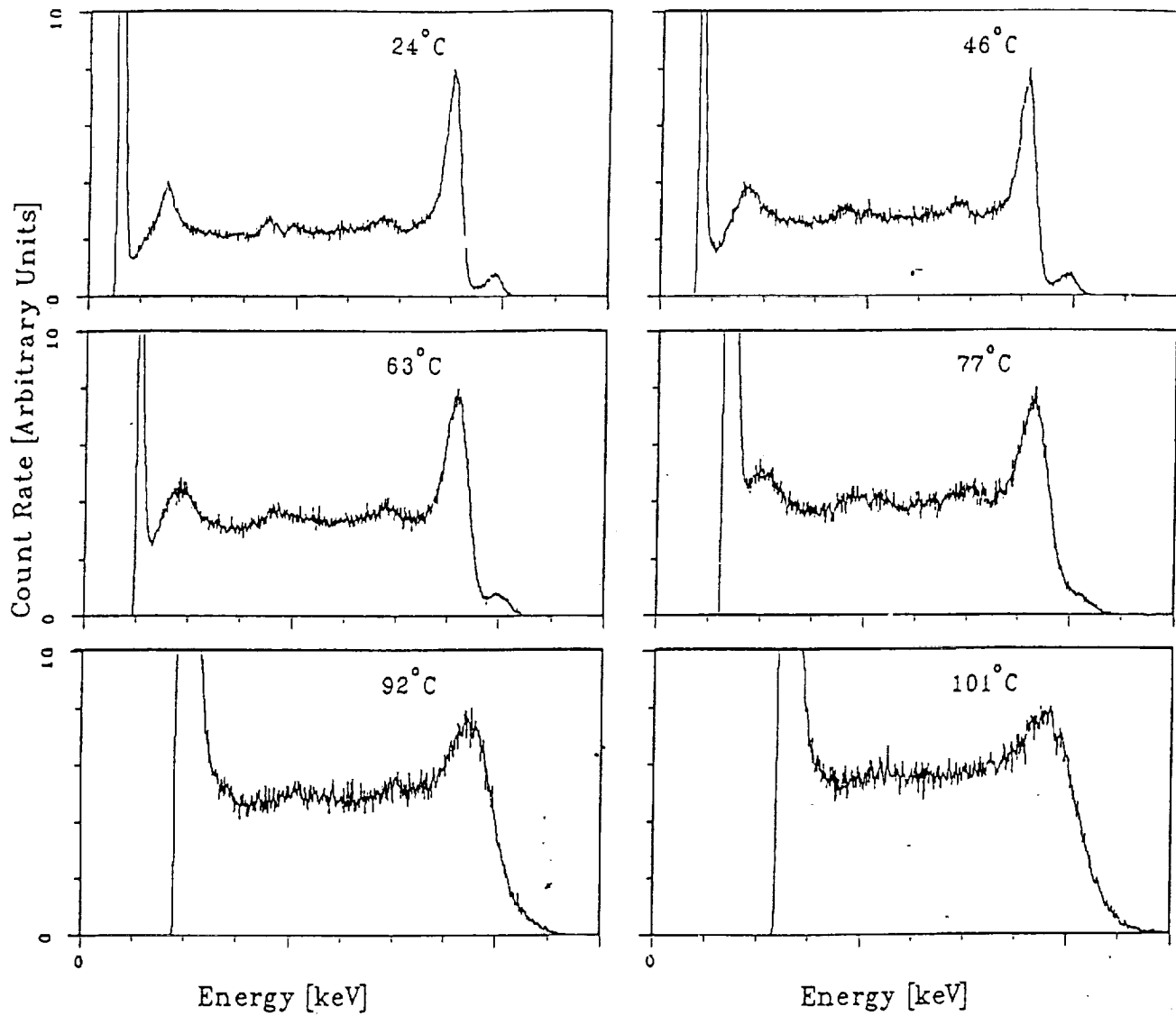


Fig. 15

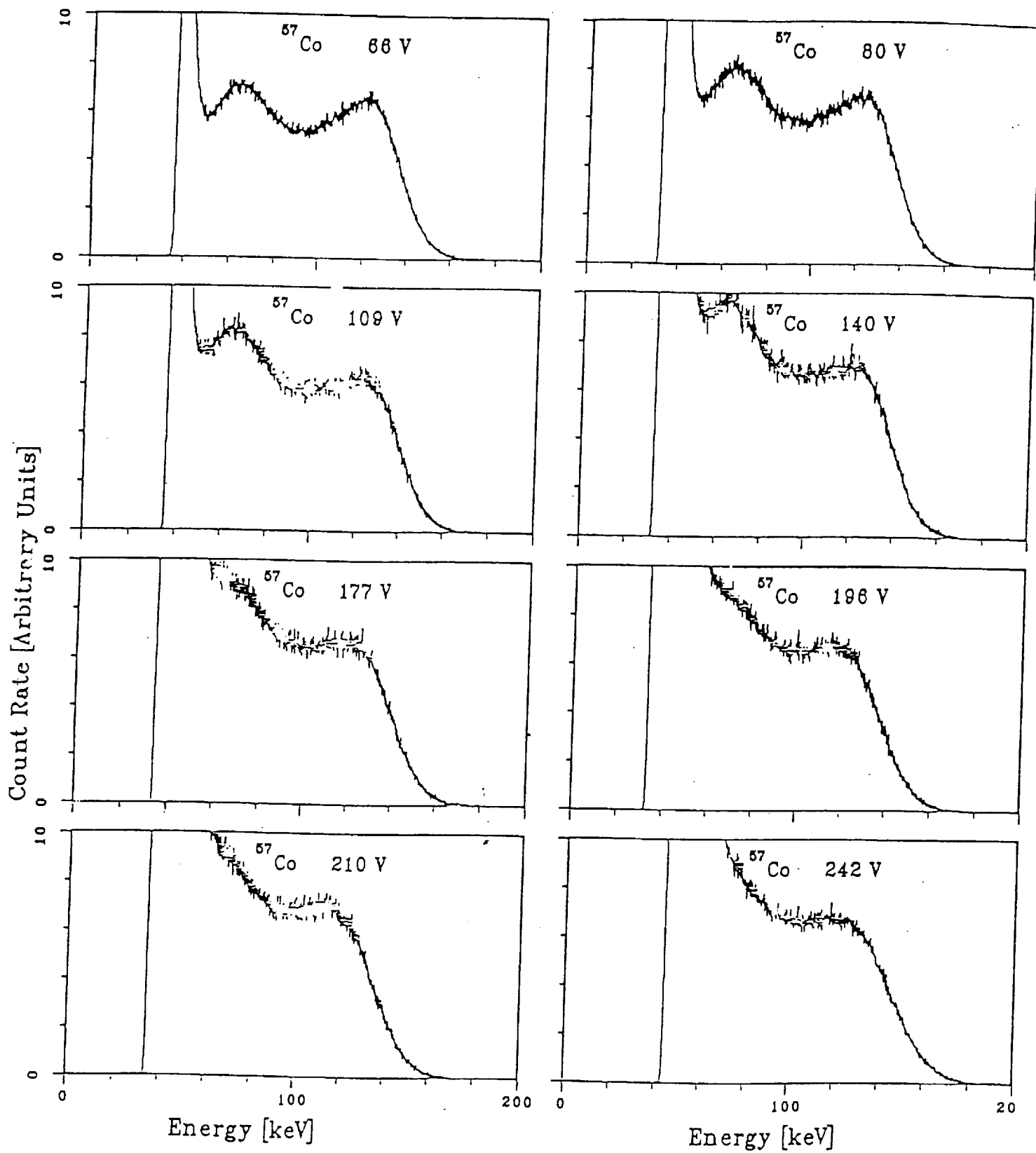


Fig. 16

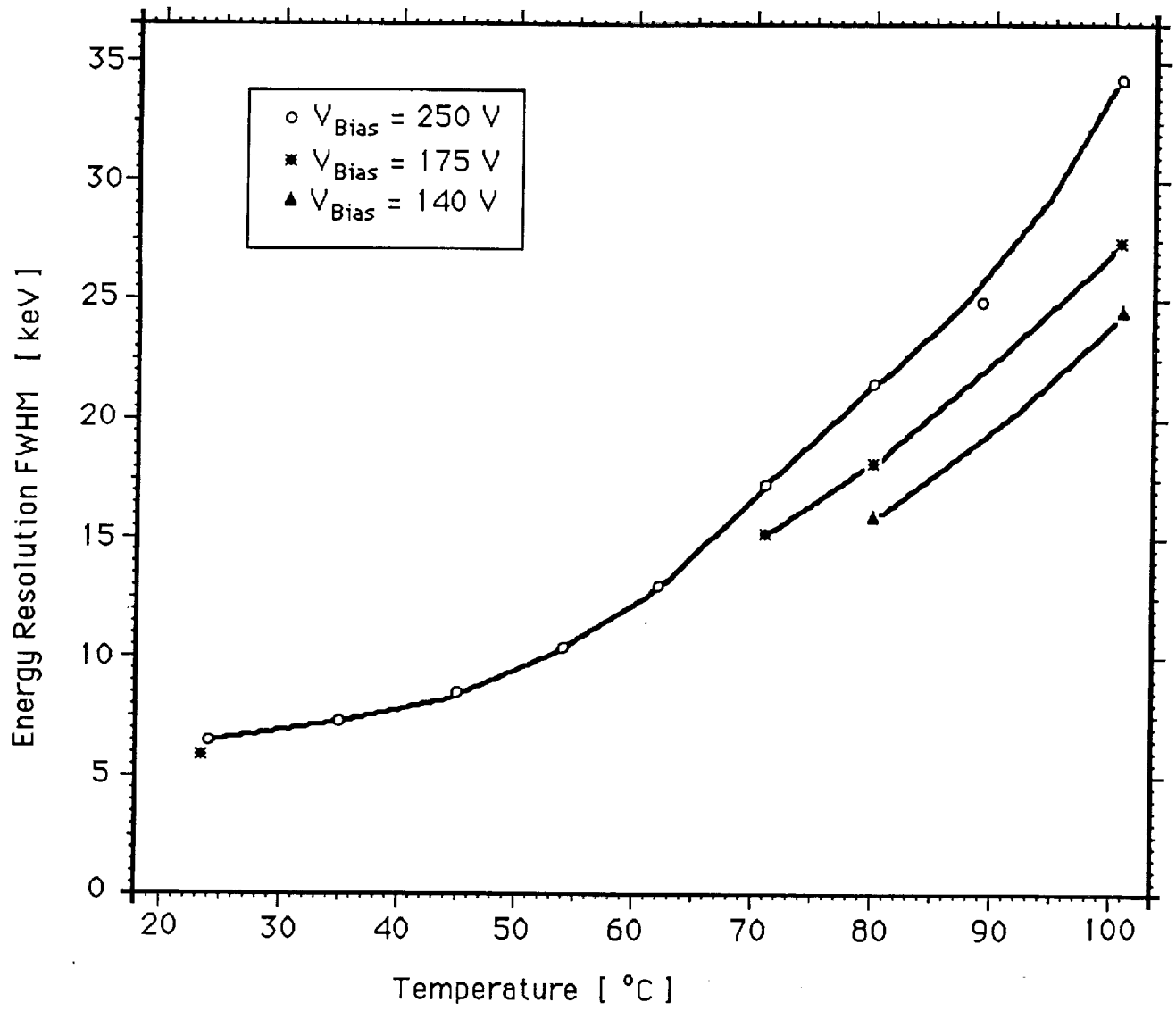


Fig. 17

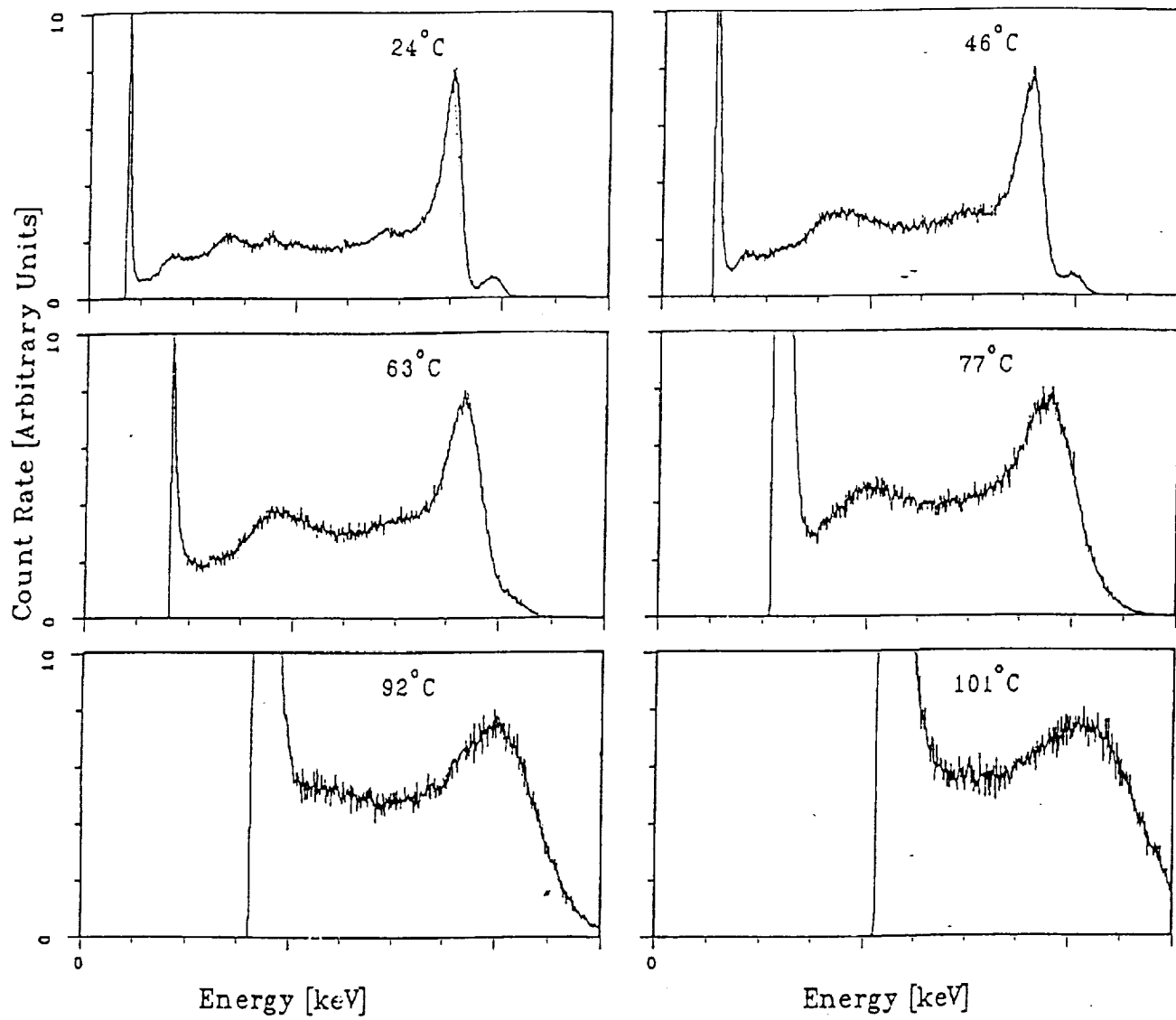


Fig. 18

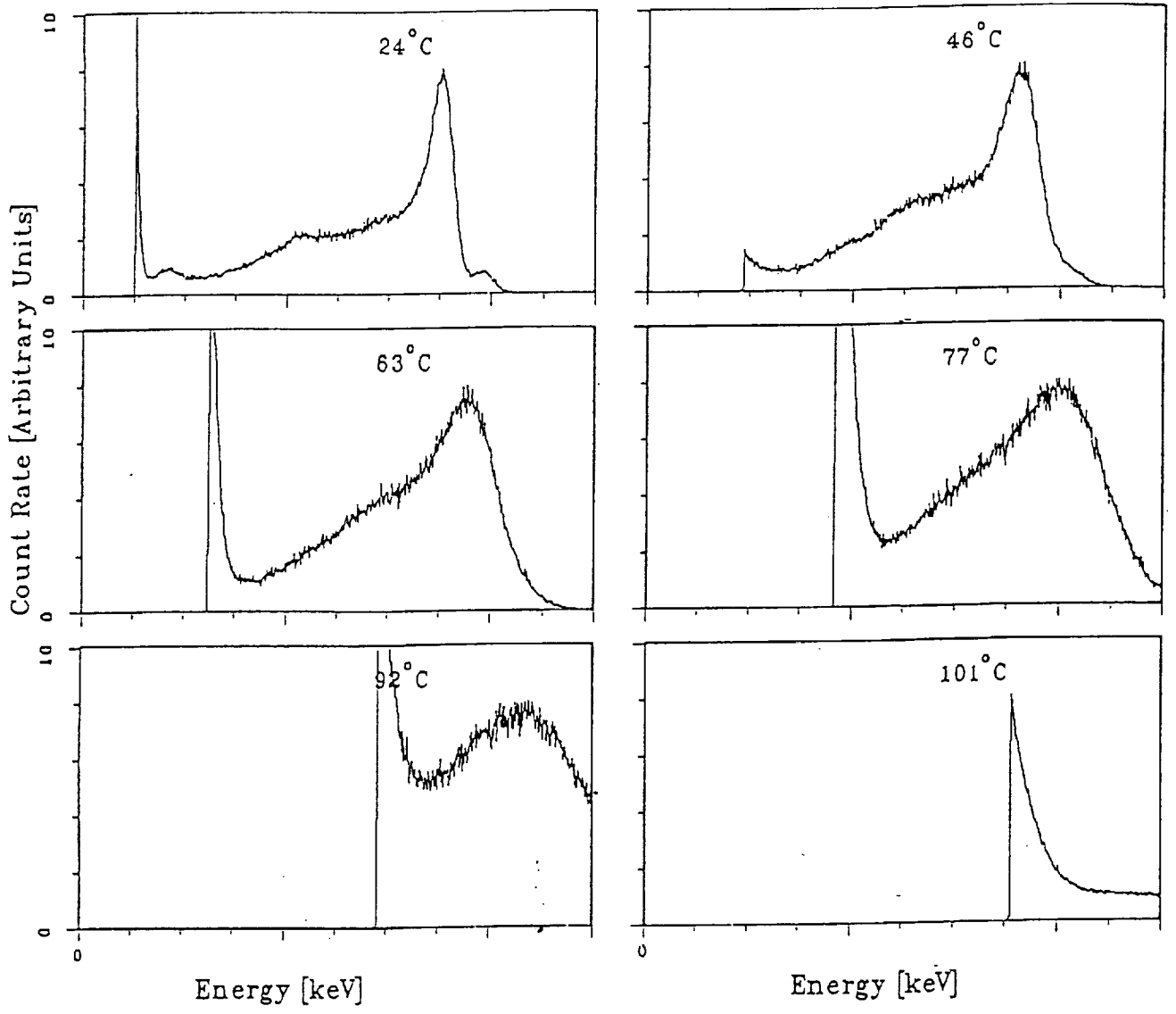


Fig. 19

# REPORT DOCUMENTATION PAGE

*Form Approved*  
OMB No. 0704-0188

Public reporting burden for this collection of information is estimated to average 1 hour per response, including the time for reviewing instructions, searching existing data sources, gathering and maintaining the data needed, and completing and reviewing the collection of information. Send comments regarding this burden estimate or any other aspect of this collection of information, including suggestions for reducing this burden, to Washington Headquarters Services, Directorate for Information Operations and Reports, 1215 Jefferson Davis Highway, Suite 1204, Arlington, VA 22202-4302, and to the Office of Management and Budget, Paperwork Reduction Project (0704-0188), Washington, DC 20503.

<b>1. AGENCY USE ONLY (Leave blank)</b>		<b>2. REPORT DATE</b> August 1994	<b>3. REPORT TYPE AND DATES COVERED</b> Contractor Report	
<b>4. TITLE AND SUBTITLE</b> First Year PIDDP Report on Gamma-ray and X-ray Spectroscopy			<b>5. FUNDING NUMBERS</b>  691 NAS5-32486	
<b>6. AUTHOR(S)</b> M. Mahdavi, K. Giboni, S. Vajda, J. Schweitzer, and J. Truax				
<b>7. PERFORMING ORGANIZATION NAME(S) AND ADDRESS(ES)</b> EMR Photoelectric Division of Schlumberger Technology Corporation P.O. Box 44 Princeton, NJ 08542-0044			<b>8. PERFORMING ORGANIZATION REPORT NUMBER</b>	
<b>9. SPONSORING/MONITORING AGENCY NAME(S) AND ADDRESS(ES)</b> National Aeronautics and Space Administration Washington, D. C. 20546-0001			<b>10. SPONSORING/MONITORING AGENCY REPORT NUMBER</b>  CR-189374	
<b>11. SUPPLEMENTARY NOTES</b>  Technical Monitor: J. Trombka, Code 691				
<b>12a. DISTRIBUTION/AVAILABILITY STATEMENT</b> Unclassified-Unlimited Subject Category 93			<b>12b. DISTRIBUTION CODE</b>	
<b>13. ABSTRACT (Maximum 200 words)</b> <p>Detectors that will be used for planetary missions must have their responses calibrated in a reproducible manner. In addition, it is important to characterize a detector system at uneven portions of its life cycle, for example, after exposure to different amounts of radiation. A calibration and response characterization facility has been constructed at Schlumberger-Doll Research for all types of gamma-ray and x-ray detectors that may be used for planetary measurement. This facility is currently being tested. Initial use is expected for the MARS 94 detectors. The facility will then also be available for calibrating other detectors as well as arrays of detectors such as the NEAR detector with its central NaI(Tl) crystal surrounded with a large BGO crystal.</p> <p>Cadium telluride detector are investigated for applications in space explorations. These detectors show an energy resolution of 5 keV for the 122 keV<sup>57</sup>Co line. Earlier reported polarization effects are not observed. The detectors can be used at temperatures up to 100° C, although with reduced energy resolution. The thickness of standard detectors is limited to 2 mm. These detectors become fully efficient at bias voltages above 200 V. Initial results for a 1 cm thick detector show that the quality of hte material is inferior to the thinner standard detectors and hole trapping affects the pulse height. A detailed characterization of the detector is in progress.</p> <p>Prototypes of photomultipliers based on a Channel Electron Multiplier (CEM) are being built to study their performance. Such photomultipliers promise better timing characteristics and a higher dynamic range while being more compact and of lower in weight.</p>				
<b>14. SUBJECT TERMS</b> Detectors, Scintillators, GSO, LSO, YSO, CdW04, CsI(Tl), photomultiplier, Gamma-ray, Remote Sensing, X-ray, Spectroscopy, MARS94			<b>15. NUMBER OF PAGES</b> 160	
			<b>16. PRICE CODE</b>	
<b>17. SECURITY CLASSIFICATION OF REPORT</b> Unclassified	<b>18. SECURITY CLASSIFICATION OF THIS PAGE</b> Unclassified	<b>19. SECURITY CLASSIFICATION OF ABSTRACT</b> Unclassified	<b>20. LIMITATION OF ABSTRACT</b> Unlimited	